

# Some Characteristics of Open Channel Transition Flow

AKM Enamul Haque

A Thesis

In

The Department

of

Building, Civil, and Environmental Engineering

Presented in Partial Fulfillment of the Requirements  
for the Degree of Master of Applied Science in Civil Engineering at

Concordia University

Montreal, Quebec, Canada

September, 2008

©AKM Enamul Haque, 2008



Library and Archives  
Canada

Published Heritage  
Branch

395 Wellington Street  
Ottawa ON K1A 0N4  
Canada

Bibliothèque et  
Archives Canada

Direction du  
Patrimoine de l'édition

395, rue Wellington  
Ottawa ON K1A 0N4  
Canada

*Your file* *Votre référence*  
ISBN: 978-0-494-63268-0  
*Our file* *Notre référence*  
ISBN: 978-0-494-63268-0

#### NOTICE:

The author has granted a non-exclusive license allowing Library and Archives Canada to reproduce, publish, archive, preserve, conserve, communicate to the public by telecommunication or on the Internet, loan, distribute and sell theses worldwide, for commercial or non-commercial purposes, in microform, paper, electronic and/or any other formats.

The author retains copyright ownership and moral rights in this thesis. Neither the thesis nor substantial extracts from it may be printed or otherwise reproduced without the author's permission.

---

In compliance with the Canadian Privacy Act some supporting forms may have been removed from this thesis.

While these forms may be included in the document page count, their removal does not represent any loss of content from the thesis.

#### AVIS:

L'auteur a accordé une licence non exclusive permettant à la Bibliothèque et Archives Canada de reproduire, publier, archiver, sauvegarder, conserver, transmettre au public par télécommunication ou par l'Internet, prêter, distribuer et vendre des thèses partout dans le monde, à des fins commerciales ou autres, sur support microforme, papier, électronique et/ou autres formats.

L'auteur conserve la propriété du droit d'auteur et des droits moraux qui protègent cette thèse. Ni la thèse ni des extraits substantiels de celle-ci ne doivent être imprimés ou autrement reproduits sans son autorisation.

---

Conformément à la loi canadienne sur la protection de la vie privée, quelques formulaires secondaires ont été enlevés de cette thèse.

Bien que ces formulaires aient inclus dans la pagination, il n'y aura aucun contenu manquant.

  
**Canada**

## ABSTRACT

### Some Characteristics of Open Channel Transition Flow

AKM Enamul Haque

Flow separation is a common phenomenon in decelerated subcritical flows as in open channel expansions. A highly distorted velocity and shear stress distribution due to flow separation can lead to a continuous reduction of energy and trigger an adverse pressure gradient resulting in flow separation. This causes loss of energy and hydraulic efficiency of the systems. An experimental investigation was conducted with the use of a gradual rising hump on the bed of an expansion in a rectangular open channel. Besides the hump, split vanes in the flow field were also used to reduce the expansion angle and in turn reduce the adverse effect of flow separation. These modifications resulted in a relatively more uniform velocity and shear stress distribution in the transition and in the channel downstream of the expansion.

A laboratory model of rectangular open channel transition expanding was constructed with Plexiglas plates. It facilitated the measurement of the flow velocity and turbulence characteristics with the aid of Laser Doppler Anemometer (LDA). The total divergent angle of the transition was 19.78 degrees. Velocities were measured along the x, y and z directions, positioning the LDA from both the bottom and the side of the channel.

Two humps with gradual linear rises of 12.5 mm and 25 mm were used. A second device included the use of a single vane and a three vane splitter plates system formed with thin Plexiglas plates.

Mainly velocity distributions, with and without humps and the splitter vanes were the results sought. The variations of energy and momentum coefficients were analyzed to find the effectiveness of the devices used in the transition to control flow separation.

As a small addition to the study, the use of computational fluid dynamics (CFD) to predict the flow characteristics of open channel was also undertaken. Due to their lower time demand and lower cost, these numerical methods are preferred to experimental methods after they are properly validated. In the present study, the CFD solution is validated by experimental results. A limited number of CFD simulations were completed using the commercial Software ANSYS-CFX. In particular, mean velocity distributions for the rectangular open channel transitions were used for model validation. To this end, the three-dimensional Reynolds-Averaged Navier-Stokes (RANS) equations and the two equations  $k-\varepsilon$  models were used. The validation of the model using test data was reasonable.

## ACKNOWLEDGEMENT

I wish to thank Dr. A. S. Ramamurthy for suggesting this research work. I would also like to express my gratitude to Mr. Mustafa Azmal, PhD student and Dr. Diep VO for their assistance and cooperation while conducting the tests in the laboratory.

I would like to thank the doctoral students Mr. Sangsoo Han and Mr. Rahim Tadayan for their helpful suggestions during the course of this research. I am also grateful to Mr. Lang Vo who helped me to install the laboratory set up for this study. Thanks are also due to friends and all those who helped me to carry out this study.

Last but not the least, I express my deepest gratitude and appreciation to my wife Shahana, son Naveed and daughter Nawreen for their patience, understanding and unfailing support.

## TABLE OF CONTENTS

List of Figures.....	x
List of Tables.....	xii
List of Symbols.....	xiii
<b>CHAPTER 1 INTRODUCTION.....</b>	<b>1</b>
1.1    General remarks.....	1
1.2    Objective of the study.....	2
1.3    Scope of the study.....	3
<b>CHAPTER 2 LITERATURE REVIEW.....</b>	<b>5</b>
2.1    Flow separation mechanism.....	5
2.2    Boundary layer flow.....	7
2.3    Losses in open channel.....	9
2.4    Turbulence characteristics in channel transition.....	12
2.5    Geometry of divergence to control flow separation.....	13
2.6    Design considerations for transitions.....	15
2.7    Method of control of flow separation.....	16
2.8    Some previous method of design.....	19
2.9    Present study related to flow separation in rectangular open channel transitions.....	20

<b>CHAPTER 3 EXPERIMENTAL SETUP.....</b>	<b>26</b>
3.1 Physical Model.....	26
3.1.1 Experimental Channel.....	26
3.2 Instrumentation.....	29
3.2.1 Velocity Measurements.....	29
3.2.2 Depth Measurements.....	32
3.2.3 Pressure Head Measurements.....	32
3.2.4 Other Measurements.....	33
<b>CHAPTER 4 THEORETICAL CONSIDERATIONS.....</b>	<b>33</b>
4.1 Hump and its effects.....	34
4.2 Velocity coefficient.....	36
4.3 Energy efficiency in diverging flows.....	37
4.3.1 General approach.....	37
4.3.2 Diffuser effectiveness.....	37
4.3.3 Turbulence intensity and turbulent kinetic energy.....	38
4.3.4 Boundary shear stress distribution.....	39
4.3.5 The Reynolds number.....	40
4.3.6 Froude number.....	40
<b>CHAPTER 5 3D NUMERICAL SIMULATION.....</b>	<b>42</b>
5.1 CFD modeling.....	42
5.2 Computational fluid dynamics (CFD).....	42

5.3	Organization of CFD codes.....	44
5.4.0	Basic governing equations.....	45
5.4.1	Navier-Stokes equation.....	45
5.4.2	Two-equation model $k-\varepsilon$ and $k-\omega$ .....	46
5.4.3	Boundary conditions.....	47
5.4.4	Inlet boundaries.....	48
5.4.5	Outlet boundaries.....	48
5.4.6	Free surface boundaries.....	48
5.4.7	Interface-tracking scheme.....	48
5.4.8	Interface-capturing scheme.....	49
5.4.9	Wall function.....	50
5.4.10	Grid generation.....	50
<b>CHAPTER 6 DISCUSSION OF RESULTS.....</b>		<b>51</b>
6.1.0	Experimental results.....	51
6.1.1	The Reynolds number effect.....	52
6.1.2	The Energy o-efficient $\alpha$ and momentum co-efficient $\beta$ .....	53
6.1.3	Velocity distribution and percentage area of reversal flow.....	55
6.1.4	Transition flow characteristics with a hump.....	56
6.1.5	Effect of vane on transition flow characteristics.....	56
6.1.6	Turbulent kinetic energy and turbulence intensities.....	57
6.1.7	Turbulence intensity diagrams.....	58



6.2.0	Numerical simulation.....	60
6.2.1	Turbulence model.....	61
6.2.2	Boundary conditions.....	61
6.2.3	Solution procedure.....	61
6.2.4	Discussion of results.....	62
6.2.5	Velocity distribution data for the case of no hump.....	62
6.2.6	Velocity distribution for the case of a single vane splitter.....	63
6.2.7	Velocity distribution for the case of 3-vane splitter.....	64
6.2.8	Boundary shear stress.....	64
6.2.9	Velocity Distribution for the case of 25 mm hump.....	65
<b>CHAPTER 7 CONCLUSIONS AND RECOMMENDATIONS.....</b>		<b>66</b>
7.1	Conclusions.....	66
7.2	Recommendations.....	67
<b>REFERENCES.....</b>		<b>109</b>
<b>APPENDIX-A</b>	<b>Secondary flow characteristics.....</b>	<b>114</b>

## LIST OF FIGURES

Fig. 1.1 Plan of open channel expansions.....	4
Fig: 2.1. Boundary-layer flow showing the separation point S (Schlichting, 2000).....	5
Fig 2.2 Stagnation Point Flow, after H. Fottinger (1933), (a) Free Stagnation-point flow without separation, (b) Retarded stagnation-point flow, with separation (Schlichting, 2000).....	6
Fig 3.1 Plan of open channel transition with elevation of two humps.....	27
Fig 3.2 Open channel transition with 3 vanes .....	28
Fig 4.1 Specific energy diagram for a transition.....	35
Fig. 6.0.1 The computational domain for simulation.....	62
Fig.6.1-6.15 Velocity contours and velocity distribution.....	68
Fig. 6.16-6.24 Turbulence kinetic energy.....	83
Fig. 6.25-6.33 Turbulence intensity.....	92
Fig. 6.34        Simulation without Hump/Vane.....	101
Fig.6.35        Axial velocity contours without hump for Section 1-1: (a) Experimental (b) Numerical, Section 4-4: (c) Experimental (d) Numerical, Section 5-5: (e) Experimental (f) Numerical.....	102
Fig. 6.36        Flow simulation with vanes.....	103
Fig. 6.37        Flow simulation with 1 vane.....	104
Fig.6.38        Axial Velocity Contours with 1 Vane for Section 1-1: (a) Experimental (b) Numerical, Section 4-4: (c) Experimental (d) Numerical,	

	Section 5-5: (e) Experimental (f) Numerical.....	105
Fig. 6.39	Simulation with 3 vanes.....	106
Fig.6.40	Axial Velocity Contours with 3 Vanes for Section 1-1: (a) Experimental (b) Numerical, Section 4-4: (c) Experimental (d) Numerical, Section 5-5: (e) Experimental (f) Numerical.....	107
Fig. 6.41	Boundary shear stress.....	108

## LIST OF TABLES

Table 2.1	Efficient angle of divergence.....	14
Table 2.2	Loss co-efficient for different transitions.....	22
Table 2.3	Summary of separation methods in channel expansions.....	23
Table 2.4	Flow regimes in separation process.....	25
Table 6.1	Flow characteristics of laboratory experiments.....	52
Table 6.2	Variation of $\alpha$ and $\beta$ with Reynolds Number.....	54
Table 6.3	Variation of % of area of reverse flow field with inlet Reynolds number.....	55
Table 6.4	Table 6.4 Boundary shear stress in channel transition.....	65
Table B.1	Sample calculation of the values of $\alpha$ and $\beta$ .....	136

**LIST OF SYMBOLS**

$a$  = Velocity co-efficient

$\beta$  = Momentum co-efficient

$\gamma$  = Specific gravity of water

$\delta$  = Boundary layer thickness

$\varepsilon$  = Rate of energy dissipation

$\omega$  = Specific rate of dissipation

$\mu$  = Molecular viscosity

$\nu$  = Kinematic viscosity

$\rho$  = Density of water

$K$  = Total kinetic energy

$k$  = Turbulent kinetic energy

$\tau$  = Shear stress

$\theta$  = Angle of Transition

$u, v, w$  = Velocity components in  $x, y, z$  direction

$p$  = Pressure

$q$  = Discharge per unit width

$E$  = Total energy

$H$  = Total head

$E_m$  = Mean kinetic energy of flow

$R$  = Hydraulic radius

$U$  = Average velocity

$V$  = Maximum observed velocity

$V_m$  = Weighted mean velocity

$\Delta P$  = Change in pressure between two points

$\Delta A$  = Elementary area of flow corresponding to velocity  $v$

## **Chapter 1**

### **Introduction**

#### **1.1 General remarks**

Flow separation in open channel expansion has been identified as one of the major problems encountered in many hydraulic structures such as irrigation networks, bridges, flumes, aqueducts, power tunnels and siphons. In most of these cases, the flows are generally subcritical in nature. In such expansions, the divergent flow can lead to a continuous reduction of kinetic energy and its conversion in part to pressure energy. During this process, some energy is lost due to changing flow condition in the channel expansion. Moreover, the presence of adverse pressure gradient causes flow separation due to the inability of flow to adhere to the boundaries and subsequent formation of eddies resulting significant head losses. In such cases control of flow separation is required to reduce bed and bank erosion. Moreover, minimizing the head loss in irrigation canals increases the command area served by them. In the past, efforts have been made to design efficient transition walls to avoid flow separation. Secondary measures have also been taken to control flow separation by the aid of splitter walls (vanes), baffles, humps etc to supplement primary measures. Despite extensive theoretical and experimental investigations on expansions in close conduits, the research on open channel expansions has comparatively been less in number and more in terms of one dimensional analysis. Therefore, it is desirable in hydraulic engineering to investigate structures of open channel expansions to evaluate the velocity distribution, boundary shear distribution, to control flow separation, and to design hydraulic structures properly. These measures are also needed to assist the

problems encountered in sediment transport, wastewater and pollutant transport phenomena.

Earlier investigators (Chaturvedi 1963, Smith 1966, Soliman 1966, Kline 1962, Feil 1962, Daugherty 1962) have carried out a few studies in this field and suggested various methods to suppress flow separation. Although their initial contributions are laudable, yet most of the studies on expansion are limited to one dimensional flow and lack quantitative data. This is especially true for the case when vanes are used to reduce separation in transitions. Recent flow measurements techniques and digital technology like Laser Doppler Anemometry (LDA) have created new opportunity to investigate complex flow characteristics of open channel expansion and broaden our present level of knowledge on these areas which may help to provide new engineering design inputs when field conditions are encountered.

## **1.2 Objective of the study**

The objectives of the study are enumerated below:

1. To determine mainly the mean velocity profile of subcritical flows in rectangular open channel transitions, and to determine the boundary shear stress of the channel bed. The latter is limited to a few select cases.
2. To determine the effects of hump in reducing flow separation and its adverse effects, to investigate the effect of splitter vanes to reduce or remove flow separation and in turn to reduce energy losses.
3. To collect limited turbulence data using Laser Doppler Anemometer (LDA) for possible later model validation.



4. To conduct a few numerical simulations as an alternative to experiment and to compare the predicted numerical simulation data with the experimental data.

### **1.3 Scope of the study**

The present study is mainly experimental supplemented by a few numerical simulations. The analysis was performed using the current data collected as well as the available existing data. To this end, a Plexiglas rectangular laboratory model was constructed to facilitate data collection by the Laser Doppler Anemometer (LDA). Flow separation was visualized using dye techniques in some cases.

A 325 mm long transition with  $19.78^\circ$  divergent angles was connected with a 171 mm wide straight upstream and 284.5 mm wide down stream horizontal rectangular open channels (Fig.1.1).

Two humps of 12.5 mm and 25 mm were formed by raising the bed level in the expanding section. They were installed to see the effects of hump as a flow separation control device.

Two sets of split vanes, one with a single vane and the other with three vanes in the transition were used to study the effect of vanes in reducing the separation and to collect quantitative data for turbulent characterization.

An inclined (1:5) manometer was mounted to get pressure reading at different height of the transitional section of the channel. It could read the water level to the nearest mm

The ranges of parameters (Froude's numbers, Reynolds numbers, velocity and discharge) were varied during the tests.

A limited number of CFD numerical simulations were also conducted. These included the use of devices such as humps and splitter vanes that were placed in the transition. The predictions of simulation were compared with the test data.

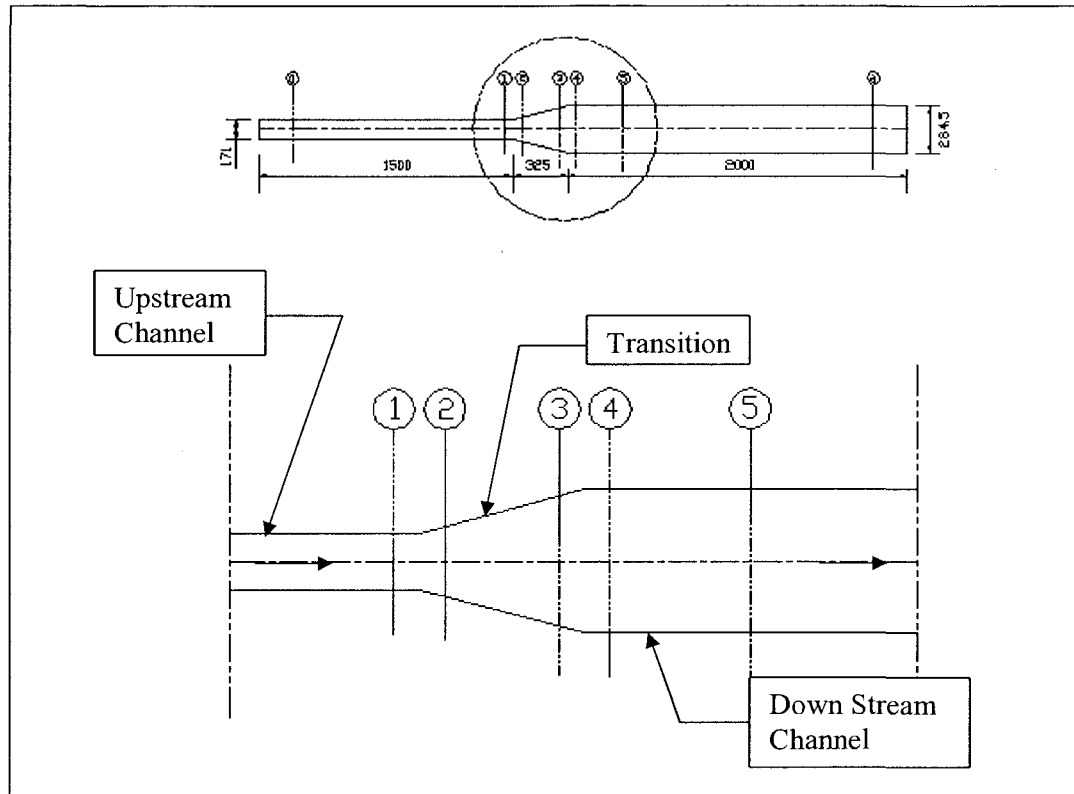


Fig. 1.1 Plan of open channel expansion

## CHAPTER 2

### LITERATURE REVIEW

#### 2.1 Flow separation mechanism

Flow separation occurs when the velocity at the stationary wall is zero or negative, and an inflection point exists in the velocity profile. Moreover, a positive or adverse pressure gradient occurs in the direction of flow. Channel expansion or contraction, sharp corners, turns and high angles all represent decelerating flow situations where the fluid in the boundary layer loses its kinetic energy leading to separation. The flow separation of a boundary layer is depicted in the Fig. (2.1). The position of the separation can be given by the condition that the velocity gradient perpendicular to the wall vanishes at the wall, i.e. the wall shear stress  $\tau_w$  vanishes (Schlichting, 2000):

$$\tau_w = \mu \left( \frac{\partial u}{\partial y} \right)_w = 0 \text{ (Separation)} \quad (2.1)$$

The point of separation can be determined by solving boundary layer differential equations.

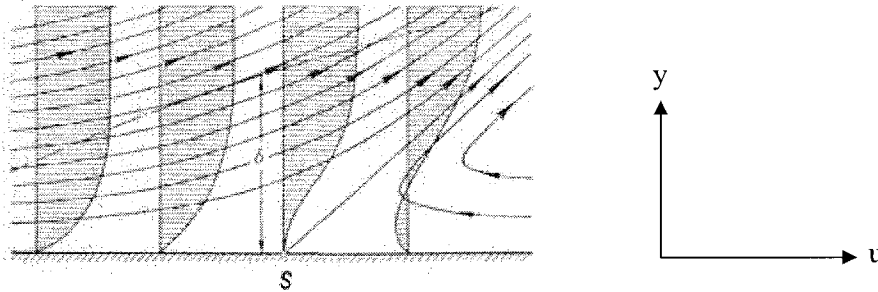


Fig: 2.1. Boundary-layer flow showing the separation point S (Schlichting, 2000)

Flow separation accompanying an expansion in an open channel results in the increase of depth in the expansion and flow separates from the walls. Fig. 2.2a shows the flow against a normal wall. There is an adverse pressure gradient in the direction of flow due to the presence of a symmetrical central streamline. However, there is no flow separation. In the fig.2.2b shows the condition in which a boundary layer with adverse pressure gradient exists due to the presence of a very thin splitter plate placed at right angles to the wall. Hence, the boundary layer formed along the splitter plate separates from the splitter plate. Thus, flow separation is extremely sensitive to small changes in the shape of the body. Flow separation in subcritical steady flow occurs in decelerated flow i.e., when  $\frac{dp}{dx} > 0$ . It also occurs when there is an abrupt change in the wall alignment.

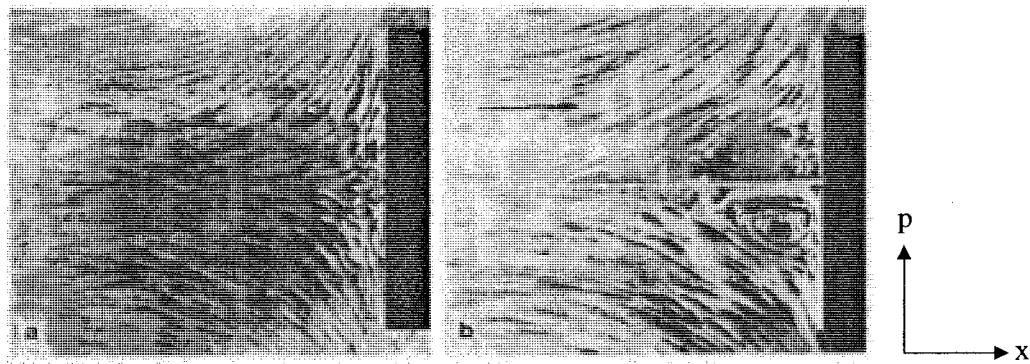


Fig 2.2 Stagnation Point Flow, after H. Fottinger (1933), (a) Free Stagnation-point flow without separation, (b) Retarded stagnation-point flow, with separation (Schlichting, 2000)

Carlson, Johnston and Sagi (1967) used tufts to trace flow separation. They divided the flow into six categories according to the relative position of the tufts with the flow. (Table 2.4)

The first attempts at describing separated flow past blunt bodies are due to Helmholtz and Kirchhoff in the framework of the classical theory of inviscid fluid flows. There was no adequate explanation as to why separation occurs. Prandtl (1904) was the first to recognize the physical cause of separation at high Reynolds numbers as being associated with the separation of boundary layers that must form on all solid surfaces.

Flow development in the boundary layer depends on the pressure distribution along the wall. If the pressure gradient is favorable, i.e. the pressure decreases downstream, then the boundary layer remains well attached to the wall. However with adverse pressure gradient, when the pressure starts to rise in the direction of the flow, the boundary layer tends to separate from the body surface.

## 2.2 Boundary layer flow

A boundary layer consists of a thin region adjacent to solid surfaces and a substantial region of inertia-dominated flow far away from the wall. The flow very close to the wall (viscous sub-layer) is influenced by viscous effects and does not depend on free stream parameters. The mean flow velocity depends on the distance  $y$  from the wall, fluid density  $\rho$  and viscosity  $\mu$  and the wall shear stress  $\tau_w$ .

Therefore,

$$U = f(y, \rho, \mu, \tau_w) \quad (2.2)$$

Dimensional analysis shows that

$$u^+ = \frac{U}{u_\tau} = f\left(\frac{\rho u_\tau y}{\mu}\right) = f(y^+) \quad (2.3)$$

The equation (2.3) is the law of the wall and contains two important dimensionless parameters  $u^+$  and  $y^+$ . The parameter  $u_\tau = (\tau_w / \rho)^{1/2}$  is the shear velocity.

The boundary layer thickness  $\delta$  is defined as the distance away from the surface where the velocity reaches 99% of the free-stream velocity. In this region, the velocity  $U = U(x)$  in the axial (x) direction depends on several parameters (Eq. 2.4).

$$U = g(y, \delta, \rho, \tau_w) \quad (2.4)$$

Here,  $y$  = distance from the wall,  $\delta$  = boundary layer thickness,  $\rho$  = density of water,

$\tau_w$  = wall shear stress.

Dimensional analysis gives

$$u^+ = \frac{U}{u_\tau} = g\left(\frac{y}{\delta}\right) \quad (2.5)$$

There is a linear sub-layer- formed by the fluid layer in contact with a smooth wall.

This layer is extremely thin ( $y^+ < 5$ ) and the shear stress is almost constant and equal to the wall shear stress  $\tau_w$  throughout the layer. It is given by

$$\tau(y) = \mu \frac{\delta U}{\delta y} \cong \tau_w \quad (2.6)$$

Integrating with respect to  $y$  and applying boundary condition  $U=0$  if  $y=0$ , a linear relationship between the mean velocity and the distance from the wall is established.

$$U = \frac{\tau_w y}{\mu} \quad (2.7)$$

There is a region outside the viscous sub-layer ( $30 < y^+ < 500$ ) where viscous and turbulent effects are both important. The shear stress  $\tau$  varies slowly with distance from the wall and within this inner region it is assumed to be constant and equal to the wall shear stress. In this region there is a dimensionally correct form of the functional relationship between  $u^+$  and  $y^+$

$$u^+ = \frac{1}{k} \ln y^+ + B = \frac{1}{k} \ln(Ey^+) \quad (2.8)$$

Here,  $k=0.4$ ,  $B=5.5$ , (or  $E=9.8$ ) for smooth wall. Because of the logarithmic relationship between  $u^+$  and  $y^+$ , the above formula is called the log-law and the layer where  $y^+$  takes the values between 30 and 500, the log-law layer.

### 2.3 Losses in open channel transitions

A channel transition may be defined as a change in the direction, slope, or cross section of the channel that brings a change in the flow condition. Though all transitions of engineering interest are relatively short features, yet they may affect the flow for a great distance upstream and downstream (Henderson, 1966). Again, the design and performance of transitions are critically dependent on sub-critical and super critical flow regimes. The calculation of energy losses and determination of the transition profile to provide a good velocity distribution at the end of the transition, are two problems areas that need the attention of hydraulic engineers.

In pipe flow, the energy loss in sudden expansion is calculated by the following expression (Daugherty et al, 1954)

$$\Delta E = \frac{C_L(V_1 - V_2)^2}{2g} \quad (2.9)$$

Here,  $\Delta E$  = loss of energy between section 1 and 2,

$V_1$  = Velocity at section 1,

$V_2$  = velocity at section 2,

$C_L$  = loss coefficient

Formica, (1955) applied the above expression in open channels and obtained an average value of  $C_L$  in the range of 0.41 to 0.87 for different channel expansions. The values obtained by Chaturvedi et al (1963) are enumerated in tables (Table 2.1 and Table 2.2). It was found that the values of  $C_L$  increase with the devices used to reduce flow separation.

Another expression made by Hinds (1928) for energy loss in gradual expansion is given by

$$\Delta E_L = K\Delta E_v \quad (2.10)$$

where,  $\Delta E_L$  = energy loss along the channel length,

$K$  = loss coefficient the value of which varies between 0.2 and 0.3



$\Delta E_u$  = the change in velocity heads between the two sections under considerations, viz.  $\left( \frac{V_1^2}{2g} - \frac{V_2^2}{2g} \right)$

Formica (1955) presented experimental data showing energy losses in sudden expansions some 10 % less than those given by Eq. (2.9). Experiments were carried out by Mishra (1977) where depth  $h_1$ ,  $h_2$ ,  $h_3$  were not very different from one another. The energy loss in his experiments with  $B_1/B_2$  ranging from 1.33 to 2.0 was 1.6 to 4.0 times that given by Eq. (2.9). Thus the energy loss in the case of an abrupt flow does not agree well with the theory of closed conduit flow.

A special feature of the flow in an expansion connecting rectangular conduits of widths  $B_1$  and  $B_2$  is found to be the lack of symmetry when the expansion ratio is large. Abbott et al. (1962) studied diffuser flows and found that the length of the eddy on both walls is the same as long as  $B_1/B_2 \leq 1.5$  but at larger values of  $B_1/B_2$ , the eddy on one side becomes larger than on the other and the centre line of the channel no longer remains the line of maximum velocity. The eddy lengths are independent of Reynolds number  $R_e$  and are dependent on  $B_1/B_2$ .

Millsaps et al. (1953) investigated flow in an open channel expansion and plotted a series of velocity profiles for different Reynolds numbers. The results show that when the Reynolds number is large, the velocity is positive over the entire cross section and at lower Reynolds numbers; reverse flows are observed near the walls denoting flow separation. Hamel (1916) found that for larger angles of divergence, flow separation occurs earlier, at lower Reynolds numbers.

The divergent angle plays an important role in flow separation. When the divergence angle  $\theta$  is small flow through expansions can be non-uniform but not necessarily very unsteady. The transitional flow is sometimes theoretically called irrotational. This is because of non uniform pressure distribution and high degrees of eddying due to flow separation. The pressure distribution may not be truly hydrostatic because of transverse and vertical velocity components.

Chaturvedi (1963) found that when the curvature of divergence is high, the domination of local stresses will prevail due to pressure variation and lateral inertial forces.

#### **2.4 Turbulence characteristics in channel transition**

Open channel flows are regularly turbulent in nature. Turbulent fluid flow is an irregular condition of flow characterized by diffusivity, large Reynolds number, 3D-vorticity fluctuations, dissipations, and continuum in nature. Turbulence is better described by its eddy motion. It consists of a continuous spectrum of largest to smallest eddies having swirling motion generating kinetic and dissipating to thermal energy. Turbulence represents the “cascade process” that occurs in the atmosphere. In another words, energy associated with large-scale motion generates larger eddies. The larger eddies transfer this energy to smaller ones and these smaller scales eddies then transfer the energy to the next smallest eddies. Eventually, the energy is dissipated into heat through molecular viscosity. In the study of turbulence, the generation and dissipation of turbulent kinetic energy are very important phenomena.

General hydraulic and transport model assumes that flows in open channels are uniform and unidirectional (Papanicolaou et al. 2001). Despite few successes, those models may under predict or over predict sediment transport, scouring in the natural channel due to the presence of secondary flows ( MaLelland et al. 1999). Prandlt

(1955) identified two types of secondary flows such as (i) skew-induced secondary flow called secondary flows of Prandtl's first kind and (ii) stress induced secondary flow or secondary flows of Prandtl's second kind due to anisotropy of turbulent fluctuations. The stress induced secondary flows are generated due to the channel transitions and bed undulations. Though several studies were conducted on secondary flows on meandering channel and bed form, very few studies were carried out on turbulent flow characteristics in channel transitions. Sukhodolov et al. 1998). Mehta (1981) and El—Shewey and Joshi (1996) investigated the effects of a sudden channel expansion on turbulence characteristics over smooth surfaces. They found that the high intensity turbulence occurs either close to the surface or near the bed because of the Prandtl's second kind secondary flows developed at the channel transitions.

## **2.5 Geometry of divergence to control flow separation**

Nikauradse (1962) conducted experiments to determine an efficient angle of divergence to see the separation characteristics of flow. The observations reported by him are given in Table 2.1.

Table 2.1 Efficient angle of divergence (Nikauradse, 1962)

Total divergence angle $\theta$	Observations
$\theta = 8^{\circ}$	Velocity profile is fully symmetrical over the width of the channel and shows no features associated with separation.
$\theta = 10^{\circ}$	Velocity profile seems to be symmetrical. Separation has just started to occur on one of the channel walls. Flow becomes unstable and adheres alternatively to the one or other wall of the channel. Such instability is the characteristics of incipient separation.
$\theta = 12^{\circ}$	Lack of symmetry is observed and the flow has completely separated from the walls.
$\theta = 16^{\circ}$	Width of the region of reversed flow is comparatively larger than for $\theta = 12^{\circ}$ . Frequent oscillation of the stream from one side to the other is observed.
$\theta > 16^{\circ}$	Region of reversed flow becomes wider and the pulses are more frequent.

Abramowitz (1949) found theoretically that a point of separation moves downstream of the channel when the Reynolds number is increased and the angle of divergence is decreased.

Rouse (1946) conducted experimental study on sub critical flow and found that there is no minimum angle for which separation will not occur because the limiting angle by boundary layer analysis has been shown to decrease with increasing length of the transition.

Smith et al.(1966) have found that the total divergence angle  $\theta$  should not be more than  $11^{\circ}16'$  to avoid flow separation. Separation occurs when the total divergence angle is increased to  $\geq 19$  (except for  $B_1/B_2 < 1$  to 2).

## 2.6 Design considerations for transitions

Different aspects of designing transitions investigated by different researchers are enumerated below:

The distribution of mean velocity at the inlet to the expansion influences the energy lost in the expansion and the efficiency of the system. High ratios of centre velocity to mean velocity in the cross section give poor efficiencies and high energy loss. When there is adequate and proper lateral distribution of momentum, there will be no flow separation at all (Chaturvedi, 1963).

A uniform velocity at the exit is more desirable to minimize energy loss as a uniform velocity distribution produces lower exit velocity for a given flow rate and lowest rate of momentum out flow and thus maximizes pressure rise and minimize exit losses (Waitman et al. 1961). Efficient conversion of kinetic energy to pressure energy plays an important role for an efficient transition design (Chaturvedi, 1963). Gradual expansion can minimize the adverse pressure gradient. Hence the probability of separation is reduced when the pressure gradient  $\frac{dp}{dx}$  is lower as the angle of divergence is smaller (Chaturvvedi, 1963)

## 2.7 Method of control of flow separation

The loss of momentum or energy due to flow separation is detrimental for a diffuser or channel transition. Probable solutions may be the prevention of the initial occurrence, early elimination, or some reduction. Prevention or reduction of separation has little difference. They essentially differ only in the degree of control required. Control techniques are broadly classified as (a) devices without auxiliary power and (b) auxiliary powered devices. The flow separation from a continuous surface is governed by two factors, adverse pressure gradient and viscosity. In order to remain attached to the surface, the flow must have sufficient energy to overcome the adverse pressure gradient, the viscous dissipation along the flow path, and the energy loss due to the change in momentum. This loss has a significant effect on the channel walls where momentum and energy are much less than in the outer part of the boundary layer. If the loss of energy is so much that the fluid cannot move ahead, then the flow separates from the wall. On the contrary, if the momentum and energy adjacent to walls are sufficient, then no separation occurs. Hence, techniques for controlling flow separation are either (a) to design the body surface configuration in such a way that a sufficiently high energy level is maintained along the flow path near the walls or (b) to boost the energy level by a physical device placed at a suitable position along the flow path (Chang, 1976).

The dilemma is to maintain sufficient energy level of the fluid along the flow path to overcome the pressure rise and viscous friction in the boundary layer. In the past, various methods have been adopted to achieve this condition. These are as follows:

- (a) Elimination of viscosity effect by suction of boundary layer: Suction removes the deceleration of flow particles in the neighborhood of the wall and hence prevents flow separation.
- (b) The increasing momentum of the surface fluid: The mixing of shear layer particles can be increased by using an auxiliary device attached to the main body. The mixing raises the turbulence level so that momentum and energy in the vicinity of the wall are augmented to prevent the separation that would otherwise occur. Vortex generators are used to transport energy into the boundary layer and shed vortices downstream of a vortex generator bring higher kinetic energy into the more slowly moving fluid. Thus, vortex generator helps to reenergize the fluid near the surface.
- (c) Another possible technique for preventing extended down stream separation to provide an abrupt change of the geometry configuration in a region of the flow path in an open channel transition is by the use of vanes. The vanes reduce the angle of expansion and reduce the tendency for flow separation.
- (d) Proper design of the basic wetted surface configuration: The stream-wise pressure gradient may be made favorable or adverse by designing concave or convex surfaces or by changing wall shape i.e., wall contouring. Moving of the walls with the stream in order to reduce the velocity difference between them, and reducing the cause of boundary layer separation.

Methods (a) to (c) listed above are subjected to efficiency loss despite their contribution to prevent separation. Method (d) does not involve any external device. Hence it does not create any obstruction to flow passage of the fluid. Based on the above control techniques the following methods have been used to prevent flow separation (Rao, 1967).

- (i) Square baffles for rapid expansion (Smith et al., 1966)
- (ii) Stream lined baffles (Gaylord et al., 1966)
- (iii) Triangular baffles adopted in trapezoidal expansion (Gaylord et al., 1966)
- (iv) Pyramidal Hump (Dake et al. 1967)
- (v) Adversely slopping bed with warped side walls (Dake et al., 1967)
- (vi) Bed deflector with warped side walls (Dake et al., 1967)
- (vii) Vanes with warped side walls (Dake et al., 1967)
- (viii) Boundary layer suction by connecting pipes at the sides of entrance and expansion ( Rao , V et al., 1966)
- (ix) Vane angle system at entrance for wide angle diffuser (Feil, O. G. 1962)
- (x) Changing the wall contouring (Chaturvedi 1963 & Dake et al., 1967)
- (xi) Bowing the bed transverse to the flow axis (Montagu, 1934)
- (xii) Longitudinal hump (Ramamurthy et al., 1967)
- (xiii) Longitudinal hump with larger divergence angle ( Present Study)
- (xiv) Splitter Vanes : single and multiple (Present Study)

The performances of the above methods are summarized in Table 2.3

Ramamurthy et al. (1967) suggested that the use of a simple hump in an expanding transition accelerates the flow and hence reduces flow separation and limits the area in which the reversal of flow occurs. The present study is an extension of concept proposed earlier. No extensive experimental study was conducted earlier about the performance of the humps. The present study aims at verifying the effectiveness of humps in larger expansion angles, to investigate the



possibility of using splitter vanes, and finally to conduct a few numerical simulations by CFD analysis in 3-dimensional perspective.

## 2.8 Some previous methods of transition design

Extensive theoretical and experimental investigations on axisymmetric expansion in pipes have been done ( Gibson et al., 1912, Chaturvedi, 1963, and Kalinske, 1946). The approaches for design of open channel expansions have comparatively been lesser in number and more empirical in nature. Hinds (1926) was the first to give a basis for such a design.

Mitra (1940) devised a simple design for an expansion transition based on the assumptions of a constant depth and a constant rate of change of velocity with distance. The expression for the expansion is hyperbolic in nature.

$$B_x = \frac{LB_c B_f}{LB_c - x(B_c - B_f)} \quad (2.11)$$

Here,  $L$  = the length of the transition,  $B_c$  = the full width, and  $B_f$  = flumed width of the channel and  $B_x$  = the width at a distance from the beginning of the expansion. The transitions designed with above equation have been found to work satisfactorily in practical situations. But it has the limitation of assuming constant depth of flow which is not justified.

Chaturvedi (1963) derived an equation for the expansion transition more or less similar to one as Mitra. The equation of the general transition curve was given by

$$x = \frac{LB_c^n}{B_c^n - B_f^n} \left[ 1 - \left( \frac{B_f}{B_x} \right)^n \right] \quad (2.12)$$

Which is eventually reduces to Eq. 2.11 when  $n=1$ . On the basis of his experimental results, he found that a transition designed with above equation performs better than Mitra's hyperbolic transition when the value of  $n=3/2$ .

Rai et al., (1969) further studied the boundary layer separation for the above two transitions. Misra et al., (1984) designed an expansion transition using the concept of minimum head loss in the expansion. The profile designed on the basis of this concept has been tested and found to give better performance in terms of efficiency in comparison with Chaturvedi's transition under similar conditions.

## **2.9 The present study related to flow separation in rectangular open channel transitions**

The present technique for preventing flow separation suggests providing a hump which will eventually change the geometry of the transitional bed. It is done by a gradual elevation of the bed level in the expansion region which allows the pressure gradient to decrease in the longitudinal direction. Again, after reaching the summit at the end of the expansion it is gradually brought back to the initial level following equal negative slope. This helps the decelerated flow to accelerate and reduce the extent of flow separation. The theoretical considerations associated with it are discussed in the next chapter. The humps used in this study start at section1 (Fig. 1.1) and rise gradually up to a height of 12.5 mm and 25 mm at the end of the expansion of length of 325 mm and falls gradually along the down slope ending to the original bed level after reaching an equal length of 325 mm.

The unique advantage of using a hump is that it does not obstruct the flow along the channel.

Another method of reducing flow separation is to provide a splitter vane system. This method has qualitative data but there is no existing quantitative data. Providing a vane or a system of vanes actually makes transition angle smaller. Hence, it reduces flow separation. In the present study, data was collected with a single vane and with a system of three vanes placed in the transition region of the channel.

Moreover, turbulent intensity data were collected in order to develop a data bank for validation of future simulation studies.

Table 2.2 Loss co-efficient for different open channel transitions

Sl. No	Type of Experiments	Researchers	$B_2/B_1$	$\theta$	$V/V'$	Loss coeff.	Comments
1	2	3	4	5	6	7	8
1	Rapid expansion	Smith & James(1966)	-	$28^{\circ}10'$	2.5	0.5	Scouring is imminent. Large eddy between jet and side walls.
2	Rapid expansion with 3 baffles	Smith & James (1966)	3.0	-	1.26	0.8	Practically no scour. Movable bed in the d/s is used. When velocity is reduction is important this may be more suitable
3	Gradual expansion	Smith & James(1966)	-	$11^{\circ}26'$	2.10	-	-
4	Straight walled flared gradual expansion	Chaturvedi (1963)	-	$19^{\circ}$	-	0.25	-
5	Curved wall flared transition	Chaturvedi (1963)	-	$38^{\circ}$	-	0.40	Central angle gradually increases
6	Abrupt outlet	Smith&James (1966)	3.0	-	-	1.08	-
7	Abrupt outlet	Smith & James(1966)	1.5	-	-	1.02	-
8	Baffled outlet (rapid expansion)	Smith & James(1966)	3.0	-	-	0.84	-
9	Baffled outlet (rapid expansion)	Smith & James(1966)	4.0	-	-	0.77	-

Notes: (1) denotes data unavailable.

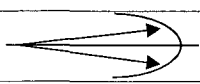
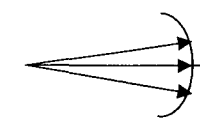
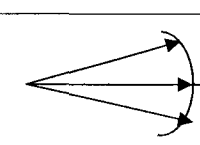
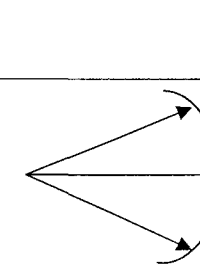
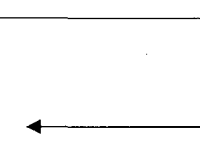
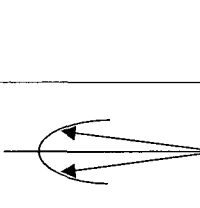
Table 2.3 Summary of methods to reduce separation in channel expansions

Sl. No.	Type of Device	Reference	Efficiency of Reverse Flow	Efficiency with respect to total head loss	Hydraulic Structures	Comments
1	2	3	4	5	6	7
1	Square baffles with rapid expansion	Smith & James (1966)	Very efficient	Not Efficient	May be used in expansion from lined to an unlined section of a canal, siphon outlet, a flume outlet or a culvert outlet	Scoured reduced completely. Velocity distribution at the outlet is more uniform than that of gradual expansion. Large scale debris clogging the baffles is probable-suitable when velocity reduction is more important
2	Streamed baffles	Soliman (1966)	May not be as efficient as #1	Better than #1	May be used in a transition of a lined canal	-----
3	Triangular baffles adopted in trapezoidal expansion.	Skogerboe & Hyatt (1966)	No separation was observed for both supercritical and sub critical flows.	Head loss is found to be same with or without baffles.	Can be used in trapezoidal expansion.	Clogging of channel is possible due to large scale debris.
4	Pyramidal Hump	Dake (1967)	Reduced reverse flow is expected	--	Suggested in super critical flows from a closed conduit.	Flow is found to spread at the outlet- suitable when channel is having large scale debris.
5	Adverse sloping bed with warped side walls	Kulaindaiswamy & Narayanam (1967)	--	--	May be adopted to improve performance of existing expansion.	Studies done are only of qualitative nature.
6	Bed deflector with warped side walls	Kulaindaiswamy & Narayanam (1967)	Reduces or avoids reverse flow	--	May be adopted to improve performance of existing expansion	--

Contd. Table 2.3

Sl. No.	Type of Device	Reference	Efficiency of Reverse Flow	Efficiency with respect to total head loss	Hydraulic Structures	Comments
1	2	3	4	5	6	7
7	Vanes with warped side walls	Kulaindaiswamy & Narayanam (1967)	More efficient than (6)	--	--	---
8	Self induced suction by connecting pipes	Vasudeva Rao (1966)	--			Can be fitted to existing transitions. Auxiliary equipment required is minimum. Probability of pipe choking up is more with channels carrying heavy concentration of silt
9	Vane angle system for very wide angle diffusers	Feil (1962)	--	--	--	Performance of this diffuser was found to have improved.
10	Changing the wall contouring	Chaturvedi (1963) & Narayanan(1967)	Reverse flow was found to have reduced	--	--	Best suited when head losses can not be ignored.
11	Bowing the bed in the transverse direction.	Montager (1934)	--	--	--	Downstream bed is curved across the width instead of leaving it flat.
12	Providing a straight hump in the longitudinal direction	Ramamurthy(1966)	Hump height was variable for different expansions to reduce reverse flow.	Head losses was minimum	May be adopted to improve flow separation in sub critical flow	Better velocity distribution and lesser chance of siltation.

Table 2.4 Flow regimes in separation process (Sagi et. al., 1967)

Tuft Pattern	Symbol	Description
	S	Steady flow-small or no oscillations of tufts.
	U	Unsteady flow- medium amplitude oscillations of tufts with no back flow observed.
	TI	Incipient transitory stall- large amplitude oscillations of tufts on the verge of the tuft pointing upstream
	IT	Intermittent transitory stall- large amplitude oscillations of tufts with the tuft pointing upstream for short periods of times
	T	Transitory stall- tuft points upstream for approximately the same period of time as it points down stream.
	F	Fixed stall- Tuft points upstream for long period of time.

## **CHAPTER 3**

### **EXPERIMENTAL SET UP**

#### **3.1 Physical model**

##### **3.1.1 Experimental channel**

The laboratory tests were performed in a Plexiglas channel designed and built for measuring flow velocities using LDA, having rectangular cross section. The upstream channel was 171 mm wide and 304.8 mm deep with an overall length of approximately 2.0 m and the down stream channel was 284.5 mm wide and 304.8 mm deep with a length of 3.0 m. These two channels are again connected by a transition of 325 mm long and 304.8 mm deep with a width of 171 mm in the upstream and 284.5 mm in the down stream respectively.

The upstream channel was connected to a large tank with an overflow section to diminish turbulent flow and the down stream channel was connected to exit gate provided to control sub critical flow in the channel. The channel flow was steady due to the overflow device. The exit flow was directed towards a V-notch to measure the discharge  $Q$  ( $m^3/s$ ). The inlet to the transition was made sufficiently long ( $> 1500mm$ ) to achieve good entrance conditions and the long exit section length ( $> 2000$  mm) was required to get fully undisturbed flow at the end. The channel walls were made of 12.5 mm thick Plexiglas sheets and were supported by external Plexiglas flange made of 19 mm Plexiglas at 325 mm spacing along the straight sections and 323.3 mm in the transition.



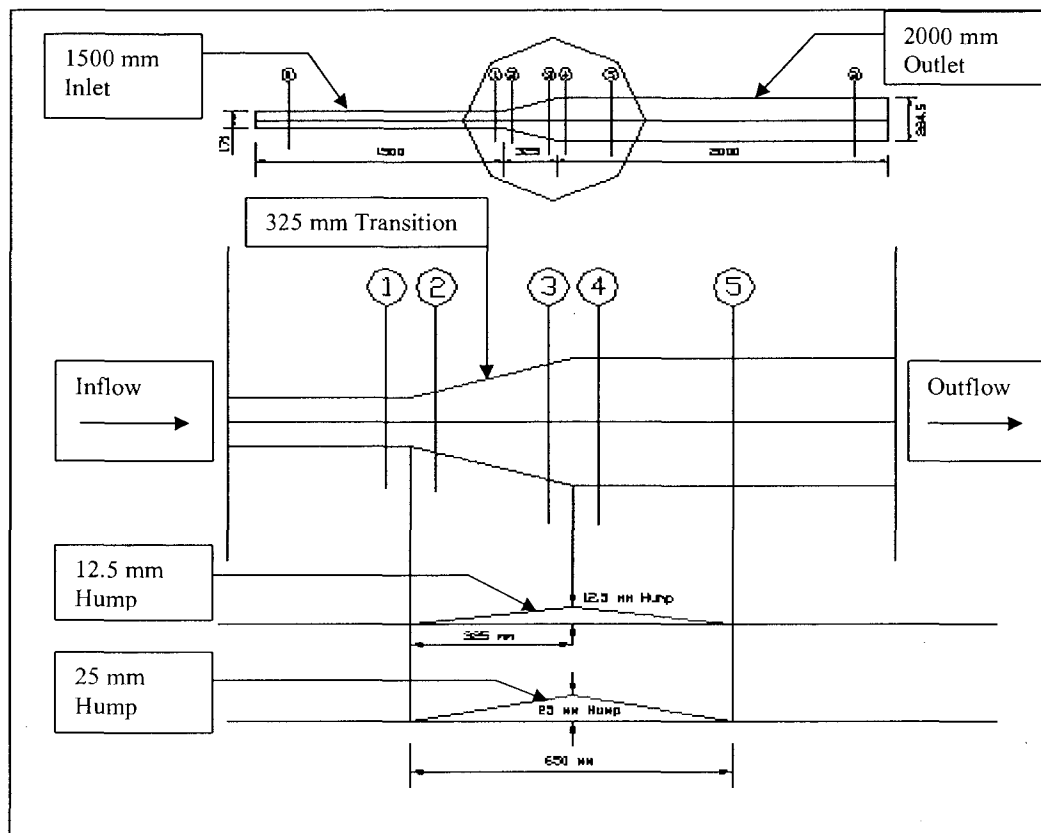


Fig: 3.1. Plan of horizontal rectangular open channel transition fitted with humps

The entire channel was supported on a steel frame on a number of identical and equally spaced steel box angle frames 1.5 m above the laboratory floor. Two wooden platforms – one at the bottom of the channel and another one at the side of the channel were erected to facilitate the movement of LDA traverse to measure velocity from the bottom as well as from the side of the channel. The spacing between the supporting sections allowed the probe to focus and measure velocities at points on the flow fields. A steady water flow was ensured in the channel through pumping water to the large tank with the overflow device. The experiments were conducted on two physical setups; one with humps and the other with vanes. Two different linear humps of 12.5 mm and 25 mm high at crests were fabricated with 1.5 mm thick Plexiglas sheets supported by wedges at the bottom. The humps were placed at the starting of transition and reached its apex at the end of maximum transition followed by a down

slope of equal magnitude of the upward slope. The experimental locations were chosen at the beginning of the transition, at the end of the transition (350 mm apart), 300 mm down stream of expanded channel.

Two sets of vanes were also constructed after finishing the experiments with humps. The first setup of vane had a single vane placed at the middle of the flow field hanging from a top support and touching the channel bed where it was sealed. The second set up of vanes consisted of three vanes spaced equally apart. The vanes were extended 225 mm upstream and 225 mm down stream from the starting of transition (Fig. 3.2).

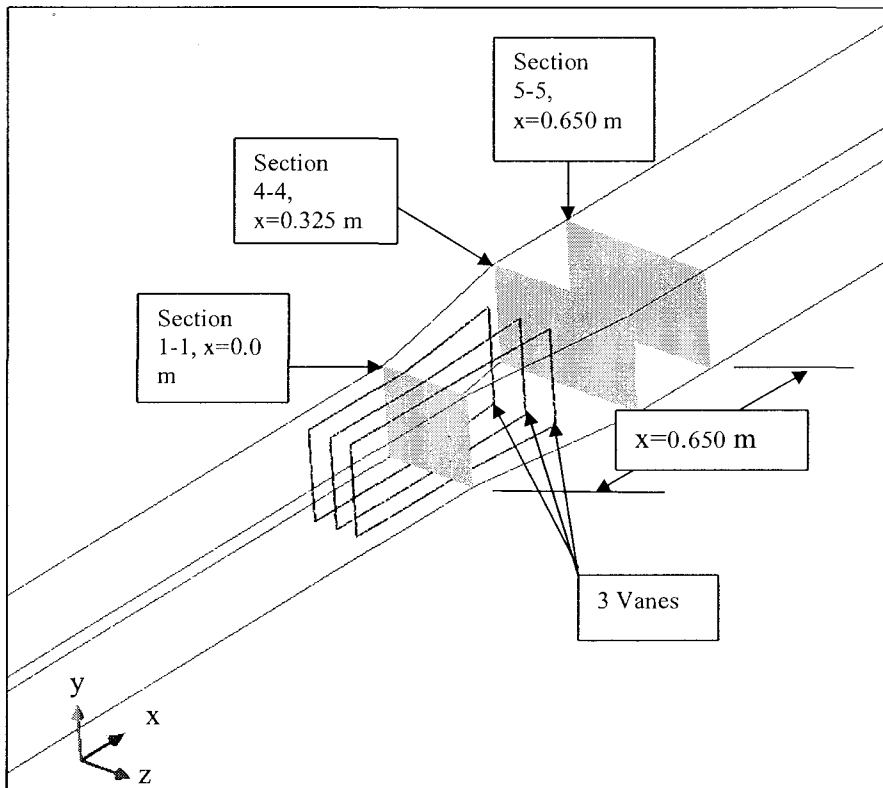
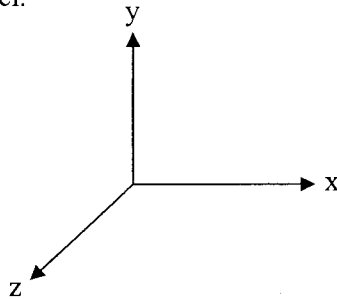


Fig.3.2 Open channel transition with 3 Vanes

## 3.2 Instrumentation

### 3.2.1 Velocity measurements

A Laser Doppler Anemometer System was used to measure velocity  $U$  (m/s) along x-axis and transverse velocity  $W$  (m/s) along z-axis positioning the probe on the bottom traverse, and vertical component  $V$  (m/s) along y-axis from the traverse placed along the side of the channel.



The DANTEC LDA system is generally, a dual beam single component system. It consists of a probe, fiber-optic cable, an optics unit and FVA enhanced signal processor. An interface card installed the computer allows the FVA to be controlled and read from the computer. This system uses a 10mW Helium Neon laser which produces light of wavelength 632.8nm. The laser and beam splitter are housed in the optics unit. A Bragg cell, used to shift the frequency of one of the beams by 40MHz is also installed here. Light from the two beams is passed through two optical fibers to the probe, where the beams are positioned and then focused using a lens. The lens also changes the direction of the beams causing them to cross at the point where they are focused and produce a tiny measurement volume, some 400mm from the sending lens. The probe operates in backscatter mode. In fact, light scattered by particles passing through the measurement volume is collected by the same lens used to focus the beams. It is then focused into a third optical fiber which carries this light back to the optics unit where it is fed into a photomultiplier (PM) tube. The nominal optical

characteristics of the system are (i) focal length = 400mm, (ii) beam separation at sending lens = 38 mm, (iii) Gaussian beam diameter at sending lens = 1.3 mm, (iv) measurement volume diameter = 0.248 mm, (v) fringe spacing =  $6.667 \mu\text{m}$ , and (vi) number of fringes in measurement volume = 37.

Signals from the PM tube are sent to the PDA processor. The burst detection criteria and processing parameters of the processor are set from the computer, which is also used to read the results. The top one labeled DOPPLER MONITOR outputs the high-pass filtered PM tube signal. The high-pass filter removes the pedestal. An oscilloscope is connected to this signal to monitor the bursts.

The laser probe is mounted on a 3-axis traverse gear made from a milling machine base. Being so heavy the traverse gear provides a stable means of positioning the measurement volume at any point in the test section. The probe mount also allows the probe to be rotated about its axis by 90 degrees, to change the component of the velocity being measured.

In the present study more advanced DANTEC BSA Flow Software, dual PDA version, was used to control the LDA system from the lab computer, and to collect the velocity measurements in two directions at a time. A third party traverse system run by another computer with the software NFTERM was used to move the probe to get different point velocities along the test sections.

For the purpose of data collection the test sections were divided, lengthwise, in to five sections and each section was subdivided into a grid along the channel cross sections. The following procedures were followed prior to actual velocity measurements:

- (i) The direction of the bisector of the two laser beams was adjusted so that it was aligned perpendicular to the channel at the section under investigation.
- (ii) The probe was then moved back and forth using the traverse controller along the traverse gear as well as along the channel until the beams intersected precisely at the required measuring point in the flow field.
- (iii) Finally PDA software was run to take the readings moving the probe along horizontal and vertical axes as required.

As its name goes Laser Doppler Anemometer, the Doppler Effect plays an important role in LDA, since the technique is based on Doppler shift of the light reflected (and/or refracted) from a moving seeding particle. The Doppler-frequency  $f_d$  can be measured as fluctuations in the intensity of the light reflected from the seeding particle. It is given by the formula suggested by Dantec,

$$f_d = \frac{2 \sin\left(\frac{\theta}{2}\right)}{\lambda} u_x \quad (3.1)$$

Here,  $f_d$  = Doppler frequency,  $u_x$  = velocity along x-axis,  $\lambda$  = wave length of Laser light ( 500 nm),  $\theta$  = the angle between the incoming laser beams

Since the Doppler frequency is directly proportional to the x-component of the particle velocity, and the velocity can thus be calculated directly from  $f_d$  :

$$u_x = \frac{\lambda}{2 \sin\left(\frac{\theta}{2}\right)} f_d \quad (3.2)$$

To measure velocities, a Bragg cell is introduced in the path of one of the laser beams. Another disadvantage is that it needs transparent flow through which the light beams can pass, and the fact that they do not give continuous velocity signals. Laser Doppler Anemometer offers unique advantages in comparison with other fluid flow instrumentation. It is a non-contact optical measurement that gives well-defined directional response, high spatial and temporal resolution, and multi-component bi-directional measurements and requires no calibration- no drift. The accuracy of the velocity measurements has 1% error margin.

### 3.2.2 Depth measurements:

In order to draw surface profiles and to compute boundary shear stresses from point velocities, the positions of the measuring points, with respect to the channel bed and the water surface, must be determined. Furthermore, accuracy in depth measurements is extremely important if errors in computations of related bed shear stress are to be minimized. Depths, surface water profiles and side water profiles were measured by a metric depth gauge that had a resolution of 0.1 mm.

### 3.2.3 Pressure head measurements:

Wall pressure head measurements taken using manometers located on the walls of the expansion section of the channels. The pressure taps were 1.6 mm in diameter. The manometers could measure the pressure head to the nearest 0.1 mm. The manometers

displayed the static head  $\left[ \left( \frac{P}{\gamma} \right) + z \right]$ . To obtain the true  $\left( \frac{P}{\gamma} \right)$  value, a datum was

established. The datum was the bottom elevation the channel when  $\left( \frac{P}{\gamma} \right) = 0$ .

#### 3.2.4 Other parameters:

The water temperatures were recorded by thermometer and typical temperature recorded was around  $20^{\circ}$  Celsius  $\pm 2^{\circ}$ . The flow rate  $Q$  was measured by diverting the flow through a calibrated V-notch located in the bottom floor of the 2-storey lab. The flow over the V-notch was measured up to the nearest 0.1 mm. The accuracy of the discharge measurement is estimated to be 3 %. (ASME Flow meter).

## CHAPTER 4

### THEORETICAL CONSIDERATIONS

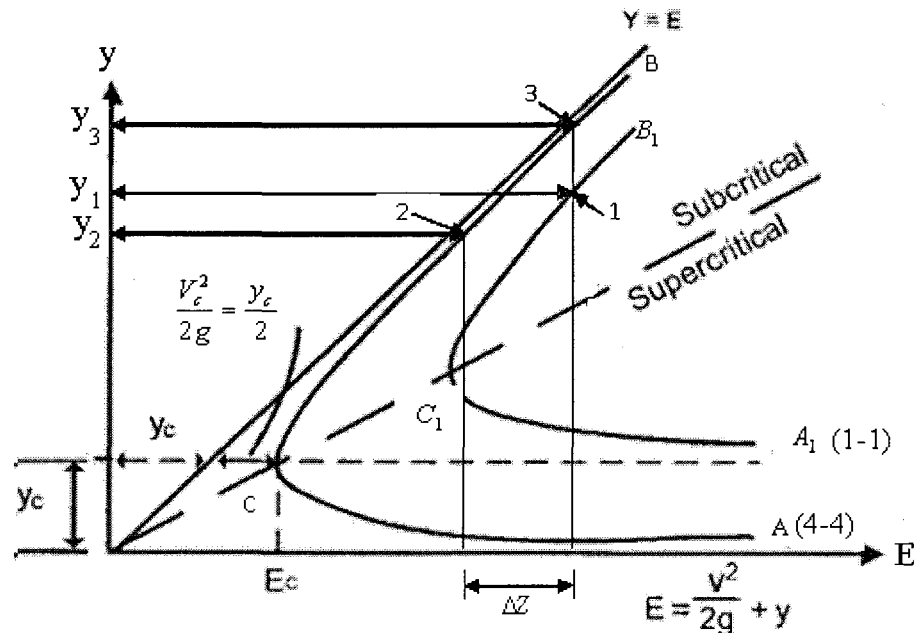
#### 4.1 Hump and its effects:

The following assumptions are made to consider the actions of humps in suppressing flow separation in a channel transition.

- (i) The pressure distribution is hydrostatic
- (ii) The original channel bed is horizontal.
- (iii) Head losses are negligible since the length between two sections is small.
- (iv) Energy coefficient  $\alpha$  is unity

The effect of hump on the flow condition is explained with the use of the specific energy diagram (Fig. 4.1). The curve 1 denoted by  $A'C'B'$  shows the energy diagram for an open channel of uniform cross section at (1)-(1) in the upstream. When the flow is under subcritical conditions and it passes through the expansion, the discharge per unit width  $q$  as well as the velocity decreases (Rao, et al., 1967). The curve for specific energy in the expansion at section (4)-(4) is shown by curve 2 denoted by  $ACB$ . Applying the energy equation, the energy at sections (1)-(1) and (4)-(4) are constant; the positions 1 and 3 represent the same energy level and remain in the same vertical line. Here, the velocity  $V_2$  decreases ( $V_2 < V_1$ ) and depth of flow  $Y_3$  increases ( $Y_3 > Y_1$ ) and thus balances the energy condition. The flow under this decelerated state experiences adverse pressure gradient, and hence flow separation may occur





Consider two values of discharge per unit width. Therefore, two E-Y curves.

Fig 4.1: Specific Energy Diagram for a Transition

resulting in an eventual energy loss in the expansion. This is a state of flow that takes place in a channel, where there is no hump or other external measures in action.

When the hump is installed in the transition, the state of flow encounters a different situation. Since the width  $B$  is not changed, the discharge per unit width  $q$  ( $Q/B$ ) remains the same. However, the velocity will have different state depending upon the depth of hump. If the height of hump is  $\Delta z$ , the total energy is

constant since head loss  $h_f$  is zero; the specific energy ( $\frac{V^2}{2g} + y_2$ ) will go up to

balance the loss of potential energy  $\Delta z$  and the flow will experience an increase in velocity with the hump. Therefore, point 2 on curves 2 represents the state of flow at the hump crest at section (4)-(4). The flow will remain subcritical until the hump height is too large. When the hump is too large, the critical flow can occur

at the crest of the hump and supercritical flow can follow downstream. Otherwise, the flow is subcritical and it is accelerated along the path (1)-(1) to (4)-(4) if

$\frac{V_2^2}{2g} > \frac{V_1^2}{2g}$  (Fig. 4.1). If  $\frac{V_2^2}{2g} < \frac{V_1^2}{2g}$ , the flow along the upward hump is under

deceleration and along the down slope of the hump additional deceleration occurs and merges to down stream flow condition. So hump helps to gain a lower pressure gradient is more desirable in the transition to diminish flow separation.

#### 4.2 Velocity coefficient:

The familiar Bernoulli equation for energy is written in terms of head between two points along the streamlines as follows:

$$y_1 + z_1 + \frac{v_1^2}{2g} = y_2 + z_2 + \frac{v_2^2}{2g} \quad (4.1)$$

In the above equation, it is assumed that the velocity is constant across the whole section of the flow. This is never true because viscous effects make the velocity lower near the solid boundaries than at a distance from them. If the velocity does vary across the section, the true mean velocity head across the section

$\left(\frac{v^2}{2g}\right)_m$  will not necessarily be equal to  $\frac{v_m^2}{2g}$  (where  $v_m$  = mean velocity). Hence,

the use of the mean velocity in the velocity head term necessitates a kinetic energy flux correction defined by (Sturm, T. W, 2001)

$$\alpha = \frac{\int v^3 dA}{v_m^3 A} \quad (4.2)$$

The same consideration applies to the calculation of the momentum term  $(Q\rho v)_m$

and requires a momentum correction coefficient  $\beta$  which is equal to

$$\beta = \frac{\int v^2 dA}{v_m^2 A} \quad (4.3)$$

The coefficients  $\alpha$  and  $\beta$  are both unity in the case of a uniform velocity distribution and for any other variation  $\alpha > \beta > 1.0$ . The higher the non-uniformity of velocity distribution, the greater will be the values of the coefficient. Generally, one can assume of  $\alpha = \beta = 1.0$  when the channels are straight, prismatic and uniform (Subramanya, K. 1982). Velocities at different subsection were obtained by Laser Doppler Anemometer. A specimen calculation is provided in the Appendix-B, Table B.1 for  $\alpha$  and  $\beta$  coefficients.

### 4.3 Energy efficiency in diverging flows:

Efficiency in diverging flows is defined in different ways by different researchers. Some of those views are provided below:

#### 4.3.1 General approach

It is defined as the ratio of kinetic energy at the exit to the energy in the inlet (Chaturvedi, 1963 & Kalinske 1946). This approach is adopted when kinetic energy is of prime concern. But it is difficult to calculate kinetic energy at the exit due to flow separation in the transition.

#### 4.3.2 Diffuser effectiveness:

Wintermizt and Ramsay (1957) described the efficiency in terms of diffuser effectiveness as they were involved in the study of flow separation in diffuser. They opined that no single diffuser efficiency is a complete criterion for diffuser performance. They found diffuser performance as a function of a set of parameters as given below:

$$\zeta_D = \phi(C_p, \alpha_1, \alpha_4, A) \quad (4.4)$$

Here,  $\zeta_D$  = Diffuser Effectiveness

$$C_p = \frac{2\Delta P}{\rho \bar{U}_0^2} \quad (4.5)$$

$\alpha_1$  and  $\alpha_4$  = energy co-efficients at entrance and exit

and A= area ratio

They also mentioned that  $C_p$ ,  $\alpha_1$  and  $\alpha_4$  are again depend on diffuser angle, surface texture and inlet conditions.

The present study defines efficiency as the ratio of kinetic energy at the exit to that at the entrance. This is a simplified and realistic approach in calculating efficiency in the transition where flow separation is a major concern.

#### 4.3.3 Turbulence intensity and turbulent kinetic energy

The Kolmogorov scales give a measure of the length, velocity and time scales for the smallest eddies in turbulent flow. Another important variable used to study turbulent flow is turbulence intensity (I) and is defined as

$$I = \frac{\overline{u'}}{U} \quad (4.6)$$

Here,  $\overline{u'}$  = the root-mean-square of the turbulent velocity fluctuations, and U= mean velocity.

Again, the average turbulent kinetic energy (TKE) per unit mass is proportional to the sum of the squares of the intensities.

$$\text{Therefore, (TKE) } k = \frac{1}{2} (\overline{u_x'^2} + \overline{u_y'^2} + \overline{u_z'^2}) \quad (4.7)$$

$$\overline{u'} = \sqrt{\frac{1}{3} (\overline{u_x'^2} + \overline{u_y'^2} + \overline{u_z'^2})} = \sqrt{\frac{2}{3} k} \quad (4.8)$$

In the above equation it is assumed that specific relative turbulence intensities are more or less isotropic (Wilcox (2006) i.e.,

$$\overline{u_x'^2} = \overline{u_y'^2} = \overline{u_z'^2} \quad (4.9)$$

#### 4.3.4 Boundary shear stress distribution

Measuring boundary shear stress distribution is very important in hydraulic engineering problems like scour, bed and bank protection, sediment transport and the design of hydraulic structures in channel transition. Applying an average value of bed shear stress criteria is not practical in sediment transport. It may lead to either underestimate or over estimate local values of shear. Hence, there may be either no transport or high transport of sediment because of local shear. Earlier investigators emphasized to determine local shear stress to overcome this problem. There are various methods to determine boundary shear stress. Here, three methods will be employed to compare the results with each other.

Chow (1959) used the average shear formula at the channel bottom.

$$\tau = \gamma RS \quad (4.10)$$

Here,  $\tau$ = boundary shear stress,  $\gamma$ = Unit weight of water,  $R$ = hydraulic radius,  $S$  =slope of the energy gradient line.

However, the boundary shear stress is not uniformly distributed along the wetted perimeter except for uniform wide open channel and closed pipe flow. Hence, it is necessary to determine local boundary shear stress in open channel. Boundary shear stresses are generally small in magnitude and accurate measurements are difficult. The shear within the boundary layer thickness can be calculated using the formula, (Schlichting, 2000),

$$\tau = \mu \frac{du}{dy} \quad (4.11)$$

here,  $\tau$ =shear stress,  $\mu$ =molecular viscosity,  $du$ =velocity and  $dy$ = distance of the point from the bed.

Later on some researcher used the logarithmic law outside viscous sub-layer to calculate shear velocity, and from shear velocity relation, shear stress was calculated.

The logarithmic equation can be written, regardless of smooth, transitional or rough bed, in the form, (Hollingshead, 1972)

$$\sqrt{\frac{\tau}{\rho}} = u_{\tau} = \frac{1}{A} \frac{u_2 - u_1}{\log \frac{y_2}{y_1}} \quad (4.12)$$

Here,  $u_1$ ,  $u_2$  are time averaged velocity measured at  $y_1$  and  $y_2$  distances from the bed,  $A = 5.75$  constant. Shear velocity  $u_{\tau}$  is obtained by solving the right hand side of the above equation. Hence, shear stress  $\tau$  is obtained equating the LHS with RHS of equation (4.12).

#### 4.3.5 The Reynolds number

The Reynolds number is described as the ratio of the inertial force to the viscous force in the pipe or channel. The Reynolds numbers are determined by (Chow, 1959),

$$Re = \frac{UR}{\nu} \quad (6.13)$$

Here,  $U$  is the average velocity at section  $x = 0.0$  m (Entry) in the transition channel,  $R$  is the hydraulic radius defined by the cross-sectional area  $A$  divided by wetted perimeter  $P$  i.e.,  $R = \frac{A}{P}$ , and  $\nu$  is the kinematic viscosity ( $\nu = \frac{\mu}{\rho}$ ).

#### 4.3.6 Froude number

The Froude number is defined as the ratio of the inertial force to the gravity force in the flow. It is determined as the ratio between mean flow velocity,  $V$ , and the speed of a small gravity (surface) wave travelling over the water surface (Hwang, 1996).

Therefore, Froude number is

$$F_r = \frac{V}{\sqrt{gD}} \quad (6.14)$$

Here,  $g$  is the acceleration due to gravity and  $D$  is the hydraulic depth.

When  $F_r = 1$ , the flow is in the critical state, when  $F_r < 1$ , the flow is subcritical and when  $F_r > 1$ , the flow is supercritical.

## CHAPTER 5

### 5.0 3D NUMERICAL CFD SIMULATIONS

#### 5.1 CFD modeling

The three most powerful tools of fluid dynamics are experiments, partial differential equations (PDEs), and dimensional analysis. Earlier fluid flow investigations were largely experimental and only very simple fluid flow could be numerically solved. With recent advances in computing techniques and numerical solution methodologies, CFD (Computational Fluid Dynamics) has now been widely used in various industry applications. Despite its wide application, CFD has recently been used in river flow research and modeling hydrology and morphology by Nezu and Nakagawa, 1993; Lane, 1998; Maetal., 2002; Cao et al., 2003, etc. (Ingham, D. B. et al., 2005). CFD can be an alternative to physical modeling in many areas including open channel flow, river morphology, flow structures and sediment transport and can be used in river management and flood prediction with its advantage of lower cost, time and flexibility.

#### 5.2 Computational fluid dynamics (CFD)

Computational fluid dynamics (CFD) is the science (and art) of predicting fluid flow, heat transfer, mass transfer, chemical reactions and other related phenomena by solving mathematical equations that represent physical laws, using a numerical process. CFD is an equal partner with pure theory and pure experiment in the analysis and solution of fluid dynamics problems. The physical aspects of any fluid flow are governed by the following three fundamental principles:

- Mass is of a fluid conserved



- The rate of change of momentum equals the sum of the forces on a fluid particle (Newton's second law)
- The rate of change of energy is equal to the sum of the rate of heat addition to and the rate of work done on a fluid particle (first law of thermodynamics).

These physical principles can be expressed in terms of mathematical equations, which are either integral or partial differential equations. Computational fluid dynamics is the art of replacing the governing integral equations or partial differential equations of fluid flow with numbers, and advancing these numbers in space and/or time to obtain a final numerical description of the complete flow field of interest. The end product of CFD is indeed a collection of numbers in contrast to a closed form of analytical solution. The objective of most engineering analysis is a quantitative description of the problem, i.e., numbers. Computers have been used to solve fluid problems for many years. Initially CFD was a tool used exclusively in research and now-a-days increasingly it is becoming a vital component in the design of industrial products and process due to recent advances in computing power, together with 3D graphics, numerical algorithm, and availability of cheap and robust commercial solvers.

Therefore, CFD is now an established industrial design tools. Despite advances in other branch of engineering, hydraulic engineering lags behind in using CFD. But CFD can be very demanding field in modeling river flow phenomena because of the complexity of the irregular bank and bed topographies as well as enormous volume involved in natural river system.(Ingham, et al., 2005). However, the current concerns of issues to be addressed in CFD simulations are grid resolution, grid dependence, wall roughness and appropriate turbulence models (Hardy et al., 1999). Nevertheless, CFD simulations have the capability to provide the better understanding the flow

characteristics of open channel flow and design inputs to control flow separation in transitional flow.

### **5.3 Organization of CFD Codes**

Most of the commercial CFD codes include user interfaces to input problem parameters and examine the output. Hence all codes essentially contain three main elements viz., a pre-processor, a solver and a post-processor. The pre-processor defines the geometry of the region of interest, generates grid/mesh, defines fluid properties and specifies the boundary conditions. The solver sets up the numerical model, approximates the unknown flow variables, discretizes the governing equations, solves the algebraic equations, computes and monitors the solution. There are three main streams of numerical solution techniques: finite difference, finite volume and finite element. The main difference among the three separate streams is associated with the way in which the flow variables are approximated and with the discretization processes. Among the three finite volume methods, finite volume method is the most well-established and thoroughly validated general purpose CFD technique. All five main commercially available CFD Codes viz., ANSYS CFX, FLUENT, FLOW3D, PHOENICS and STAR-CD are using the finite volume method. The post-processor examines and displays the result with data visualization tools and considers revisions of the model, if necessary. At the end of a simulation the user must make judgment whether the results are “good enough”. It is not easy to assess the validity of the models of physics embedded in a program as complex as a CFD codes or the accuracy of its final results unless making comparison with experimental investigations. One should bear in mind that CFD is no substitute for experimentation, but a very powerful supplementary problem solving tool. In this study in addition to main laboratory investigation, a few CFD analyses were done using the commercial

software ANSYS CFX to compare the laboratory investigation and in other words, to validate the CFD simulation by laboratory experiment.

#### 5.4.0 Basic governing equations

##### 5.4.1 Navier-Stokes equation

The pressure and the velocity of the flow are the two basic parameters to describe an open channel flow. Since water is assumed to be incompressible Newtonian fluid, these parameters are governed by the classical Navier-Stokes equations. These equations were developed on the basis of physical laws of conservation of mass and momentum. The Reynolds-average form of 3D Navier-Stokes equations in the Cartesian co-ordinate for an incompressible and turbulent fluid flows are given below (Hinze, 1975):

Navier\_Stokes equation

$$\rho \frac{\partial u^i}{\partial t} + \rho u^j \frac{\partial u^i}{\partial x^j} = -\frac{\partial p}{\partial x^i} + \frac{\partial}{\partial x^j} \left[ \mu \left( \frac{\partial u^i}{\partial x^j} + \frac{\partial u^j}{\partial x^i} \right) \right] + \frac{\partial \tau^{ij}}{\partial x^j} + \rho g^i \quad (5.1)$$

Continuity Equation

$$\frac{\partial u^i}{\partial x^i} = 0 \quad (5.2)$$

Here,

$x^i$  = components of the Cartesian co-ordinate system ( $i=1, 2, 3$ );  $t$  = time;  $u^i$  = mean fluid velocity;  $p$  = pressure;  $\rho$  = density;  $\mu$  = molecular viscosity; and  $g^i$  = gravitational acceleration.

Open channel flow can be modeled numerically by using the above Reynolds-averaged Navier-Stokes (RANS) equations. The classical model uses the Reynolds equations which forms the basis of turbulence calculations in currently available commercial CFD codes. The most common turbulence models are as follows:

Classical Models based on (time-averaged) Reynolds equations

1. Zero equation model-mixing length model
2. Two-equation model  $k - \varepsilon$  **and**  $k - \omega$  mode
3. Reynolds stress equation model
4. Algebraic stress model

Large Eddy simulation based on space-filtered equations

Of the classical models the mixing length and two-equation  $k - \varepsilon$  **and**  $k - \omega$  models are the most popularly used and validated models.

#### 5.4.2 Two-equation model $k - \varepsilon$ **and** $k - \omega$

Despite recent sophisticated models like the RSM (Launder et al., 1975), the two equation models are still popular turbulence models because of their easy implementation, economy in computation and accuracy in solution with the available computer power. The Standard  $k - \varepsilon$  model (Launder and Spalding (1972) has enjoyed popularity among the turbulence modelers. It represents the eddy viscosity by turbulent kinetic energy  $k$  and dissipation rate  $\omega$  as follows:

$$\mu_t = c_\mu \rho \frac{k^2}{\varepsilon} \quad (5.3)$$

Here,  $c_\mu = 0.09$ , an empirical constant

The turbulent kinetic energy  $k$  and the dissipation rate  $\omega$  have to be obtained by solving the following equations,

Kinetic energy equation

$$\rho \frac{\partial k}{\partial t} + \rho u^j \frac{\partial k}{\partial x^j} = \frac{\partial}{\partial x^i} \left[ \left( \frac{\mu + \mu_t}{\sigma_k} \right) \frac{\partial k}{\partial x^i} \right] + P - \rho \varepsilon \quad (5.4)$$

Here,

$$P = (\mu + \mu_t) \left( \frac{\partial u^i}{\partial x^j} + \frac{\partial u^j}{\partial x^i} \right) \frac{\partial u^i}{\partial x^j} \quad (5.5)$$

and it represents the production of turbulence.

Dissipation rate equation

$$\rho \frac{\partial \varepsilon}{\partial t} + \rho u^j \frac{\partial \varepsilon}{\partial x^j} = \frac{\partial}{\partial x^i} \left[ \left( \frac{\mu + \mu_t}{\sigma_\varepsilon} \right) \frac{\partial \varepsilon}{\partial x^i} \right] + c_{\varepsilon 1} \frac{\varepsilon}{k} P - c_{\varepsilon 2} \frac{\varepsilon}{k} \rho \varepsilon \quad (5.6)$$

Here,  $c_{\varepsilon 1} = 1.44$ ,  $c_{\varepsilon 2} = 1.92$ ,  $\sigma_k = 1.0$ ,  $\sigma_\varepsilon = 1.3$

Similar to  $k-\varepsilon$  model, the  $k-\omega$  models are derived for the turbulence kinetic energy

$k$  and the specific dissipation rate  $\omega = \frac{\varepsilon}{k}$  and the turbulent viscosity is calculated by,

$$\mu_t = \alpha \rho \frac{k}{\omega} \quad (5.7)$$

The first  $k-\omega$  model was proposed by Kolmogorov (1942). However, the models of Wilcox (1988, 1998) and Mentor (1994) were used and tested extensively.

### 5.4.3 Boundary conditions

The two equations  $k-\varepsilon$  model is elliptical in nature and it requires boundary conditions on all the boundaries of the solution domains to solve the equations. The boundary conditions to be used should reflect the real conditions to achieve the accuracy of the model. For channel flow the following boundary conditions are required:

- (i) Inlet boundaries
- (ii) Outlet boundaries
- (iii) Free surface boundaries
- (iv) Wall functions

#### 5.4.4 Inlet boundaries

Fluid velocity and turbulence quantities are specified at the inlet boundary. A uniform boundary profile is chosen when the inlet boundary is located sufficiently upstream of the sections under investigation to get a fully developed flow. Great care should be taken to select a development length since this may be large in some cases.

#### 5.4.5 Outlet boundaries

The down stream boundary is also taken on a location where the velocity is fully developed and the gradient is zero. When flow can not be treated as fully developed, the pressure condition may be used and the outlet pressure is set to zero. To find the surface profile, the outlet boundary condition needs the water surface level to be specified.

#### 5.4.6 Free surface boundaries

In open channel simulation, the free surface boundary is very important. For steady state flow condition with horizontal free surface, a fixed lid method is used to represent water surface. Various methods are employed to find the free surface. These are classified into two major groups (Ferziger, 2002) viz., (a) Interface-Tracking Scheme and (b) Interface-Capturing Scheme

#### 5.4.7 Interface-tracking scheme

Sharp interface is defined in this method and the model tracks the motion of the free surface in the computation. Frequent grid adjustments are required for unsteady free surface. Very small time steps and boundary-fitted grids are used in this method to find sharp interface

The boundary for the vertical velocity is determined by following equation:

$$u_z = \frac{\partial H}{\partial t} + u_x \frac{\partial H}{\partial x} + u_y \frac{\partial H}{\partial y} \quad (5.8)$$

Here,  $u_x$ ,  $u_y$ , and  $u_z$  are the flow velocity in x-direction, y-direction, and z-direction respectively.  $H$  is the water depth and  $t$  is the time.

The pressure variable  $p$  is determined by the following equation:

$$p = p_0 + \gamma H \quad (5.9)$$

Here,  $p_0$  is the free surface pressure, and  $\gamma$  is the specific gravity (Meselhe and Sotiropoulos, Huang et al., 2002).

#### 5.4.8 Interface-capturing scheme

The Volume of Fluid (VOF) method is one of the Interface-capturing methods, which does not specify any sharp boundary (Hirt and Nicholas, 1981). Though it was designed for solving unsteady fluid problem, it is also used to predict a steady flow while water level is not known. The VOF method can be used to determine the surface profile using control volume method. In this method, a water volume fraction,  $F$ , can be defined by,

$$F = \frac{\delta\Omega_{water}}{\delta\Omega_{cell}} \quad (5.10)$$

Here,  $\delta\Omega_{cell}$  is the volume of the computational cell and  $\delta\Omega_{water}$  is the fraction of the volume of the cell filled with water. Thus, the VOF equation is

$F = 1$ , when cell is full of water

$F = 0$ , when cell is full of air

$0 < F < 1$ , when cell contains free surface.

#### 5.4.9 Wall functions

Fluid flow near to the channel wall (bed and bank) is generally very complex in respect of both its mean and turbulent structure. A very fine grid near to these boundaries is required to simulate their effect on the fluid flow. Launder and Spalding

(1974) proposed the standard wall function to find the characteristics of mean fluid flow region and to avoid the use of expensive and complex fine grid in the vicinity of the wall boundaries. The standard wall function, which relates the local shear stress (through  $u_\tau$ ) to the mean velocity, turbulence kinetic energy and rate of dissipation, can be expressed as follows:

$$\frac{u}{u_\tau} = \frac{1}{\kappa} \ln \frac{u_\tau y}{\nu} + C \quad (5.11)$$

Here,  $u$  is the velocity parallel to the wall at the first cell,  $u_\tau$  is the friction velocity,  $\kappa = 0.41$ ,  $y$  = distance normal to the wall,  $\nu$  is the kinematic viscosity and  $C = 5.0$  for smooth walls. The effect of roughness has to be considered for rough surface and the value of constant  $C$  has to be adjusted accordingly.

#### 5.4.10 Grid generation

Grid generation is one of the difficult tasks to solve partial differential equations on a complex domain such as the geometry of an  $u_\tau$  open channel transition. Boundary-fitted orthogonal grids and curvilinear coordinates are generally employed to simulate flows in complex geometries. These are classified as structured, block-structured, or unstructured. In this study multi-block structured grid method is used. This method divide the geometry in to several blocks and each block is again meshed by power law function. It creates fine mesh near the channel transition or near the walls or in the unsteady flow region.



## CHAPTER 6

### 6.0 DISCUSSION OF RESULTS

#### 6.1.0 Experimental results

Velocity measurements were carried out in the open channel transition with the 66% expansion. The upstream flow conditions were subcritical and the Froude number range was from 0.17 to 0.41. The variation of flow rate was from 0.0070 m<sup>3</sup>/s to 0.0168 m<sup>3</sup>/s. The Reynolds number  $R_e$  varied from 27,000 to 109,000 representing the turbulent flow regime. The channel transition can trigger flow separation causing energy losses. To reduce the effect of separation, the use of a hump (rising of bed level) or vanes were explored by measuring the velocity profiles and turbulence intensities in the section downstream of the transition. Moreover, the primary parameters like Reynolds numbers were varied and the study determined the velocity coefficient  $\alpha$  and the momentum coefficient  $\beta$ , turbulent energy and the regions of reverse flow were investigated. The data obtained from LDA measurements of the velocity were analyzed and velocity profiles were drawn.

Fig.6.1 shows the velocity contours for axial velocities at the entry section at  $x = 0.0$  m, near the exit section at  $x = 0.325$  m and a section in the channel slightly downstream of the channel transition at  $x = 0.650$  m for a specific flow condition ( $Q = 0.0070$  m<sup>3</sup>/s). Figs. 6.2 to 6.15 provide the velocity contours and the velocity distribution near the bed and free surface for several other flow conditions ( $0.0070 < Q < 0.0168$ ). Figs. 6.16 to 6.24 represent the turbulent kinetic energy; Figs. 6.25 to 6.33 depict the turbulent intensities.

Table 6.1 Flow characteristics of laboratory experiments

Measurement locations  $X_1 = 0.0$  m (Entry) and  $X_2 = 0.325$  m (Exit)

Discharge $Q$ ( $\text{m}^3/\text{s}$ )	Velocity $v$ (m/s)	Channel Depth $D$ (m)	Froude No $F_r$	Reynolds No $R_e$
$X_1 = 0.0133$	0.492	0.158	0.395	86,575
$X_2 = 0.0133$	0.273	0.171	0.211	52,042
$X_1 = 0.0168$	0.551	0.178	0.417	109,275
$X_2 = 0.0168$	0.325	0.182	0.243	65,795
$X_1 = 0.0160$	0.592	0.158	0.475	104,150
$X_2 = 0.0160$	0.327	0.172	0.251	62,563
$X_1 = 0.0158$	0.541	0.171	0.416	102,714
$X_2 = 0.0158$	0.285	0.195	0.206	61,819
$X_1 = 0.0070$	0.282	0.145	0.236	45,484
$X_2 = 0.0070$	0.161	0.153	0.130	27,230
$X_1 = 0.0110$	0.227	0.170	0.175	42,925
$X_2 = 0.0110$	0.389	0.165	0.306	71,543
$X_1 = 0.0142$	0.488	0.170	0.378	92,375
$X_2 = 0.0142$	0.271	0.185	0.201	55,562
$X_1 = 0.0072$	0.284	0.148	0.236	46,836
$X_2 = 0.0072$	0.273	0.154	0.222	46,834

### 6.1.1 Reynolds number effect

Froude number is a primary parameter of subcritical open channel flow. However, its influence was restricted due to its narrow range of variation (Table 6.1) in the tests. Moreover, since the experimental channel flow is highly turbulent in nature, the Reynolds number here plays a role to characterize the dynamics of flow separation including the distribution of velocity, turbulent kinetic energy and turbulent intensity. Experimental evidence shows that the point of separation around a sphere or rounded bluff body can be moved downstream when the boundary layer flow becomes turbulent. When turbulence is increased by mechanical devices like tripping rings, the channel flows turn more turbulent giving the desired movement of separation point

(Schlichting, 2000). However, for flow past a channel expansion of the present case separation point is fixed and hence effect of Reynolds number is not extensive. Still the extent of separation depends on the factors such as the divergence angle, and the shape of the transition. It may be a straight transition or a curved transition. Flow visualization by dye techniques can give the downstream point of reattachment in some cases. As the dye diffused in the flow very quickly, the procedure of dye technique to locate point of separation was not successful. One can use a tuft to locate the reattachment point.

### **6.1.2 The energy coefficient $\alpha$ and momentum coefficient $\beta$**

Table 6.2 shows the variations of  $\alpha$  and  $\beta$ . In each case, the flow separation zone is seen at section 4-4. The values of  $\alpha$  and  $\beta$  are larger at section 4-4, but those are much smaller at sections 1-1 and 5-5 as expected. In the later case, the flow has recovered slightly.

Table 6.2 Variation of  $\alpha$  and  $\beta$  with Reynolds Number

Sl. No	Discharge Q (m <sup>3</sup> /s)	Inlet R <sub>e</sub> No	Inlet F <sub>r</sub> No	Values of $\alpha$			Values of $\beta$			Comments
				Section	Section	Section	Section	Section	Section	
				1-1	4-4	5-5	1-1	4-4	5-5	
				$\alpha$	$\alpha$	$\alpha$	$\beta$	$\beta$	$\beta$	
1	0.0110	71543	0.31	1.00	1.10	1.05	1.00	1.03	1.01	No Hump
2	0.0133	86575	0.40	1.07	N/A	N/A	1.02			No Hump
3	0.0070	45484	0.24	1.01	1.31	1.18	1.00	1.11	1.06	No Hump
4	0.0142	92375	0.38	1.08	1.23	1.18	1.03	1.07	1.06	No Hump
5	0.0158	102714	0.42		1.44	1.28		1.15	1.11	No Hump
6	0.0070	46836	0.24		1.23	1.23		1.10	1.08	12.5 mm Hump
7	0.0168	109275	0.42	1.01	1.27	1.15	1.00	1.10	1.04	12.5 mm Hump
8	0.0070	46836	0.24		1.16	1.27		1.06	1.11	25 mm Hump
9	0.0158	102714	0.42		1.32	1.09		1.13	1.03	25 mm Hump
10	0.0142	92375	0.38	1.08	1.42	1.11	1.03	1.16	1.04	1 Vane
11	0.0070	46836	0.24		1.30	1.15		1.11	1.05	1 Vane
12	0.0142	92375	0.38	1.08	1.21	1.01	1.03	1.08	1.00	3 Vanes
13	0.0070	46836	0.24	1.08	1.31	1.09	1.03	1.11	1.03	3 Vanes

### 6.1.3 Velocity distribution and percentage area of reversal flow

The present study investigated the effectiveness of the hump and vane to reduce flow separation at the channel expansion under subcritical flow regime. Efforts were made to quantify the reverse flow region due to flow separation to some extent for different flow conditions considering the rate of flow, with and without auxiliary devices (humps and vanes). The results given in the Table 6.3 show the level and extent of the reverse flow observed at the exit of the transition ( $x = 0.325$  m) for different flow rates considering other variables.

Table 6.3 Variation of % of area of reverse flow field with inlet Reynolds number

Sl. No.	Discharge Q in m <sup>3</sup> /s	Inlet Reynolds No. $R_e \times 10^{-4}$	Area of Flow At Section 4-4 m <sup>2</sup>	Area of Reverse Flow Field at Sec.( 4-4) m <sup>2</sup>	% of Reverse Flow	Remarks
1	0.0070	4.54	0.04345	0.0060	14	Fig.6.1(b), No Hump
2	0.0142	9.23	0.05310	0.0040	8	Fig.6.3(b), No Hump
3	0.0158	10.27	0.05339	0.0015	3	Fig.6.4(a), No Hump
4	0.0070	4.68	0.04061	0.00006	0.1	Fig.6.5(b), 12.5 mm Hump
5	0.0168	10.41	0.00000	0	0	Fig.6.6(b), 12.5 mm Hump
6	0.0070	4.68	0.03777	0	0	Fig.6.7(b), 25 mm Hump
7	0.0158	10.27	0.04970	0	0	Fig.6.8(b), 25 mm Hump
8	0.0072	4.68	0.04430	0.0003	1	Fig.6.9(b), 1 Vane
9	0.0142	9.23	0.05254	0.0008	1	Fig.6.10(b), 1 Vane
10	0.0072	4.68	0.04430	0	0	Fig.6.11(b), 3 Vanes
11	0.0142	4.68	0.05026	0	0	Fig.6.12(b), 3 vanes

Figs. 6.2a to 6.4c denote the flow behavior in the transition for three different flow rates ( $Q = 0.0133 \text{ m}^3/\text{s}$ ,  $Q = 0.0142 \text{ m}^3/\text{s}$ , and  $Q = 0.0158 \text{ m}^3/\text{s}$ ).

In all these cases, neither the hump nor the vane was present. Reverse flows were concentrated at the corners at section 4-4. It may be recalled that above figures show no reverse flow at the entry section and at the section down stream of the transition. The variations of velocity near the free surface (top) and near the floor (bottom) are also included in Fig.6.5 for two different flow rates. Figures 6.5a and 6.5b show the velocity distribution near the bottom and near the surface of water and the negative values indicate the reversal of flow.

#### **6.1.4 Transition flow characteristics with a hump**

Fig. 6.6 shows the characteristics of velocity for transition flow with a hump in place. It shows that even a small hump (12.5 mm hump) reduces the flow separation significantly (Fig6.6b). Fig. 6.7 shows the flow behavior for the same hump height of 12.5 mm at  $Q = 0.0160 \text{ m}^3/\text{s}$ . and Figs. 6.8(b) and 6.9(b) show that a larger hump height ( $z = 25 \text{ mm}$ ) removes the separation totally. As before the velocity distribution near the bottom surface and near the surface of water are shown in Figs. 6.10a to 6.11b. The disappearance of negative values indicates that the flow separation is not present.

#### **6.1.5 Effect of Vane on Transition Flow Characteristics**

Figs. 6.12 and 6.13 show the effect of a single vane, and Figs.6.14 and 6.15 show the effect of 3 vanes in the transition. A single vane reduced the flow reversal to 1% from

that of flow without vane a (14%). Further, it was found that the three vanes were more effective than the single vane. One vane reduced separation significantly but 3 vanes completely removed separation. The study revealed that the percentage of reversal flow is much less than that in a smaller expansion as found in the past preliminary studies.(Rao, 1967 and Ramamurthy et al. 1967). In the past studies of Rao (1967), the end of channel boundary conditions were different and the velocity data was collected by Pitot tubes which are not very effective for reverse flow measurement. In the present case, LDA was used to measure velocity. The most striking feature of the velocity distribution is that though the channel section is symmetrical, the flow distribution in the transition is unsymmetrical.

#### **6.1.6 Turbulent Kinetic Energy and Turbulence Intensities**

Figs. 6.16 to 6.18 show the distribution of turbulent kinetic energy for 3 different flow rates when no hump was present. Figs. 6.19 to 6.22 show the kinetic energy data at different sections for transition flows with humps. Lastly, Figs. 6.23 to 6.24 provide kinetic energy data for transition flows with vanes.

Figs.6.16 to 6.24 and Figs. 6.25 to 6.33, represent turbulent kinetic energy (TKE) associated with the open channel transition flow and the turbulence intensity (TI) distributions respectively at the three sections with neither the hump nor the vane and a hump ( $\Delta z=12.5$  or  $25$  mm) and the two systems of vane (1 and 3 vanes). These data refer to both the maximum and minimum flows of  $0.0158$  and  $0.007$  ( $\text{m}^3/\text{s}$ ). Since at the exit section ( $x = 0.325$  m), flow separation was present due to channel expansion, turbulence data was collected there. The intensity of turbulence sketches and the turbulent kinetic energy sketches are nearly similar. As such, only the former are discussed in details in the following section.

### 6.1.7 Turbulence Intensity Diagrams

Fig. 6.25 shows the intensities for minimum flow condition of  $0.007 \text{ (m}^3/\text{s)}$  and without use of hump. Here, the observed intensities were 0 - 0.8 at section 4-4 and 0-0.3 at section 5-5 and maximum intensities were near the walls.

In Fig. 6.26, it was also observed that the turbulent intensities with a range of 0-1.0 are high at section 4-4 (Fig.6.26b) in comparison to other two sections 1-1 and 5-5 with the range of 0-0.35 and 0-0.8 respectively. The turbulent kinetic energy and intensities were highest at surfaces in section 4-4 and 5-5 and at sides in section 1-1. The middle area experienced the lowest intensities. Mehta (1981) and later El-Shewey and Joshi (1996) conducted the study of the effect of channel expansion on turbulence characteristics. In Figs. 6.26b and 6.26c, the maximum turbulence intensities occurred either close to free surface or close to bottom which agreed with the findings of Brundette and Baines (1985) and El-Shewey and Joshi(1996). They state that turbulent intensities increase toward the free surface indicating the transfer of a higher-momentum flux from the channel bed to the free flow surface.

Fig. 6.27 represents turbulent intensities data for another case of without hump or vane situation. Here the flow rate was  $0.0158 \text{ (m}^3/\text{s)}$  with higher Reynolds numbers. The turbulent intensity ranges were 0 to 0.6 and 0 to 0.4 at section 4-4 and 5-5 respectively. The highest intensities were clustered near the walls.

The use of 12.5 mm hump reduced the intensity levels to 0-0.30 and 0-0.25 at section 4-4 and 5-5 respectively (Fig.6.28). The percentage reductions were 62% and 16%. The maximum turbulent intensities were close to the walls i.e., the intensity increased with depth.



Fig.6.29 denotes the turbulent intensities at section 4-4 and 5-5 with 12.5 mm hump ( $Q = 0.0168 \text{ m}^3/\text{s}$ ). The intensity ranges were 0-0.25 and 0-0.20 and the high cores were near the walls.

Fig. 6.30 represents a case with 25 mm hump and a flow rate of  $0.0070 \text{ m}^3/\text{s}$ . Here the intensities were in the range of 0-0.20 at exit section and 0-0.15 at the down stream section. The maximum intensities were observed near the walls.

Fig. 6.31 shows two sections at 4-4 and 5-5 with the use of 25 mm hump. Here, the ranges of turbulent intensities were 0-0.2 and 0-0.20. So, the reductions were 67% and 50% respectively. The maximum intensities were observed near the bottoms and corners.

Fig. 6.32 indicates the turbulent intensity distribution for the present study ( $Q=0.142 \text{ m}^3/\text{s}$ ) while using a one splitter vane at the centre. The use of a splitter vane was effective in decrease of turbulent intensities in the range of 0 to 0.3 at section 1-1, 0 to 0.7 at section 4-4 and 5-5. Further at section 1-1, 4-4 and 5-5, the reduction of turbulent intensities was about 14%, 30% and 25% respectively. This trend tells us that the decrease of turbulence intensity indirectly indicates a reduction of flow separation. Here the maximum intensities were shifted to either the side or floor of the channel and the minimum was at the middle.

Fig.6.33 represents the use of 3 vanes placed at equal distance apart and here the intensity decrease trend is similar to that of one vane. The maximum intensities occurred at the sides of the sections.

Intensity distribution patterns also suggest that the flow was anisotropic throughout the depth. Turbulent anisotropy is the primary process triggering secondary flows of Prandtl's second kind (Nezu and Nakagawa 1993).

It was also found that a channel expansion created an unbalanced turbulent kinetic energy distribution, thus affecting the distribution of intensities. This result agrees with the findings of Mehta(1981) and El-Shewey and Josho (1997) who studied flows with sudden expansions. The maximum turbulent intensities were found to occur near the free surface, at the sides and above the bottom. In their studies the intensity increased with depth suggesting that turbulence momentum is not transferred from the core of flow to the bed, but from the bed to the free surface. This indicates the presence of secondary flows of the second kind due to channel expansion (Ead et al. 2000).

Proper use of vane and hump can reduce flow separation and hence reduce intensity of turbulence in down stream of transition. This in turns reduce scour potential due to secondary flow intensity.

#### **6.2.0 Numerical simulation**

A very brief and limited study was also devoted to determine the flow characteristics of transitions based on numerical simulations based on computational fluid dynamics (CFD).

Generally, theoretical analysis and experiments are the main tools to find a solution of open channel problems to meet the needs of field requirements. Recently CFD techniques are being used extensively to solve flow problems. In this study, a few simulations were carried out using the commercial code ANSYS CFX to match the present experimental investigation. Simulation was carried out to predict the velocity distribution, surface profile and turbulence kinetic energy distribution.

### **6.2.1 Turbulence model**

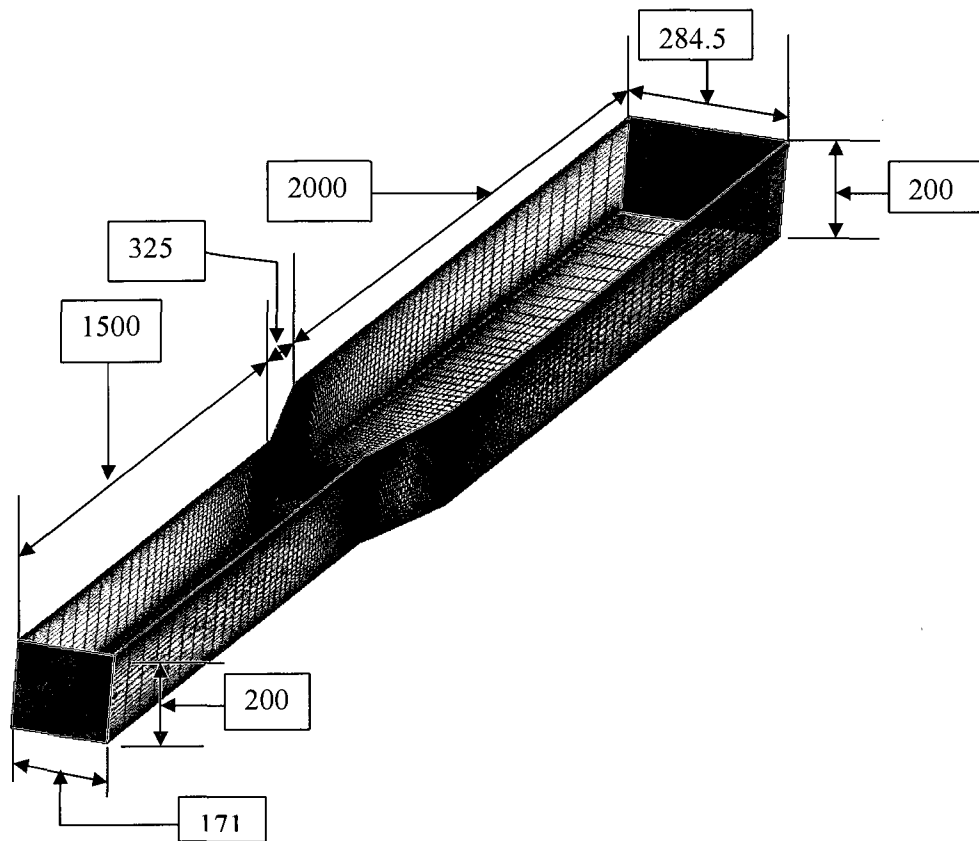
The widely used standard two equation k- $\epsilon$  model was employed to predict the flow characteristics. The control volume method was used to convert the PDE equations to algebraic equations for numerical solutions. The 3-D numerical simulations of the fluid flow were performed with steady water discharge held constant at a value of 0.0133 m<sup>3</sup>/s for cases without a hump, and also for a case with a 25 mm hump. The discharge was also held constant at 0.0142 m<sup>3</sup>/s for 1 and 3 Vane cases. The volume of fraction (VOF) method was used to predict the free water surface elevation. The ANSYS CFX solver was used to perform the calculation.

### **6.2.2 Boundary conditions**

The laboratory set up used smooth Plexiglas rectangular channel. Therefore, at the wall boundary, the standard wall function was used. At the inlet boundary, known flow velocities and turbulent quantities were provided. The outlet boundaries were treated as pressure boundaries with zero pressure input as the general rule for all the air boundaries.

### **6.2.3 Solution procedure**

The computation was done on the geometric domain shown in the figure 6.0.1. The channel was 1.5m long at the upstream section and 2.0 m long at the down stream section.



Dimension in mm

Fig. 6.0.1 Computational Domain for Simulation

The Cartesian co-ordinates were used for flow domain and it was meshed with the power law function ensuring fine mesh near the critical zone like channel expansions and near the corners.

#### 6.2.4 Discussion of results (comparison of model prediction and test data)

#### 6.2.5 Velocity distribution data for the case of no hump

Fig. 6.34 shows the contours of predicted axial velocity  $U$  and those are compared to represent the distribution of velocity contours of experimental data Fig. 6-35; one notices that the pattern is almost similar.

For comparing the results of simulation and test data related to axial velocity, one case is considered with  $Q = 0.0133 \text{ m}^3/\text{s}$ . The simulation (Fig. 6.34) captures the corner separation zones for the case of no hump providing qualitative agreement

between simulation predictions and test data. There is almost separation free flow at the section downstream of the transition exit section 5-5 (flow recovery zone) in the simulation though the test data shows no separation in 5-5.

Figure 6.35 shows also the comparisons between the numerically predicted contours of the axial velocity and those of the experimental data at sections 1-1 (Entry), 4-4 (Exit), and 5-5 (Down stream of exit). Reasonably good qualitative agreement is present between the numerical and experimental data for the axial direction both in terms of the general patterns of the fluid flow and velocity magnitude. It also indicates a reasonable correspondence with respect the zones of separation at the entry, near the exit and the section downstream of the exit. This implies that the standard two equation k- $\epsilon$  model is generally capable of predicting the main structure of hydraulic flow in channel transition.

The shift of the core of high-velocity fluid flow towards the left-hand side of the channel and below the water surface in both the measured and predicted results indicates the asymmetric nature of flow distribution.

#### **6.2.6 Velocity distribution for the case of a single vane splitter**

Fig.6.36 shows the channel section fabricated with Vanes. Fig. 6.37 shows the predicted velocity contours with 1 vane which exhibit similar flow patterns but with some small negative spots near the bottom. Besides this, there is no sharp disagreement.

Fig.6.38 denotes the comparison of experimental velocity contours results with predicted results for single vane and shows a close agreement between them at least qualitatively and indicates the improvement in the flow separation.

### **6.2.7 Velocity distribution for the case of 3-vane splitter**

Fig.6.39 shows the same predicted velocity contours with 3 vanes placed at equal distance apart in the channel. The velocity pattern and magnitude show a good agreement with experimental results (Figure 6.40). Hence, the performance of 3 vanes is better than that of 1 vane both in experiments and simulations.

### **6.2.8 Boundary shear stress**

Boundary shear stress was calculated from measured velocities using standard shear stress equation (Eq. 4.11). These results were compared with the average boundary shear stress determined by equation (Eq. 4.10). Fig. 6.41 shows the plot of these results and both methods gave comparable results.

The standard formula value is quite close to average shear stress value but its peak is higher than the average value and it is located near the centre of the channel width. The comparison of the two methods is shown in Table. 6.4.

Table 6.4 Boundary shear stress in channel transition

Sl. NO.	Distance from Left Wall (m)	Average Shear Stress (N/m <sup>2</sup> ) [ $\tau = \gamma RS$ ]	Boundary Shear Stress (N/m <sup>2</sup> ) [ $\tau = \mu \frac{u}{y}$ ]
1	0.00000	0.000	0.0000
2	0.00500	0.033	-0.0159
3	0.01000	0.033	-0.0086
4	0.01500	0.033	-0.0089
5	0.03550	0.033	-0.0154
6	0.06600	0.033	0.0056
7	0.09649	0.033	0.0305
8	0.12699	0.033	0.0282
9	0.15799	0.033	0.0508
10	0.18799	0.033	0.0479
11	0.21848	0.033	0.0375
12	0.24898	0.033	0.0308
13	0.26948	0.033	0.0221
14	0.27448	0.033	0.0237
15	0.27948	0.033	0.0167
16	0.28448	0.000	0.0000

### 6.2.9 Velocity distribution for the case of 25 mm hump

Fig. A1 indicates the predicted velocity contours at section 1-1, 4-4 and 5-5 for the transition with a 25 mm hump. Using of a hump reduces the adverse pressure gradient and hence decreases flow separation significantly which agrees reasonably well with the experimental results where a 25 mm hump was used in the tests (Fig A2). The experimental results agree qualitatively well with the predicted data for 25 mm hump.

To get further insight into the characteristics of transition flows, simulation studies were slightly extended to note the secondary flow characteristics at the different sections of transition (Appendix-A).

## CHAPTER 7

### 7.0 CONCLUSIONS AND RECOMMENDATIONS

#### 7.1 Conclusions:

The following conclusions are made from the present study:

- (1) The velocity profiles developed from the experimental study show that flow separation occurs in the expansion in the rectangular channel and the velocity profile is not symmetrical. The boundary shear stress is not equal all along the boundary; the bed shear stress is larger near the centre of the channel
- (2) The use of a linear hump is effective to control flow separation in the transition of rectangular open channels. The reversal of flow in the transition is generally eliminated at section section 4-4 near the end of the transition for the configurations tested.
- (3) The use of one splitter vane reduces the separation significantly and the use of three vane system removes separation completely. Humps and vanes are both efficient in reducing flow separation.
- (4) Intensity distribution patterns suggested that the flow in the transition was anisotropic throughout the flow depth. The maximum turbulent intensities are found to occur near the free surface, at the sides and at the bottom.  
  
The turbulent intensity increases with depth and suggests that turbulence momentum is transferred from the bed to the free surface. As such, it indicates the presence of secondary flows of the second kind due to channel expansion.
- (5) The limited qualitative analysis of flow simulation of the present study shows that the CFD model is quite capable of predicting some gross flow



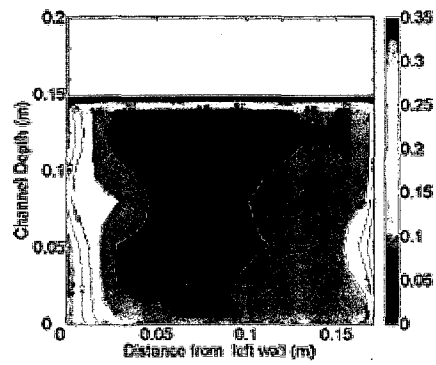
characteristics such as velocity profile, and zone of separation in the open channel transition. The CFD model also shows that using a hump and vane is effective to reduce the flow separation and hence ensure energy efficiency in the transitional flow. The experimental results concur reasonably well with the past experimental studies and as well as with the prediction by present numerical simulation.

## **7.2 Recommendations:**

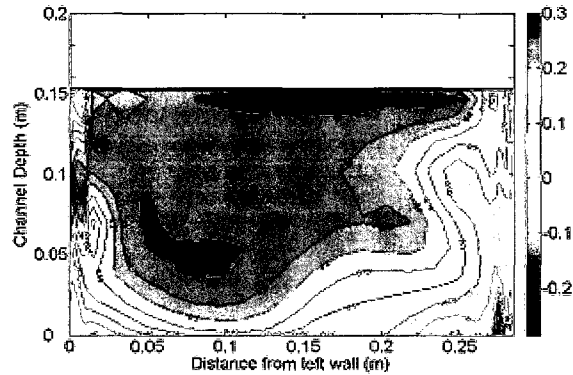
The experimental study can be extended to further investigation in the following areas:

- (1) The effectiveness of hump and vane in other geometric cross sections (trapezoidal channels) can be explored.
- (2) Reduction of turbulence can be investigated by various suppressing devices such as screen, honeycomb etc.
- (3) The height of hump can be increased up to the level of critical flow and investigation can be taken up to find the flow characteristics under conditions close to choking up conditions.
- (4) The effect of nonlinear humps can be explored and the measurement of wall velocity and boundary shear can be completed.
- (5) An advanced, unsteady and more complex turbulence model can be used to predict the flow characteristics in the open channel.
- (6) It is desirable to repeat the test series and simulation for the 25 mm hump to get a better simulation.

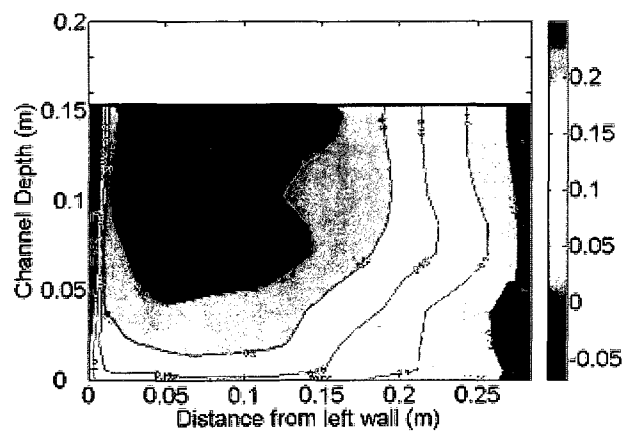
Velocity (m/s)

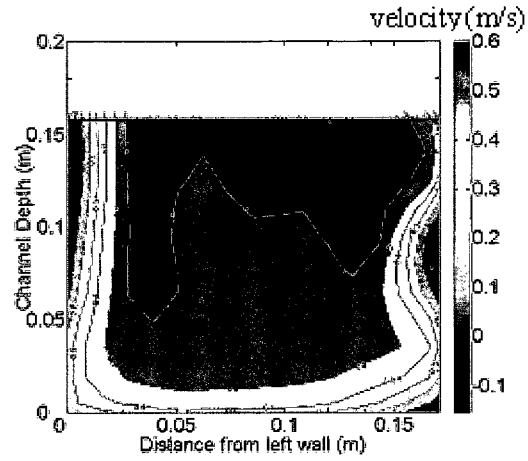
(a) Section at  $x = 0.0$  m (Entry)

Velocity (m/s)

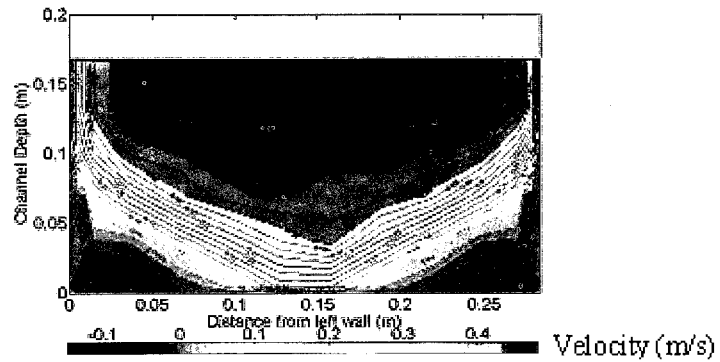
(b) Section at  $x = 0.325$  m (Exit)

Velocity (m/s)

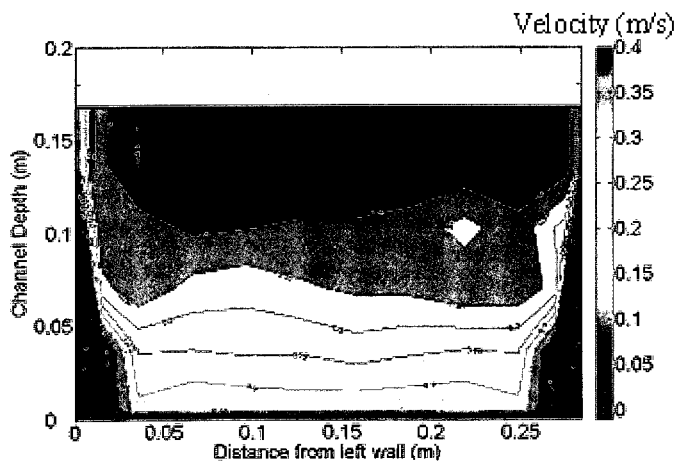
(c) Section at  $x = 0.650$  m (Downstream)Fig. 6.1 Velocity Contours without Hump for  $Q = 0.0070$  m<sup>3</sup>/s



(a) Section at  $x = 0.0$  m (Entry)

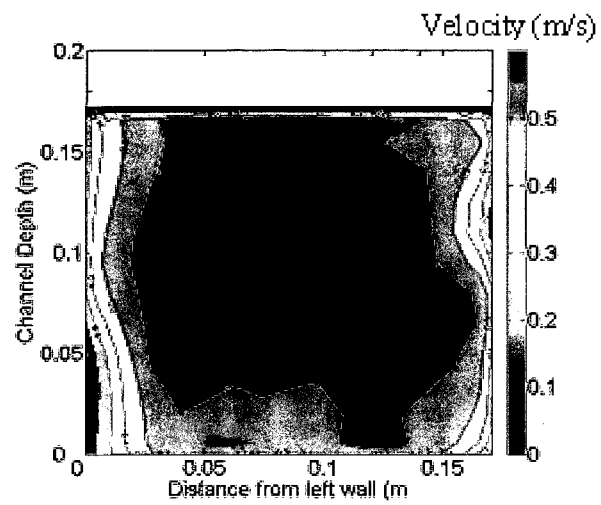
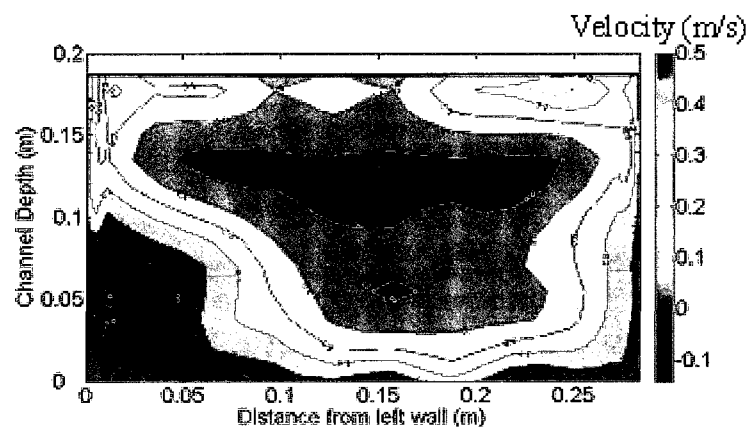
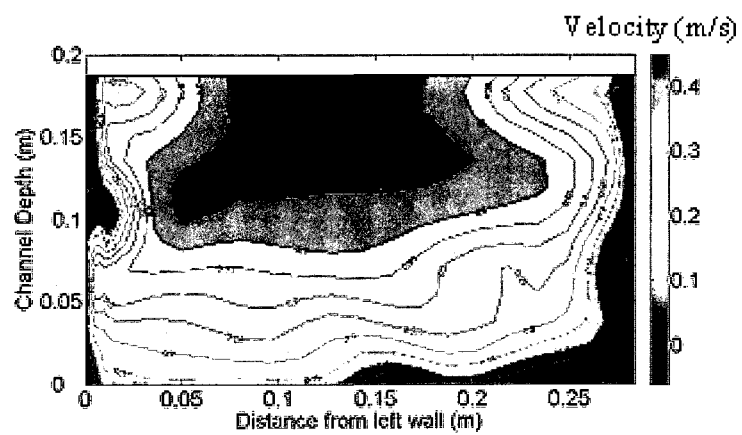


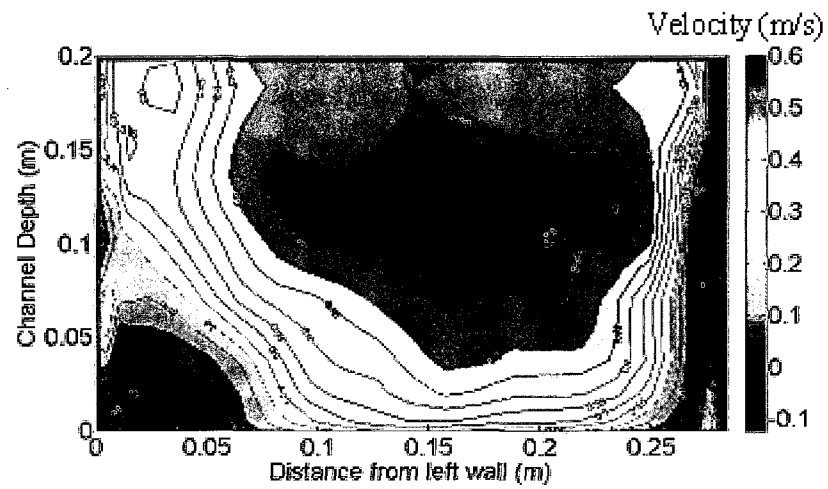
(b) Section at  $x = 0.325$  m (Exit)



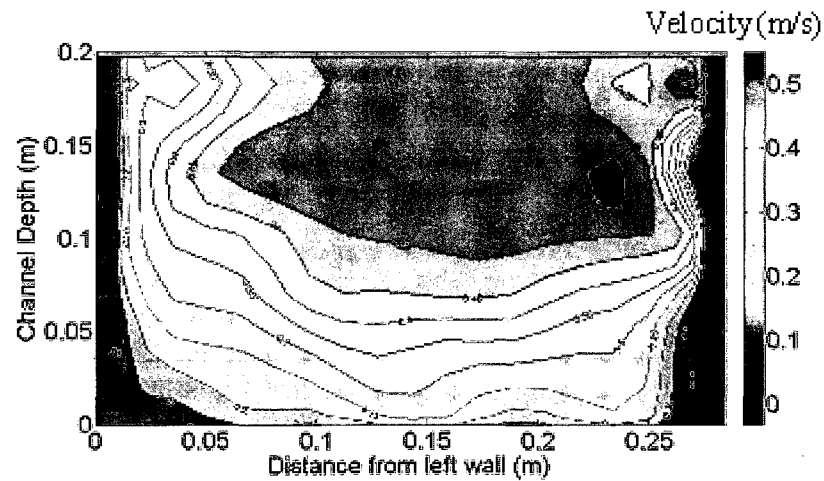
(c) Section at  $x = 0.650$  m (Downstream)

Fig. 6.2 Velocity Contours without Hump for  $Q = 0.0133 \text{ m}^3/\text{s}$

(a) Section at  $x = 0.0$  m (Entry)(b) Section at  $x = 0.325$  m (Exit)(c) Section at  $x = 0.650$  m (Downstream)Fig. 6.3 Velocity Contours without Hump for  $Q = 0.0142 \text{ m}^3/\text{s}$

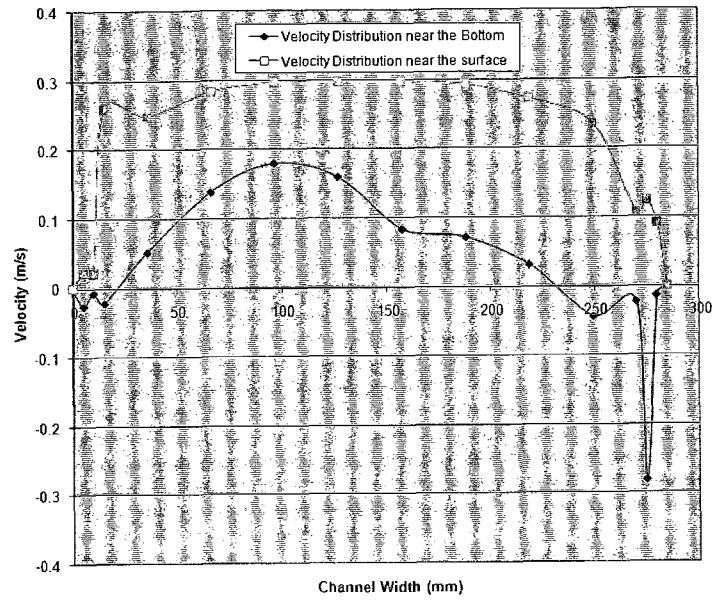


(a) Section at  $x = 0.325$  m (Exit)



(b) Section at  $x = 0.650$  m (Downstream)

Fig. 6.4 Velocity Contours without Hump for  $Q = 0.0158$  m<sup>3</sup>/s



6.5 (a) Velocity Distribution Curves at  $X = 0.325$  m (No Hump),  $Q = 0.0070$  m<sup>3</sup>/s

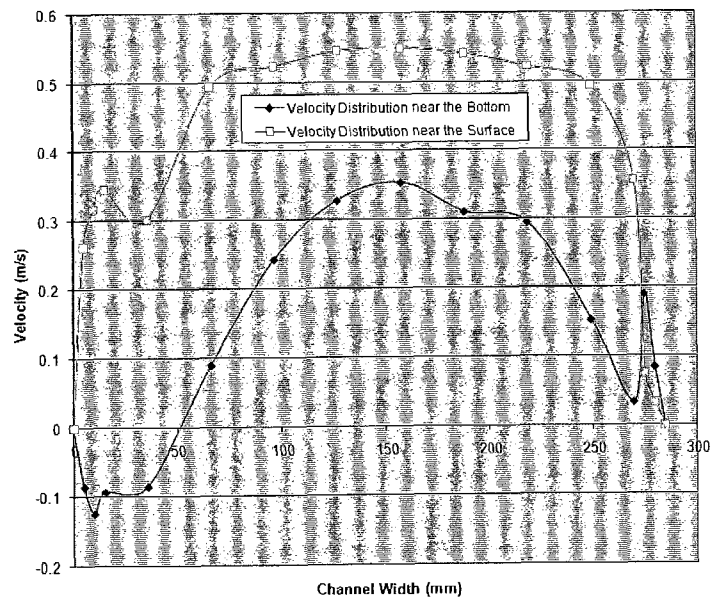
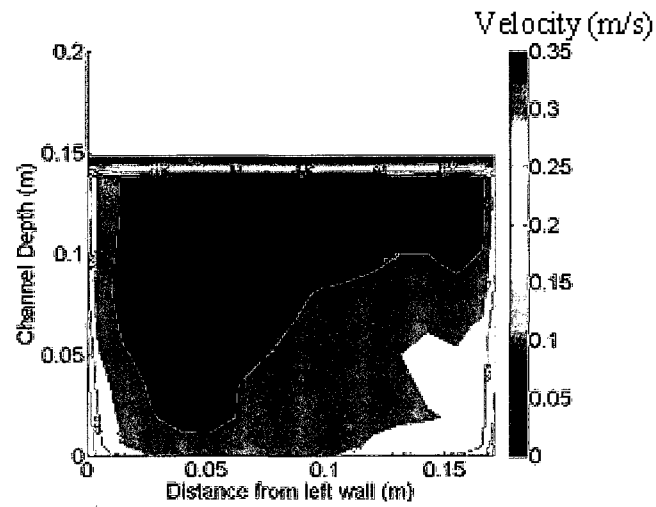
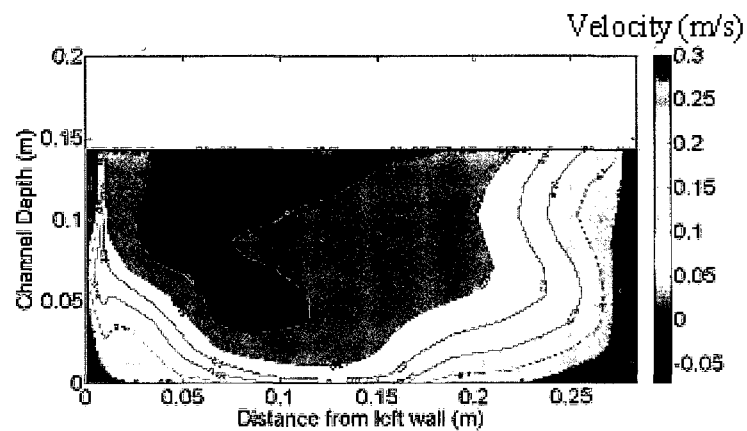


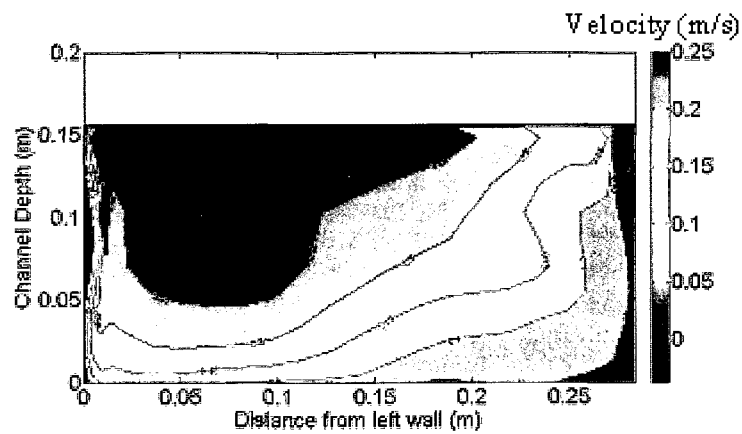
Fig. 6.5 (b) Velocity Distribution Curves at  $X = 0.325$  m (No Hump),  $Q = 0.0158$  m<sup>3</sup>/s



(a) Section at  $x = 0.0$  m (Entry)

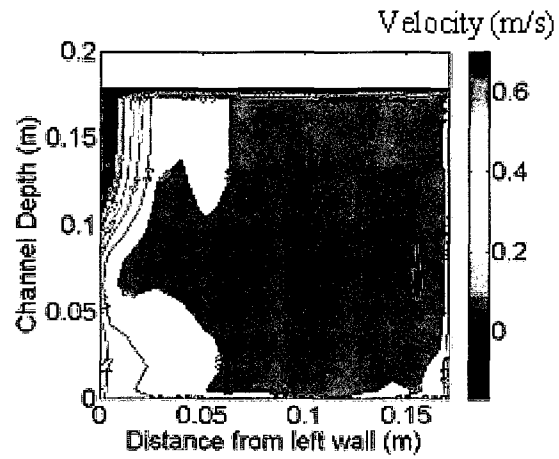
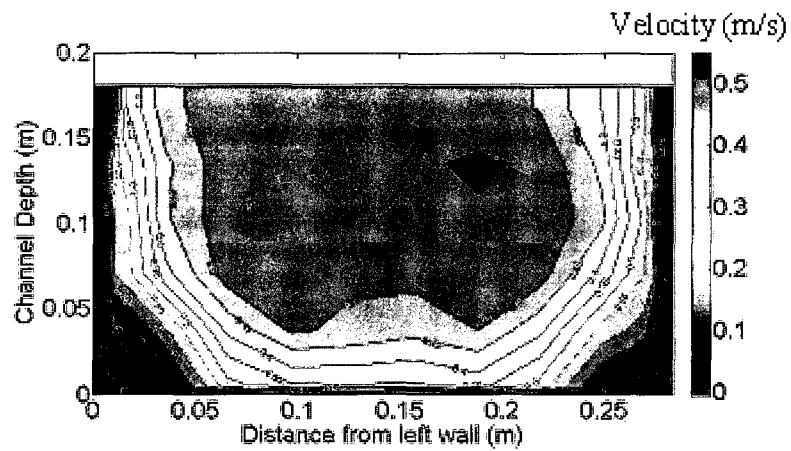
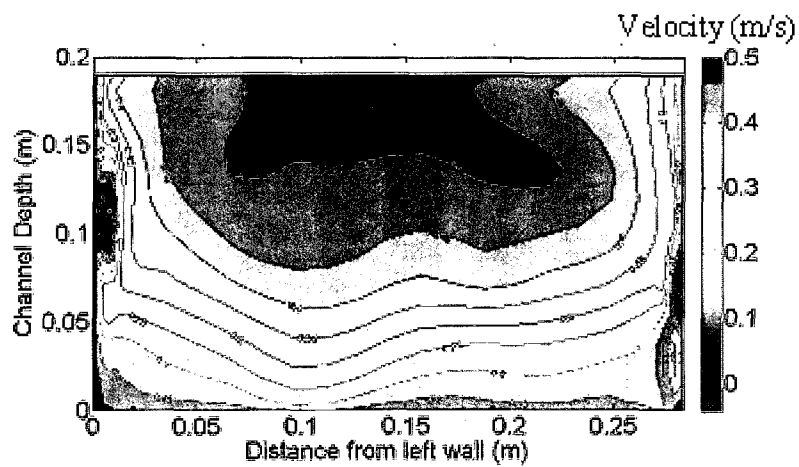


(b) Section at  $x = 0.325$  m (Exit)

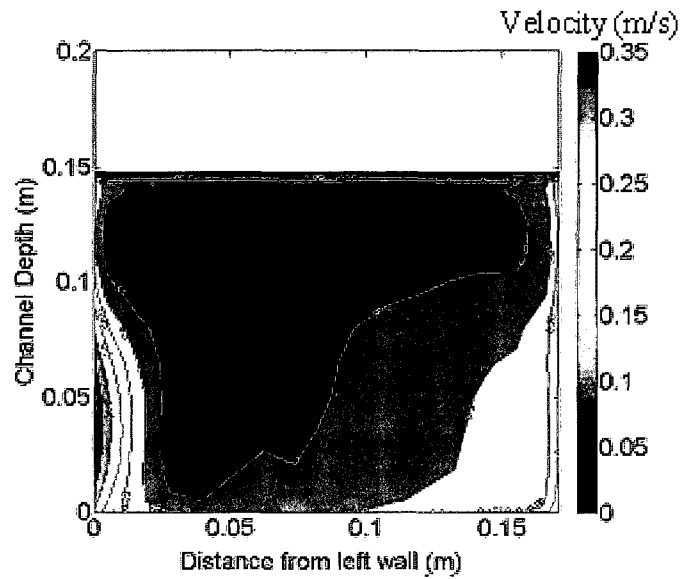
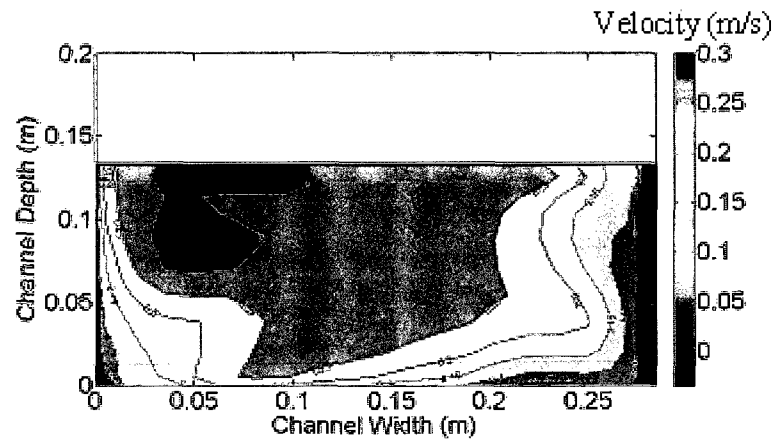
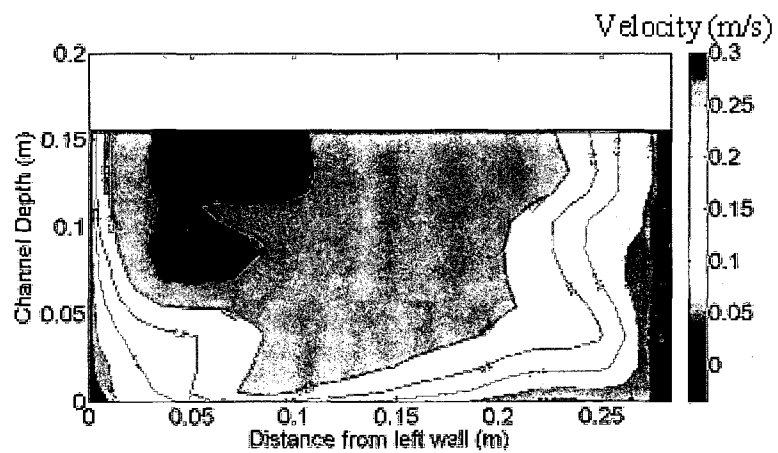


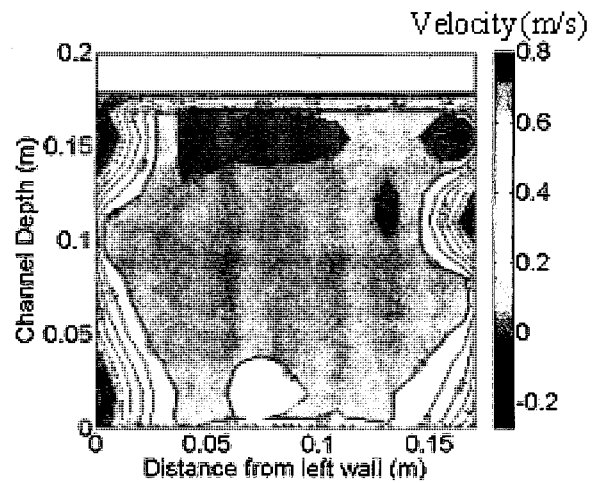
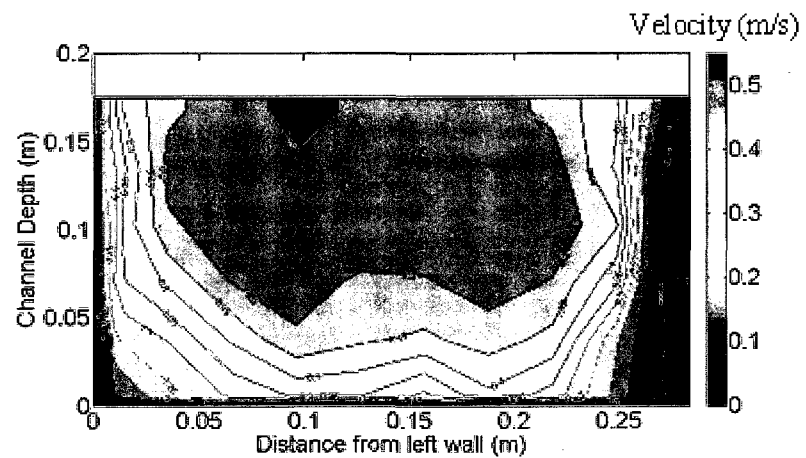
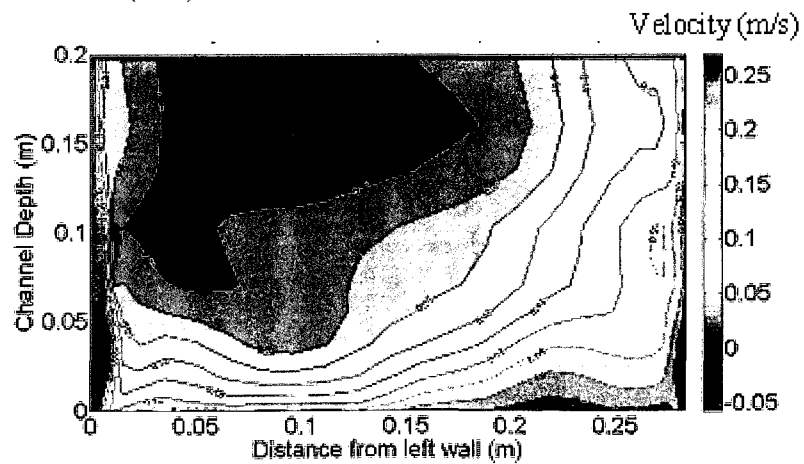
(c) Section at  $x = 0.650$  m (Downstream)

Fig. 6.6 Velocity Contours with 12.5 mm Hump for  $Q = 0.0070$  m<sup>3</sup>/s

(a) Section at  $x = 0.0$  m (Entry)(b) Section at  $x = 0.325$  m (Exit)(c) Section at  $x = 0.650$  m (Downstream)Fig. 6.7 Velocity Contours with 12.5 mm Hump for  $Q = 0.0168 \text{ m}^3/\text{s}$



(a) Section at  $x = 0.0$  m (Entry)(b) Section at  $x = 0.325$  m (Exit)(c) Section at  $x = 0.650$  m (Downstream)Fig. 6.8 Velocity Contours with 25 mm Hump for  $Q = 0.0070$  m<sup>3</sup>/s

(a) Section at  $x = 0.0$  m (Entry)Section at  $x = 0.325$  m (Exit)(c) Section at  $x = 0.650$  m (Down stream)Fig. 6.9 Velocity Contours with 25 mm Hump for  $Q = 0.0158$  m<sup>3</sup>/s

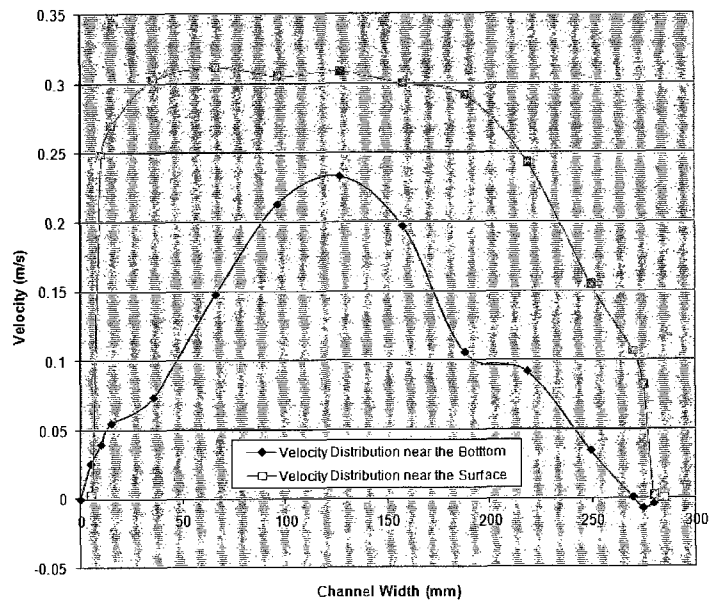


Fig.6.10 (a) Velocity Distribution Curves at X = 0.325 m (12.5 mm Hump),  
Q = 0.0070 m<sup>3</sup>/s

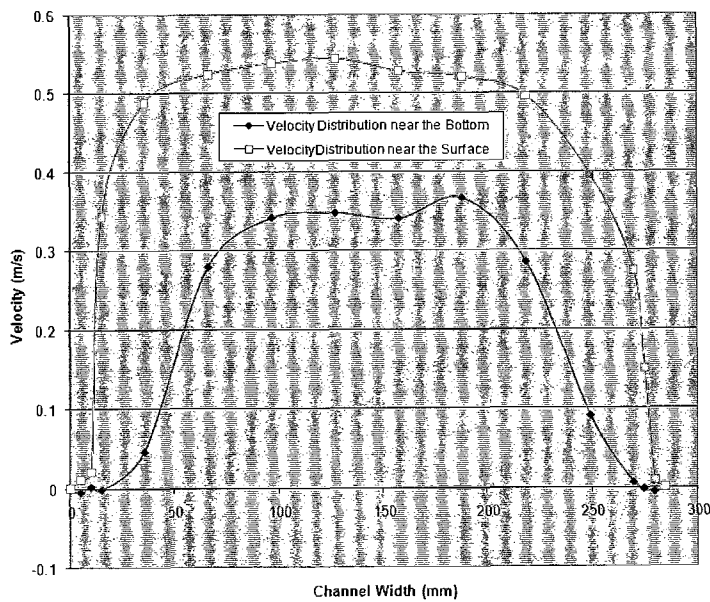


Fig. 6.10(b) Velocity Distribution Curves at X = 0.325 m (12.5 mm Hump),  
Q = 0.0168 m<sup>3</sup>/s

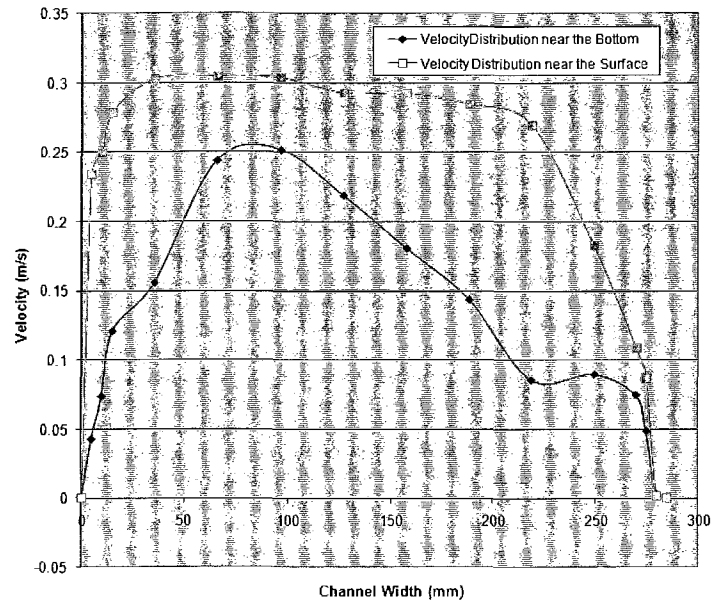


Fig. 6.11(a) Velocity Distribution Curves at  $X = 0.325$  m (25 mm Hump),  $Q_2 = 0.0070$  m<sup>3</sup>/s

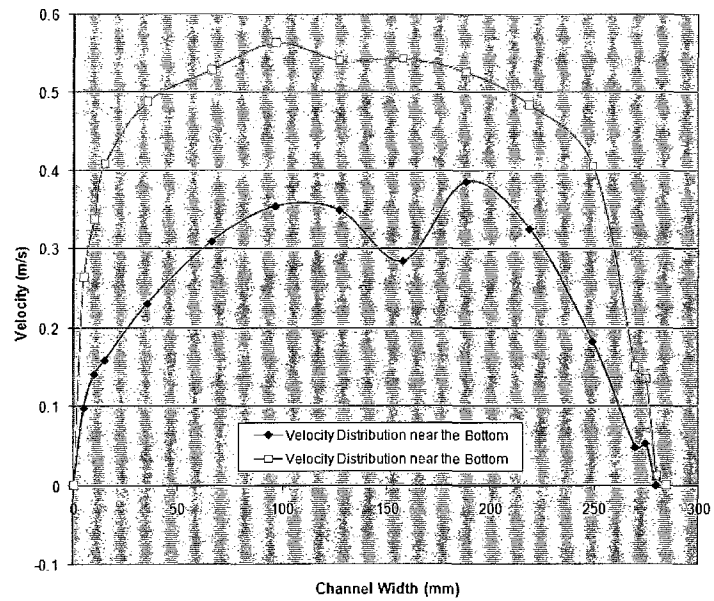
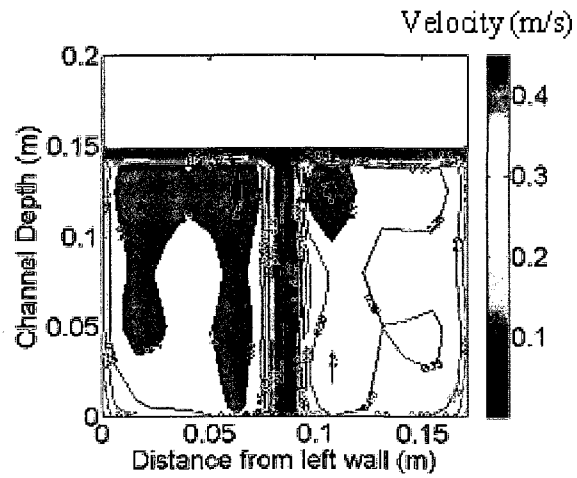
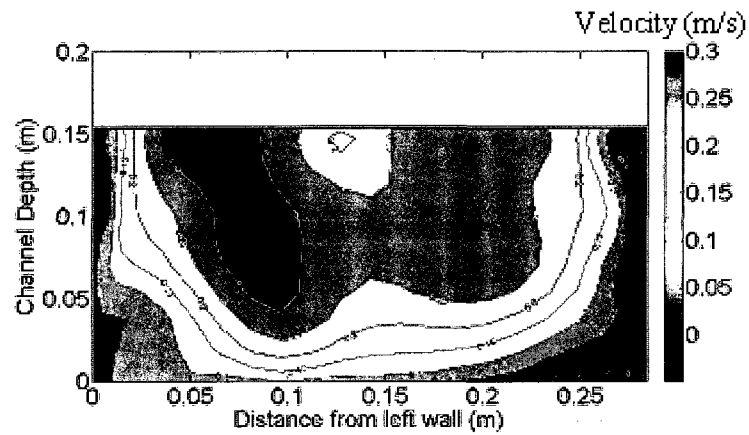
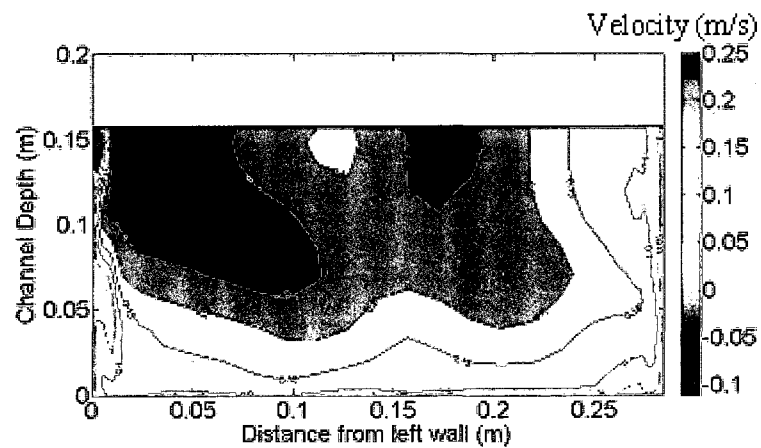
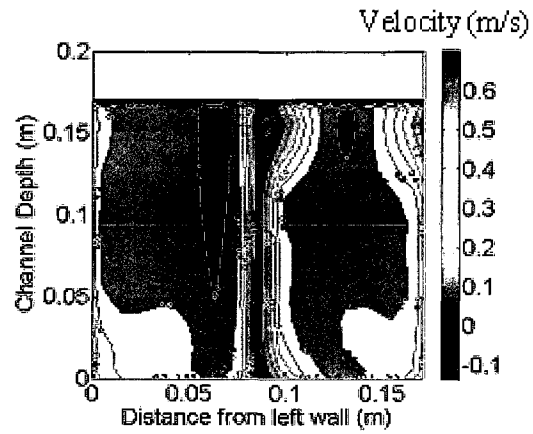
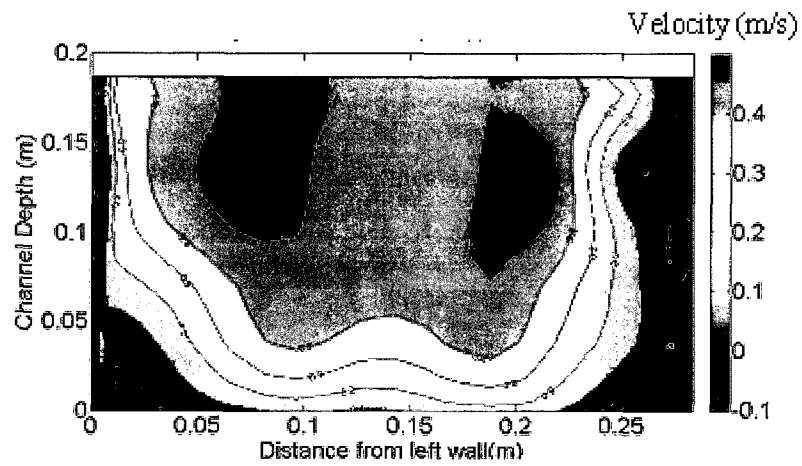
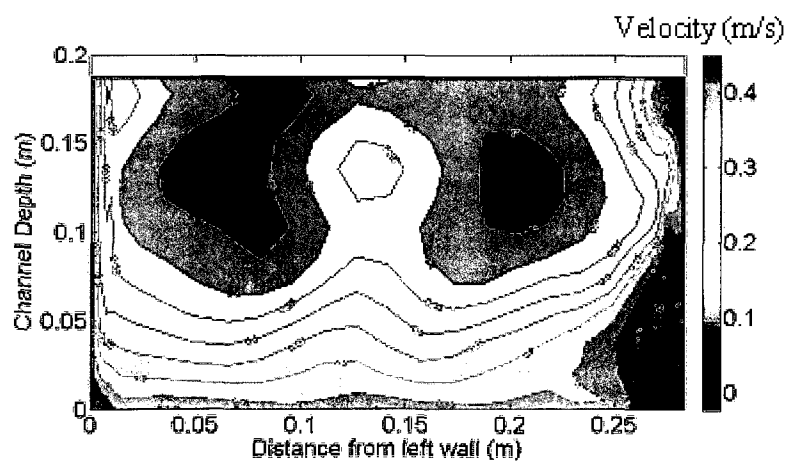
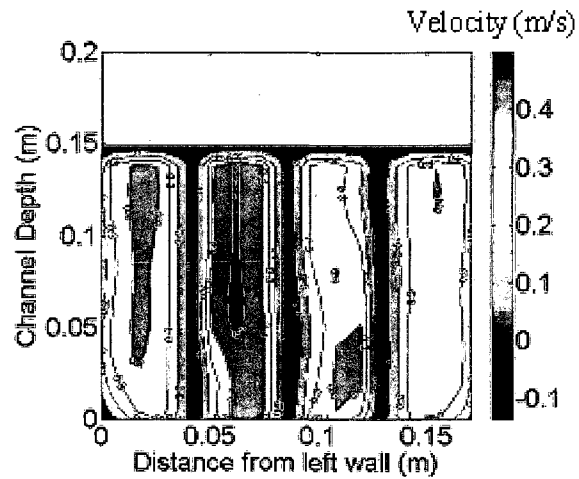
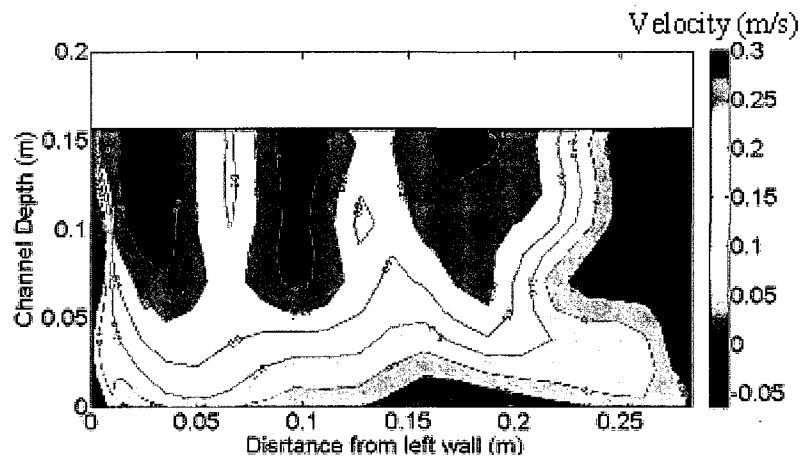
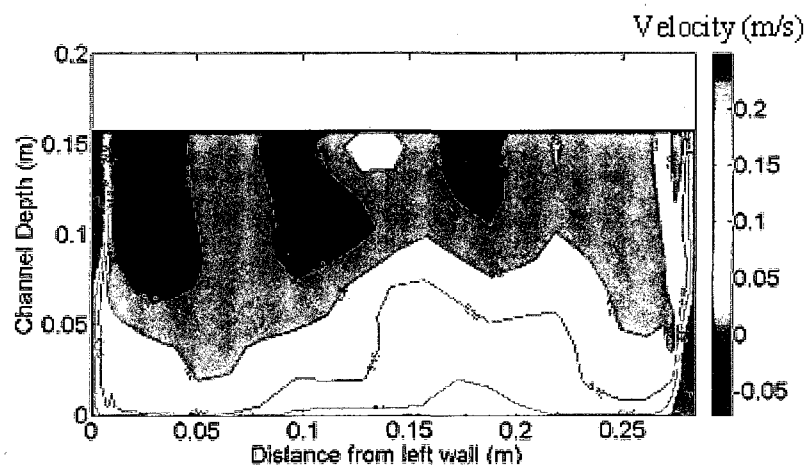
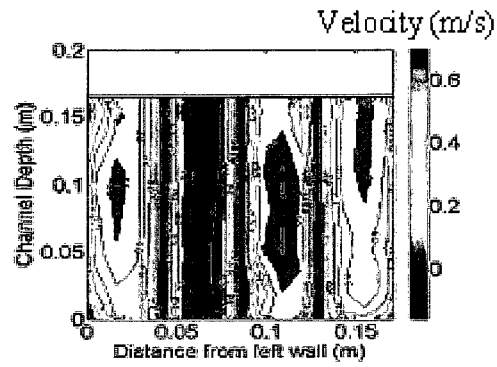
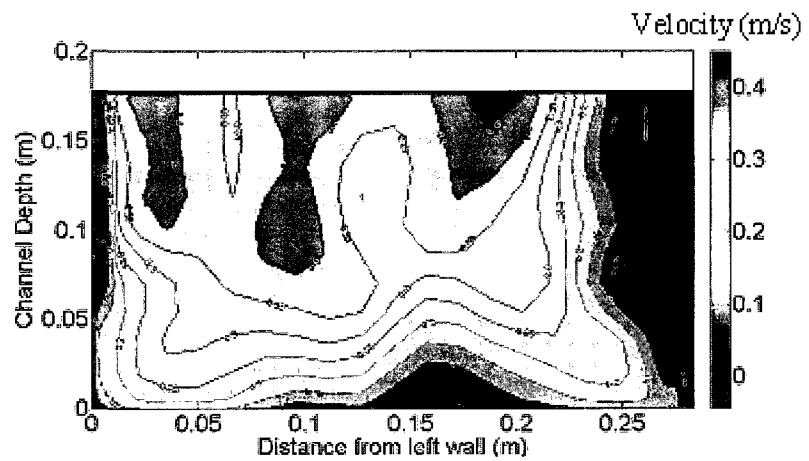
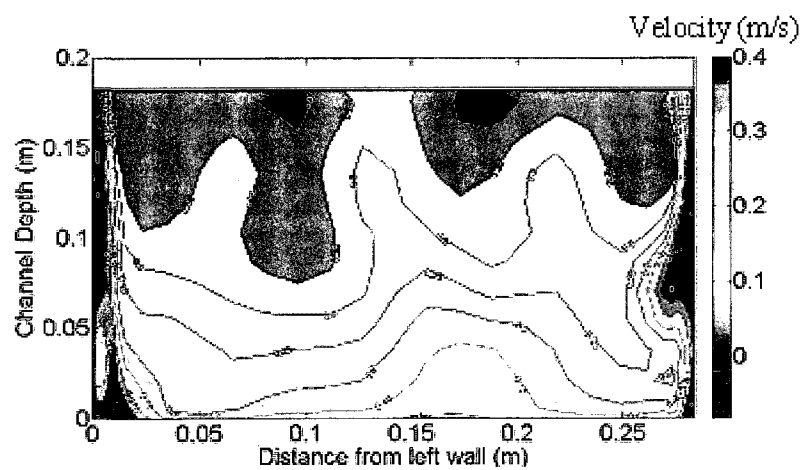


Fig. 6.11(b) Velocity Distribution Curves at  $X = 0.325$  m (25 mm Hump),  $Q = 0.0158$  m<sup>3</sup>/s

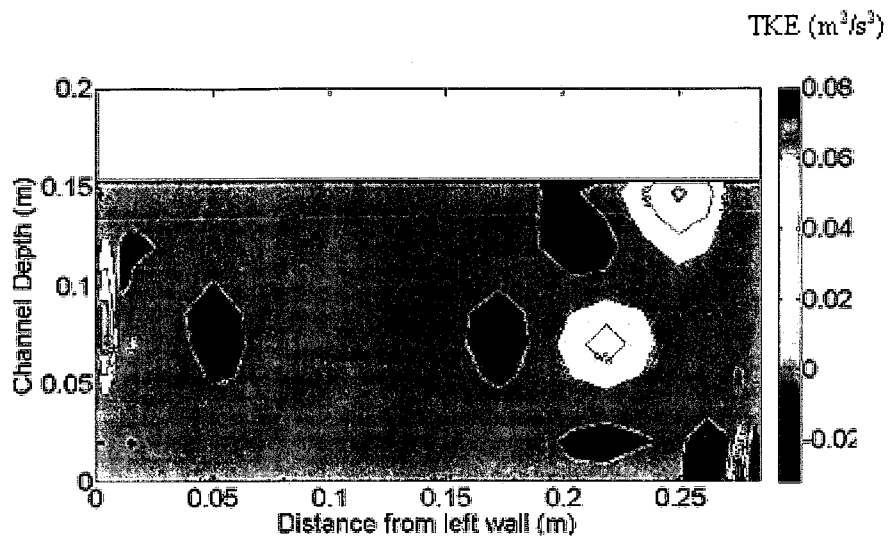
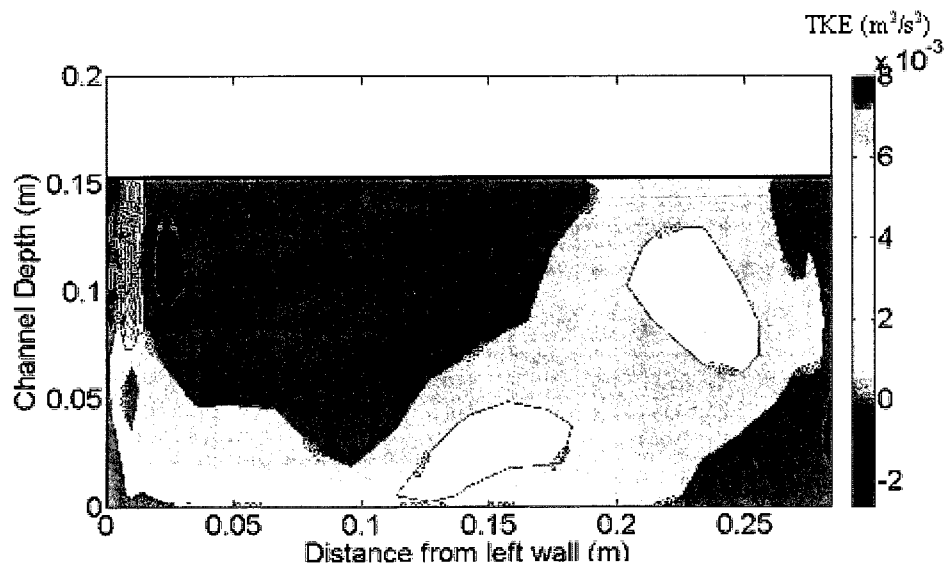
(a) Section at  $x = 0.0$  m (Entry)(b) Section at  $x = 0.325$  m (Exit)(c) Section at  $x = 0.650$  m (Down stream)Fig. 6.12 Velocity Contours with 1 Vane for  $Q = 0.0070$  m<sup>3</sup>/s

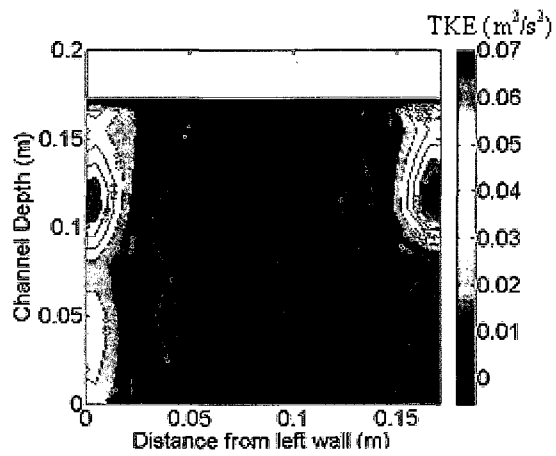
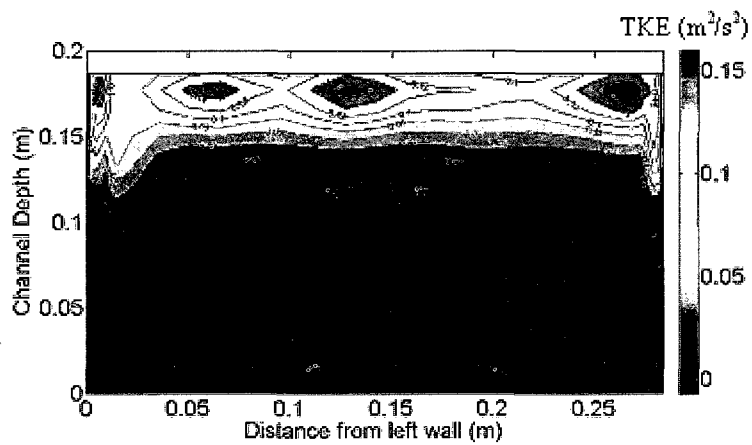
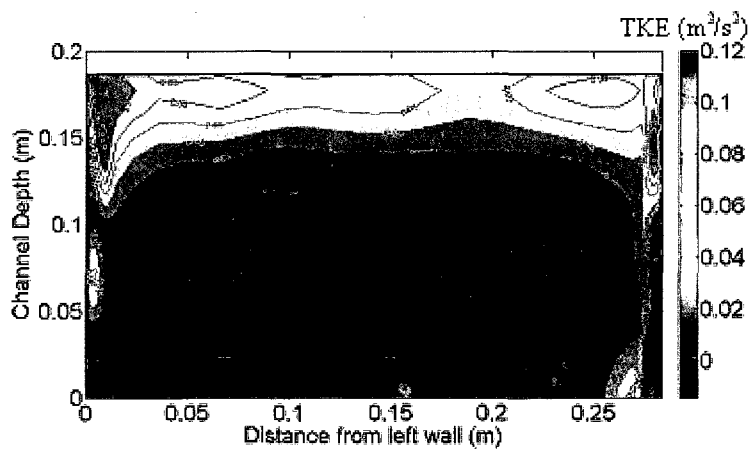
(a) Section at  $x = 0.0$  m (Entry)(b) Section at  $x = 0.325$  m (Exit)(c) Section at  $x = 0.650$  m (Down stream)Fig. 6.13 Velocity Contours with 1 Vane for  $Q = 0.0142$  m<sup>3</sup>/s

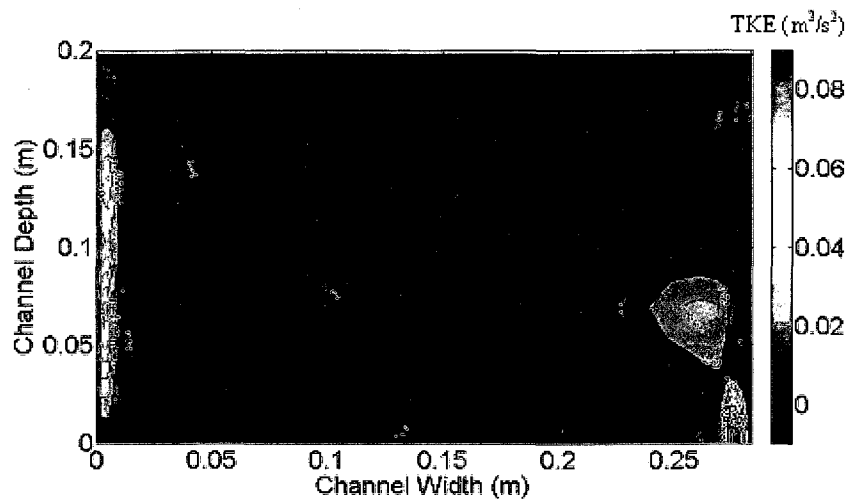
(a) Section at  $x = 0.0$  m (Entry)(b) Section at  $x = 0.325$  m (Exit)(c) Section at  $x = 0.650$  m (Down stream)Fig. 6.14 Velocity Contours with 3 Vanes for  $Q = 0.0070$

(a) Section at  $x = 0.0$  m (Entry)(b) Section at  $x = 0.325$  m (Exit)(c) Section at  $x = 0.650$  m (Down stream)Fig. 6.15 Velocity Contours with 3 Vanes for  $Q = 0.0142 \text{ m}^3/\text{s}$

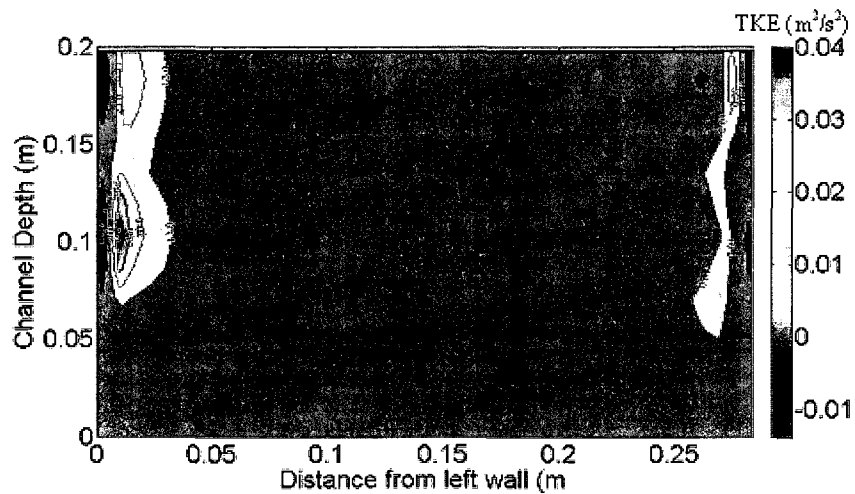


(a) Section at  $x = 0.325$  m (Exit)(a) Section at  $x = 0.650$  m (Down stream)Fig.6.16 Turbulence Kinetic Energy without Hump for  $Q = 0.0070 \text{ m}^3/\text{s}$

(a) Section at  $x = 0.0 \text{ m}$  (Entry)(b) Section at  $x = 0.325 \text{ m}$  (Exit)(c) Section at  $x = 0.650 \text{ m}$  (Down stream)Fig.6.17 Turbulence Kinetic Energy without Hump for  $Q = 0.0142 \text{ m}^3/\text{s}$



(a) Section at  $x = 0.325 \text{ m}$  (Exit)



(b) Section at  $x = 0.650 \text{ m}$  (Down stream)

Fig.6.18 Turbulence Kinetic Energy without Hump for  $Q = 0.0158 \text{ m}^3/\text{s}$

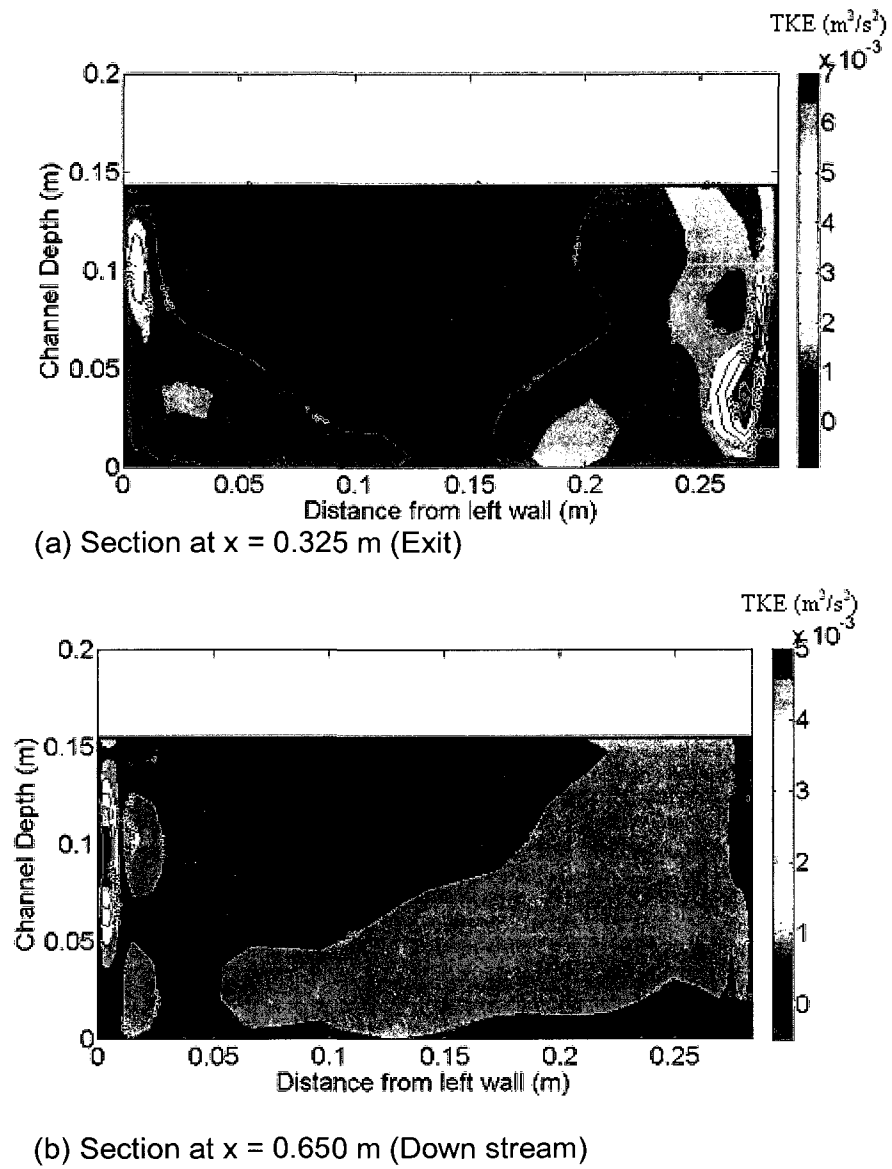
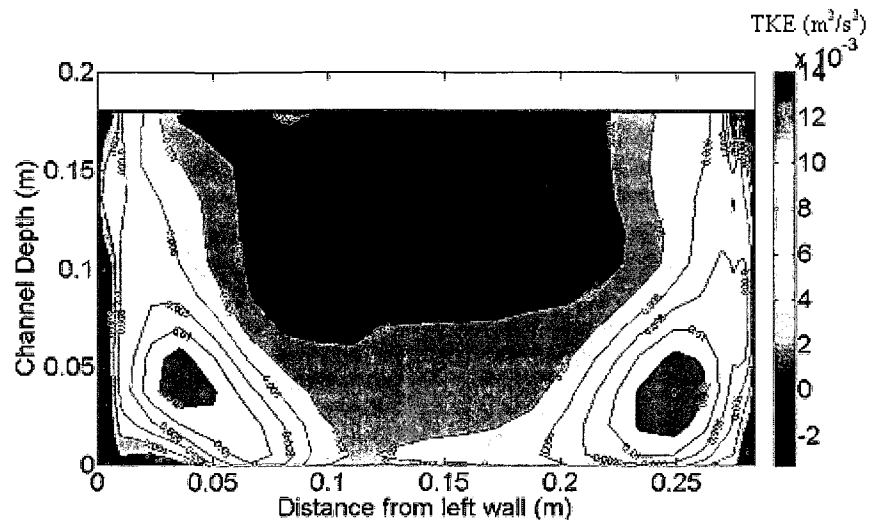
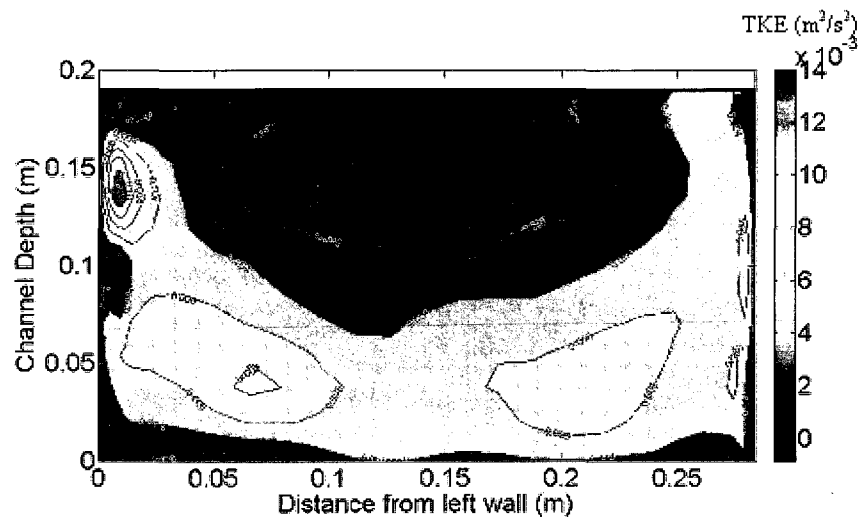
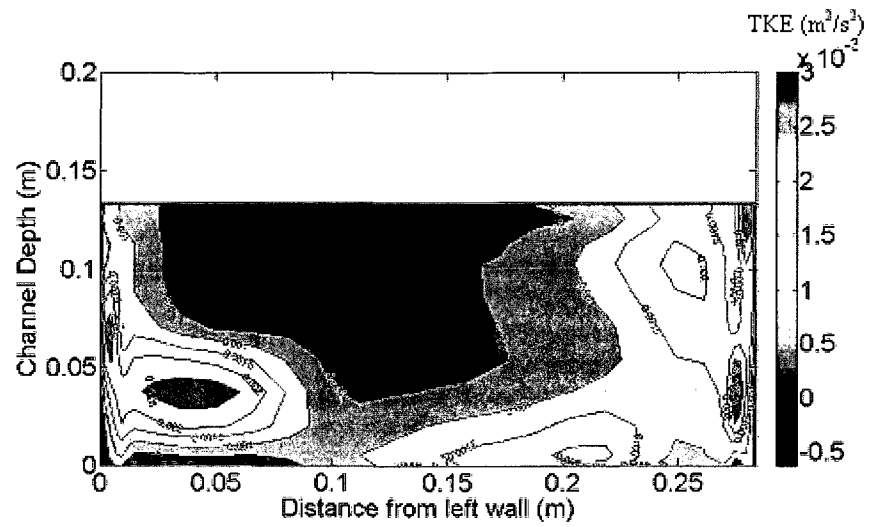
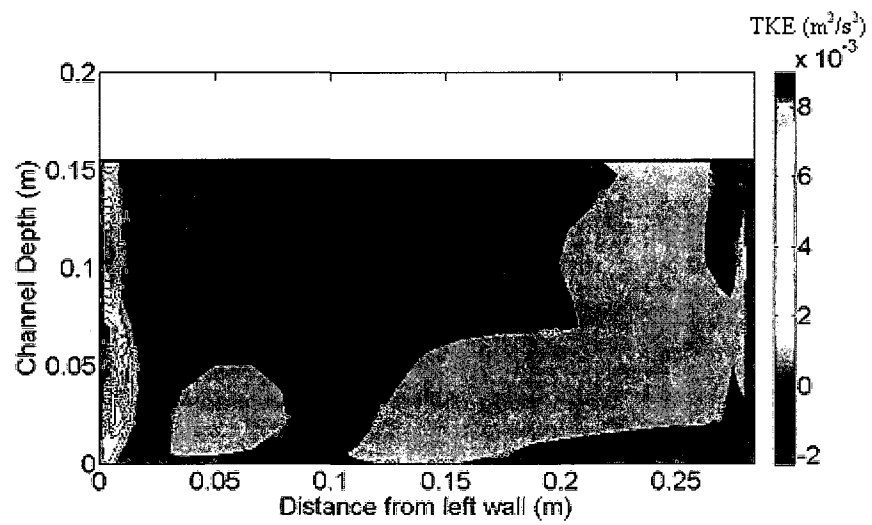


Fig.6.19 Turbulence Kinetic Energy with 12.5 mm Hump for  $Q = 0.0070$   $\text{m}^3/\text{s}$

(a) Section at  $x = 0.325$  m (Exit)(b) Section at  $x = 0.650$  m (Down stream)Fig. 6.20 Turbulence Kinetic Energy with 12.5 mm Hump for  $Q = 0.0168$  m<sup>3</sup>/s

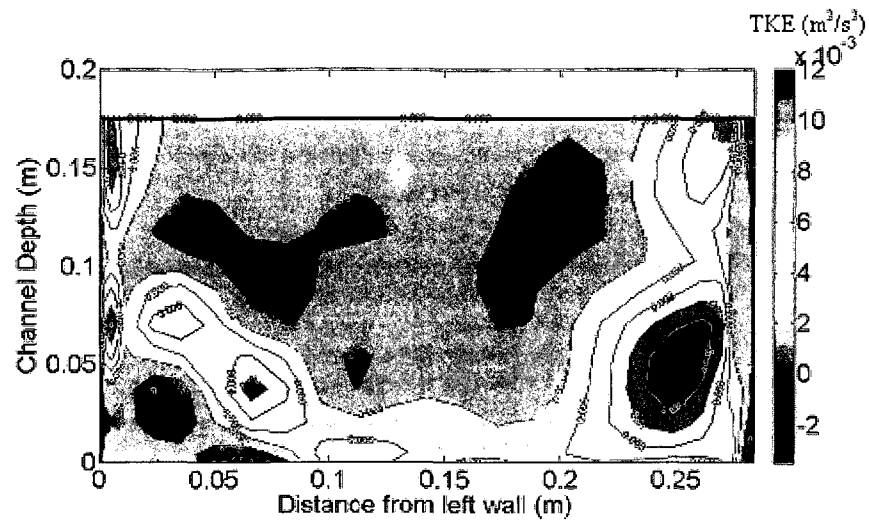


(a) Section at  $x = 0.325$  m (Exit)

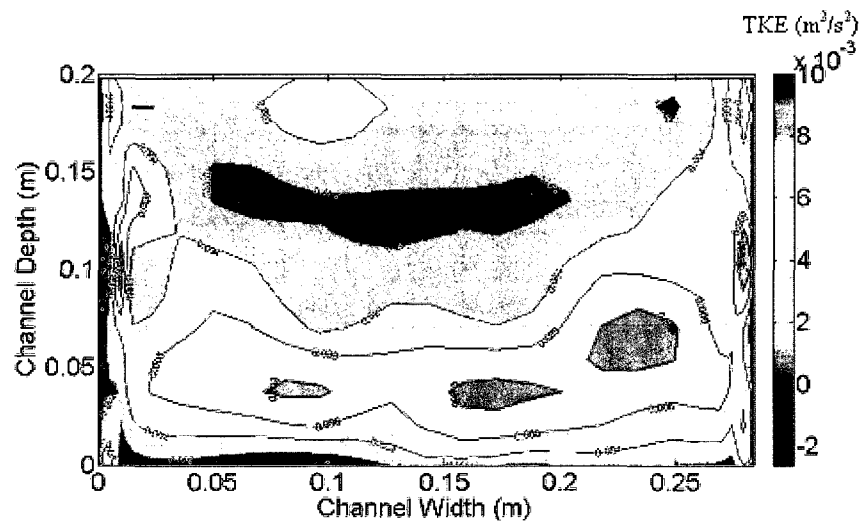


(b) Section at  $x = 0.650$  m (Down stream)

Fig.6.21 Turbulence Kinetic Energy with 25 mm Hump for  $Q = 0.0070$   $\text{m}^3/\text{s}$

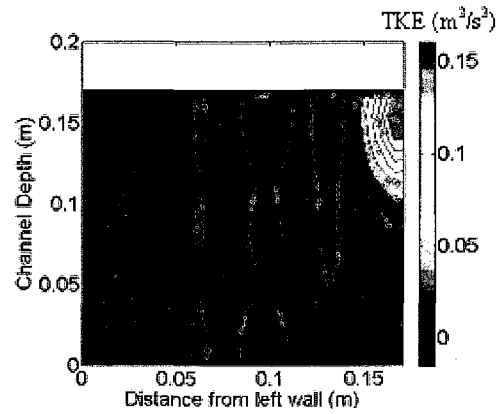
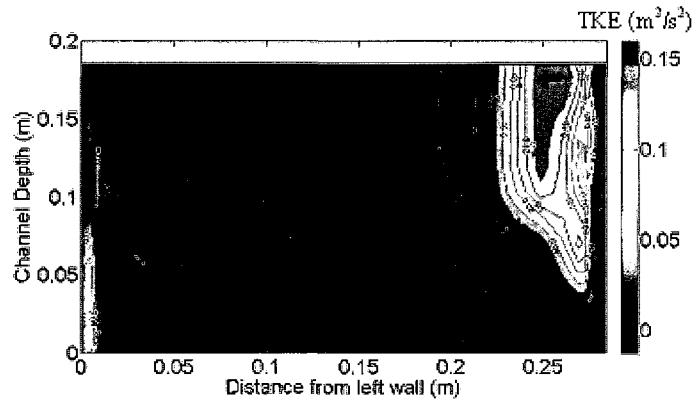
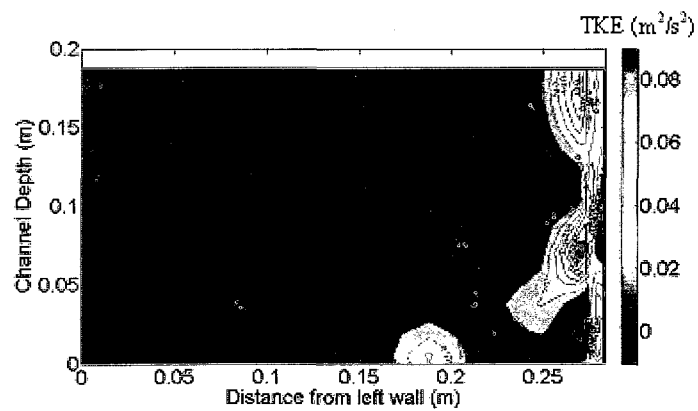


(a) Section at  $x = 0.325$  m (Exit)

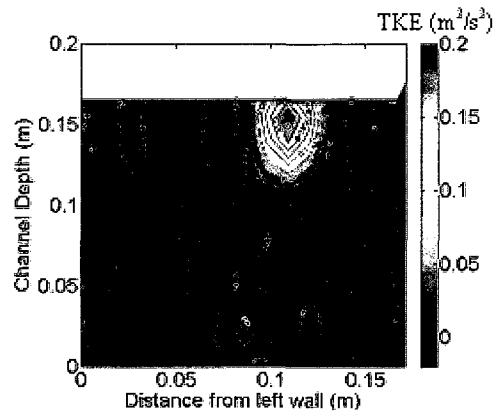
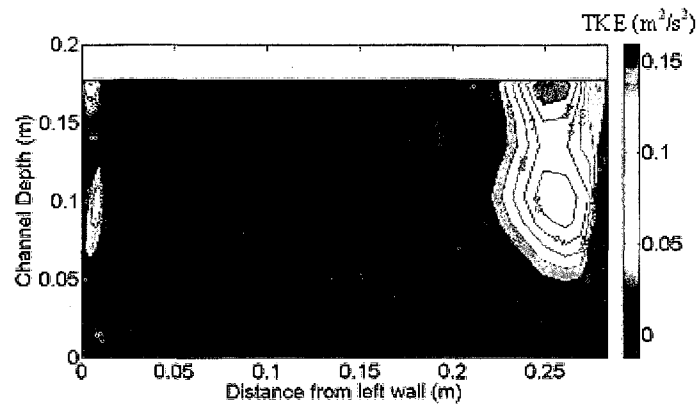
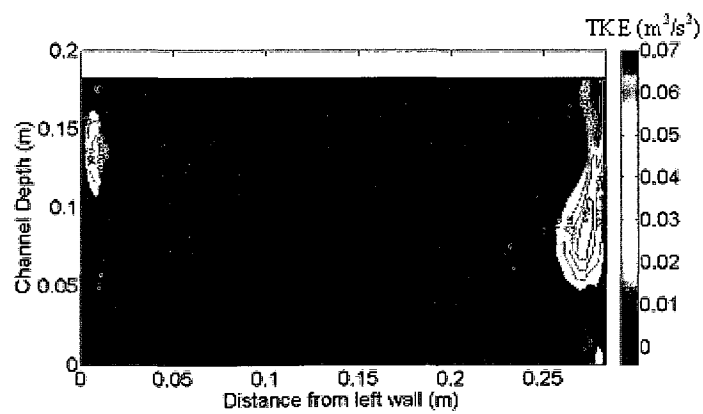


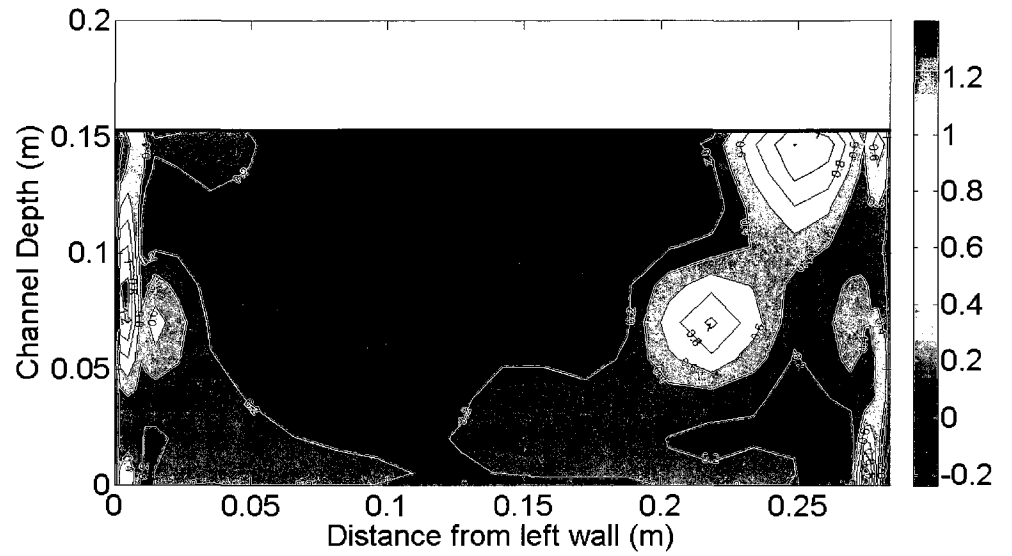
(b) Section at  $x = 0.650$  m (Down stream)

Fig.6.22 Turbulence Kinetic Energy with 25 mm Hump for  $Q = 0.0158$   $\text{m}^3/\text{s}$

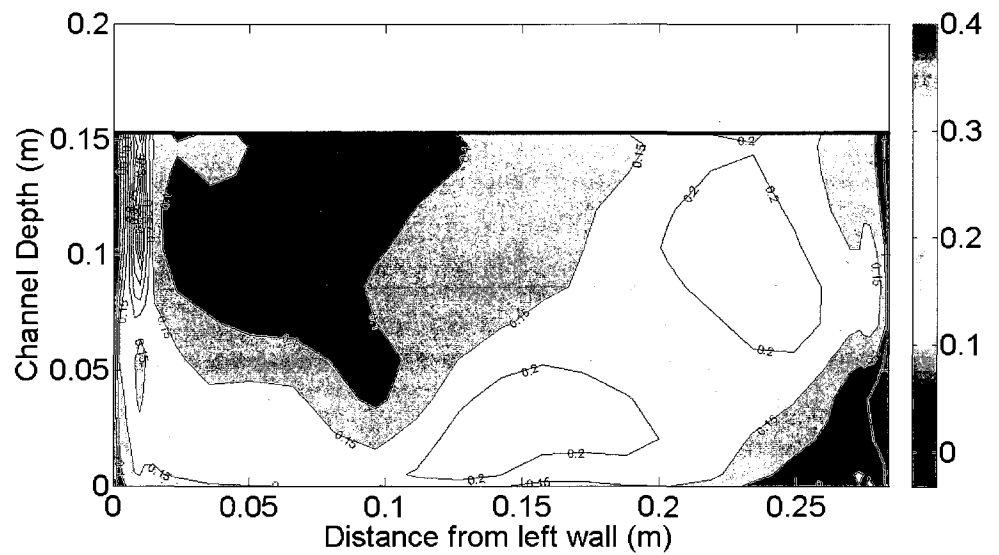
(a) Section at  $x = 0.0$  m (Entry)(b) Section at  $x = 0.325$  m (Exit)(c) Section at  $x = 0.650$  m (Down stream)Fig.6.23 Turbulence Kinetic Energy with 1 Vane for  $Q=0.0142$  m<sup>3</sup>/s



(a) Section at  $x = 0.0$  m (Entry)(b) Section at  $x = 0.325$  m (Exit)(c) Section at  $x = 0.650$  m (Down stream)Fig.6.24 Turbulence Kinetic Energy with 3 Vanes for  $Q = 0.0142$  m<sup>3</sup>/s

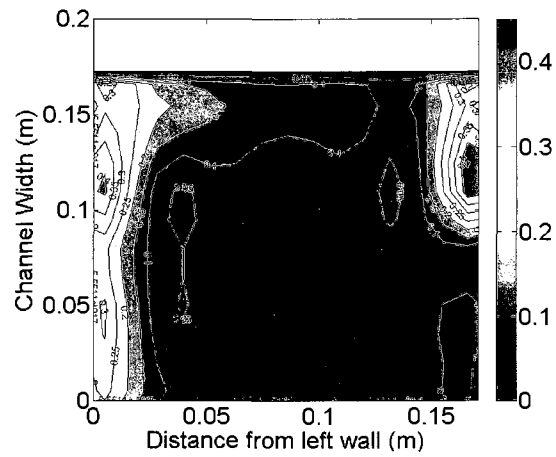
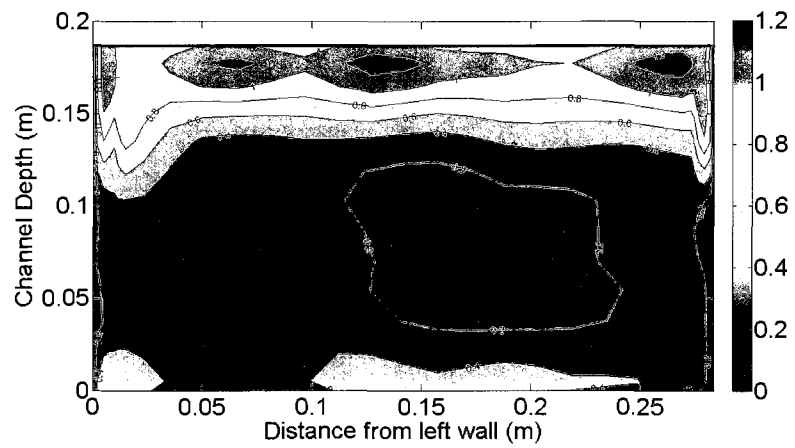
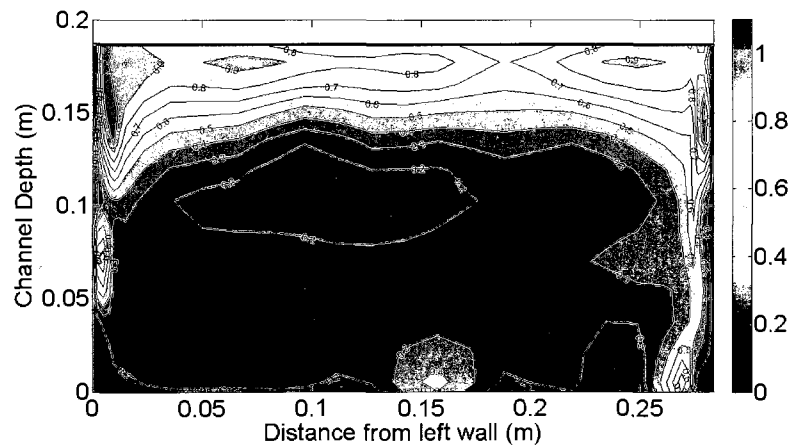


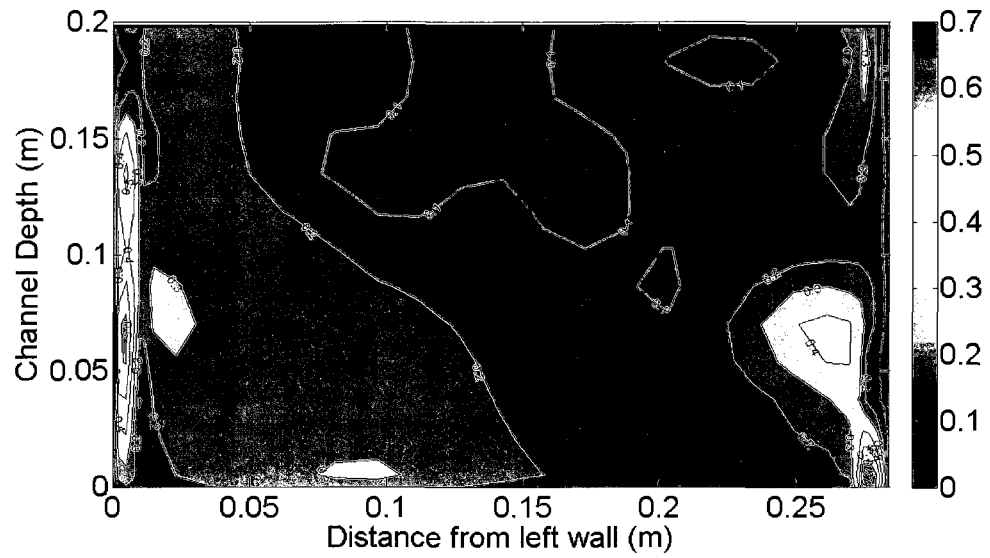
(a) Section at  $x = 0.325$  m (Exit)



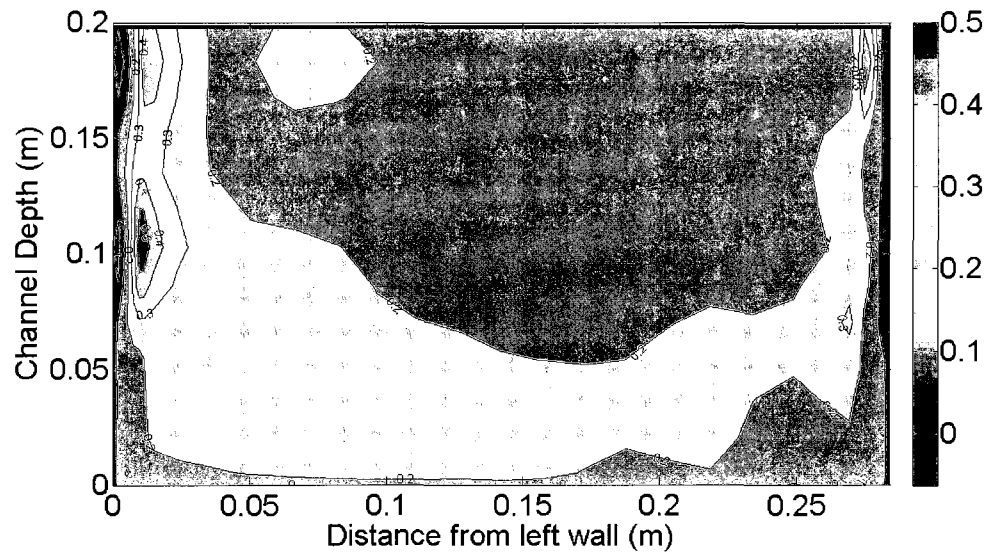
(b) Section at  $x = 0.650$  m (Down stream)

Fig.6.25 Turbulence Intensity without Hump for  $Q = 0.0070$  m<sup>3</sup>/s

(a) Section at  $x = 0.0$  m (Entry)(b) Section at  $x = 0.325$  m (Exit)(c) Section at  $x = 0.650$  m (Down stream)Fig.6.26 Turbulence Intensity without Hump for  $Q = 0.0142 \text{ m}^3/\text{s}$

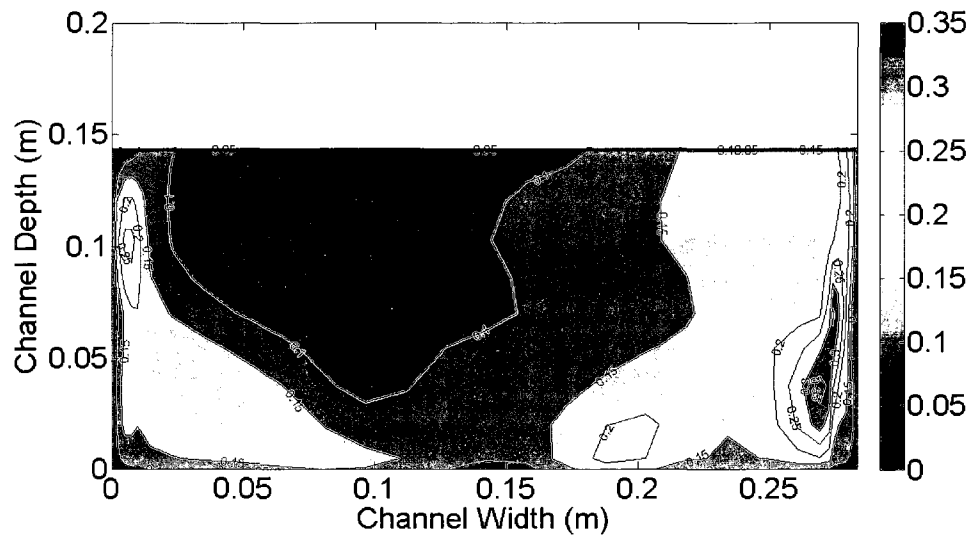
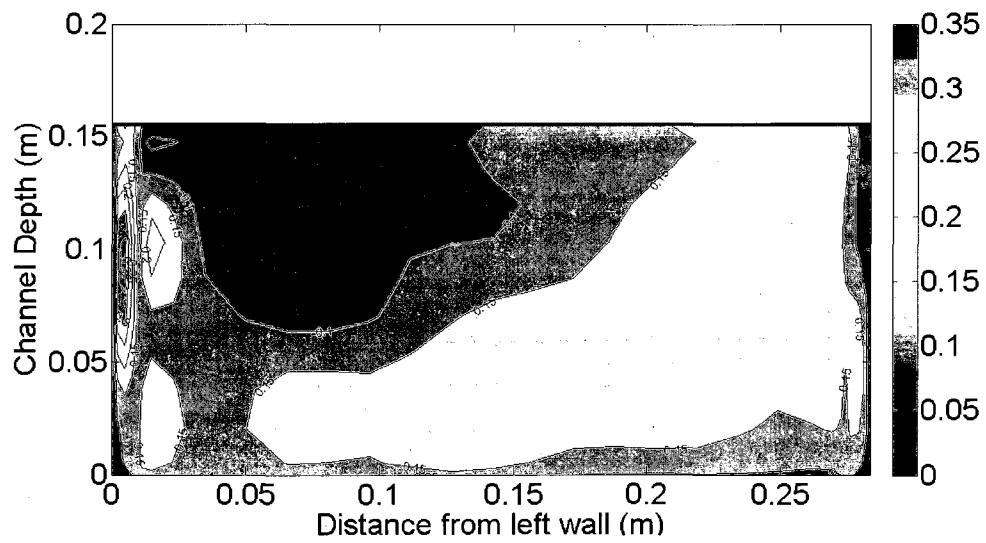


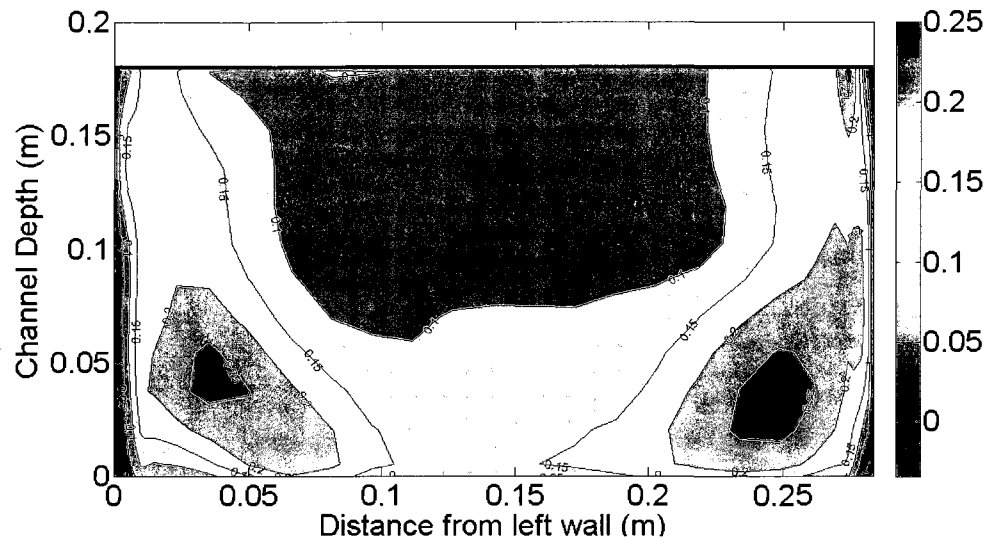
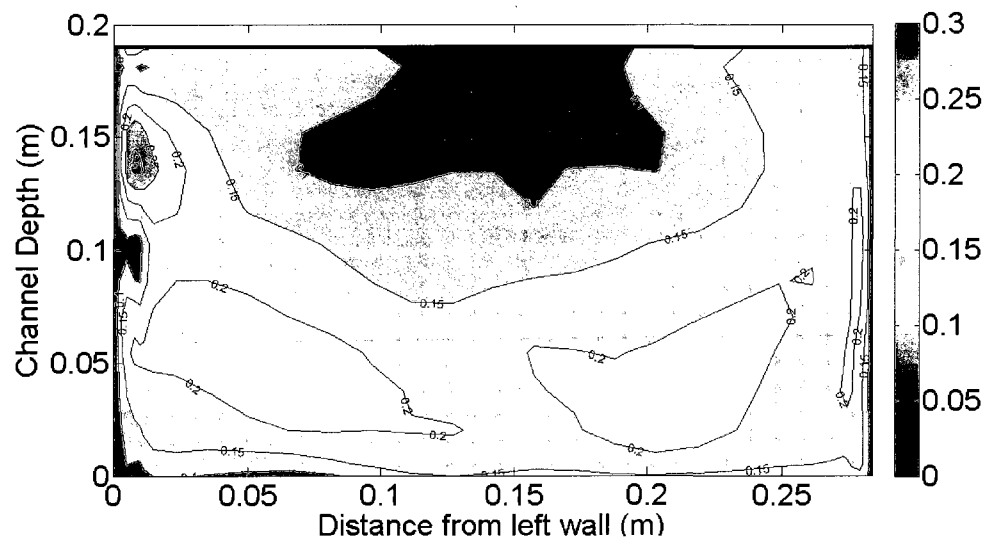
(a) Section at  $x = 0.325$  m (Exit)

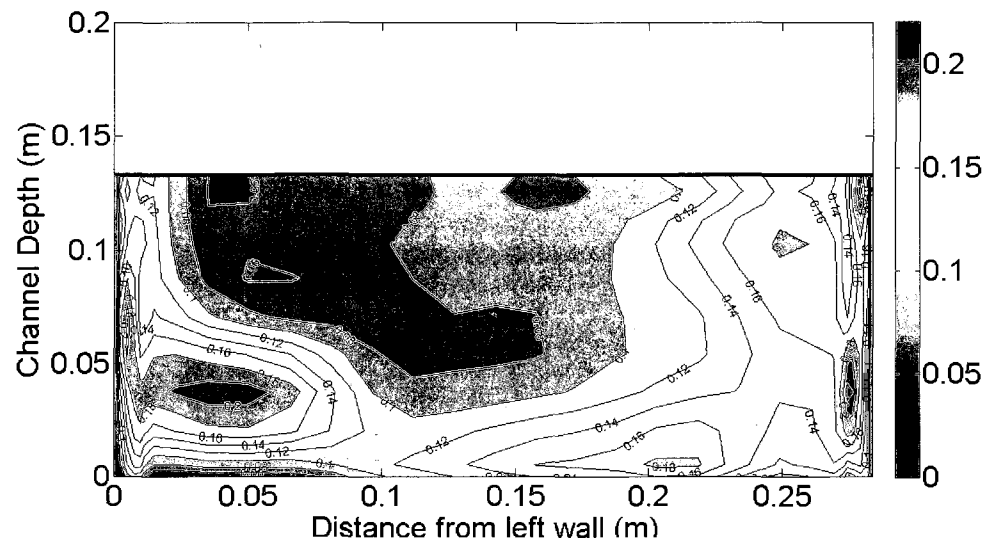


(b) Section at  $x = 0.650$  m (Down stream)

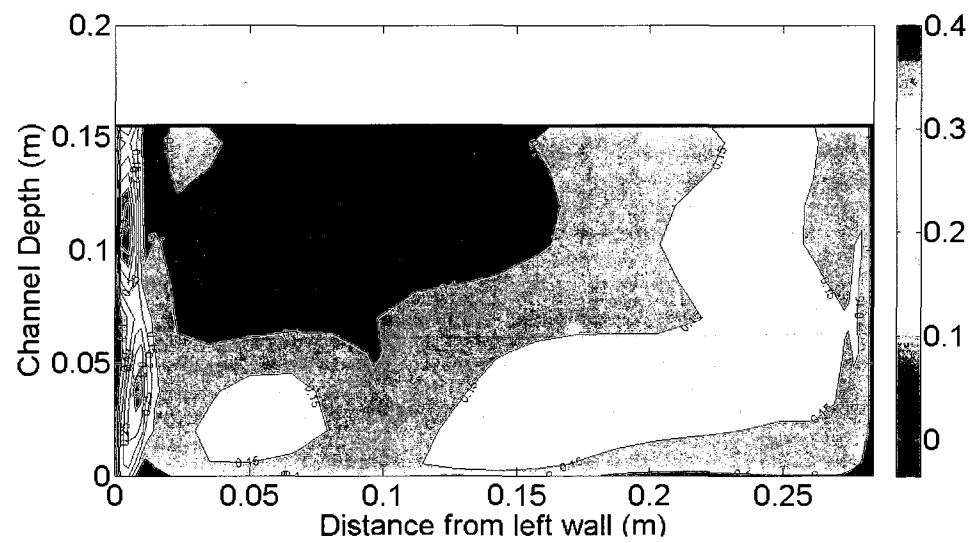
Fig. 6.27 Turbulence Intensity without Hump for  $Q = 0.0158$  m<sup>3</sup>/s

(a) Section at  $x = 0.325$  m (Exit)(b) Section at  $x = 0.650$  m (Down stream)Fig. 6.28 Turbulence Intensity with 12.5 mm Hump for  $Q = 0.0070$  m<sup>3</sup>/s

(a) Section at  $x = 0.325$  m (Entry)(b) Section at  $x = 0.650$  m (Down stream)Fig. 6.29 Turbulence Intensity with 12.5 mm Hump for  $Q = 0.0168 \text{ m}^3/\text{s}$

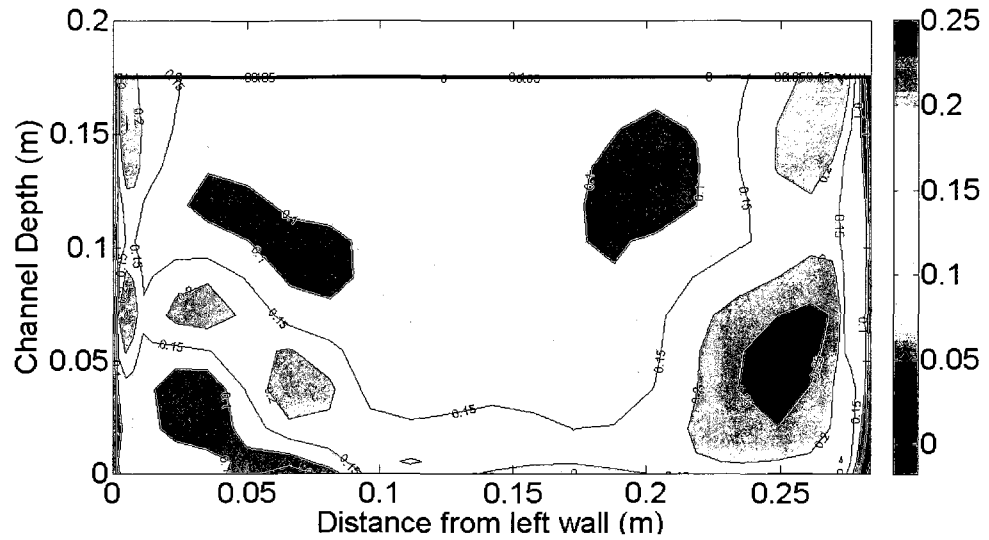


(a) Section at  $x = 0.325$  m (Exit)

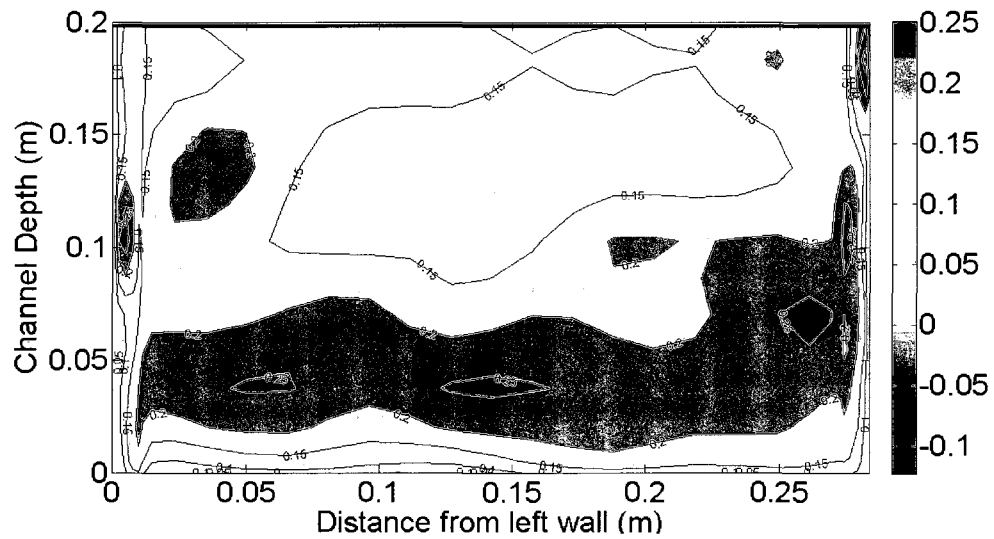


(b) Section at  $x = 0.650$  m (Down stream)

Fig. 6.30 Turbulence Intensity with 25 mm Hump for  $Q = 0.0070$  m<sup>3</sup>/s



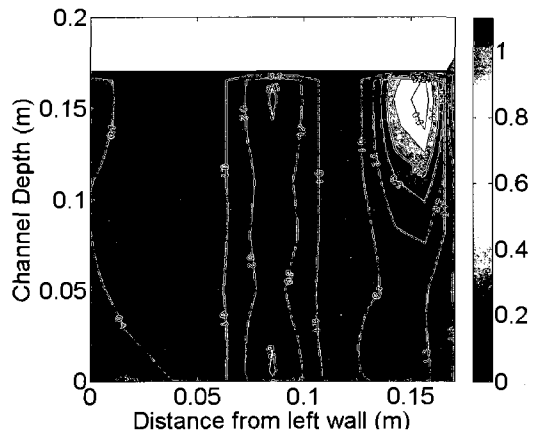
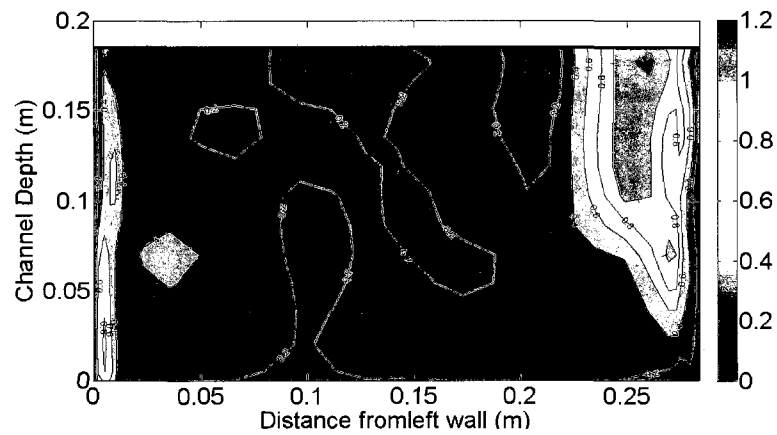
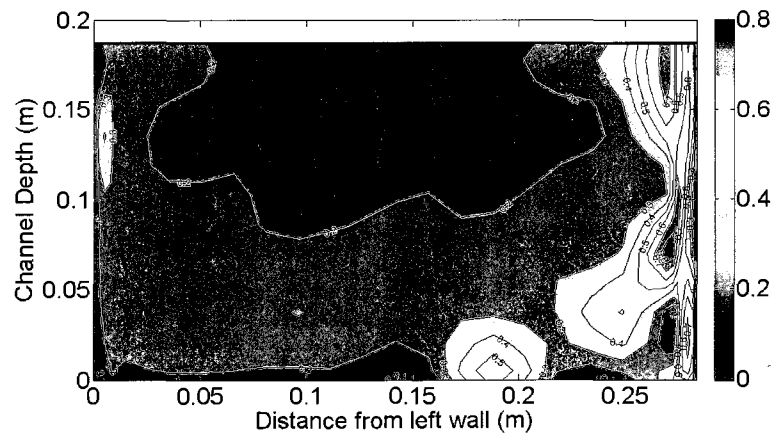
(a) Section at  $x = 0.325$  m (Exit)

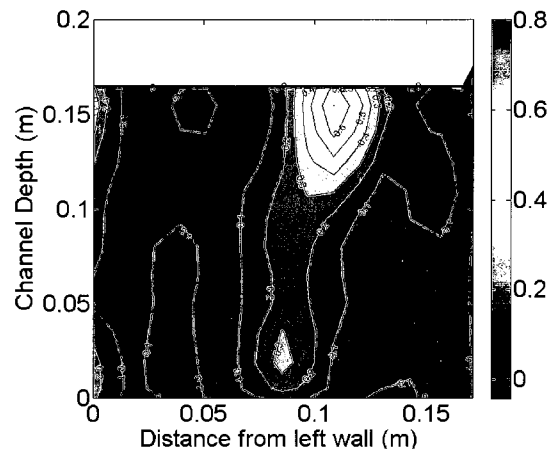
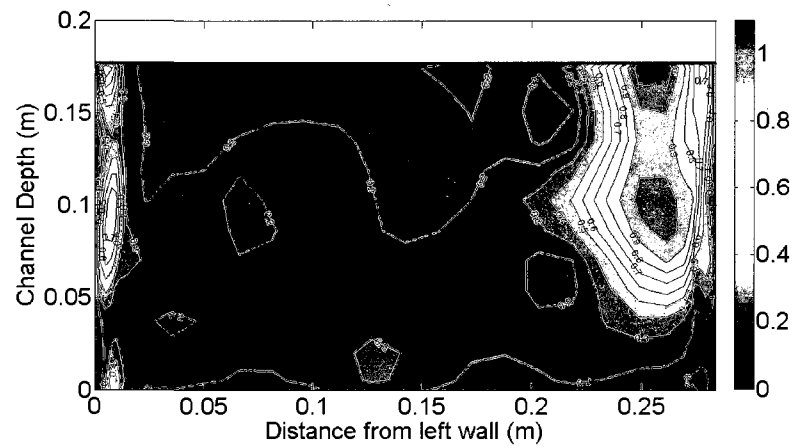
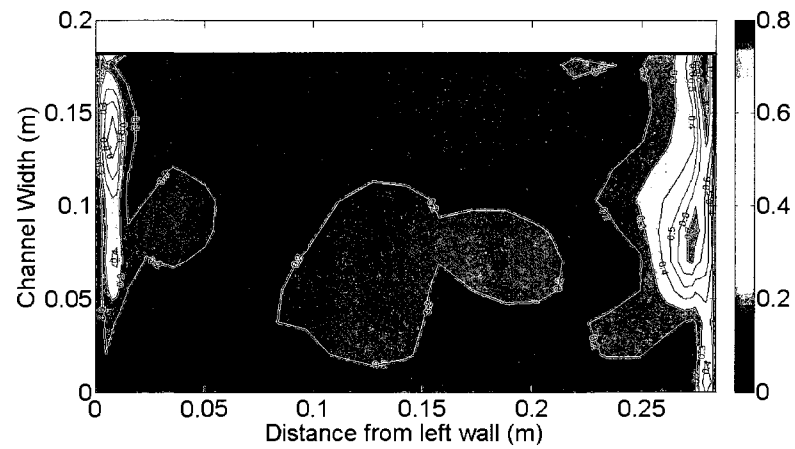


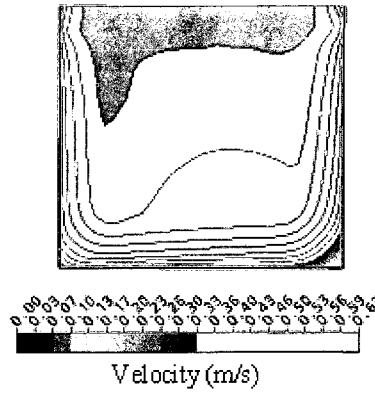
(b) Section at  $x = 0.650$  m (Down stream)

Fig. 6.31 Turbulence Intensity with 25 mm Hump for  $Q = 0.0158 \text{ m}^3/\text{s}$

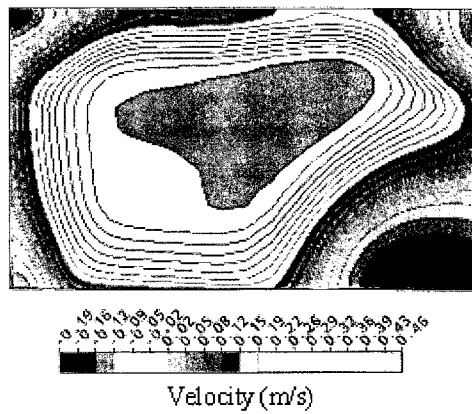


(a) Section at  $x = 0.0$  m (Entry)(b) Section at  $x = 0.325$  m (Exit)(c) Section at  $x = 0.650$  m (Down stream)Fig. 6.32 Turbulence Intensity with 1 Vane for  $Q = 0.0142 \text{ m}^3/\text{s}$

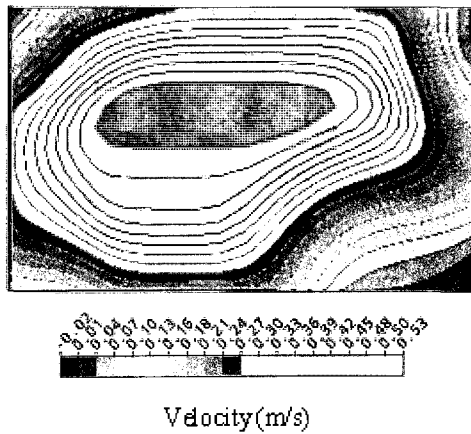
(a) Section at  $x = 0.0$  m (Entry)(b) Section at  $x = 0.325$  m (Exit)(c) Section at  $x = 0.650$  m (Down stream)Fig. 6.33 Turbulence Intensity with 3 Vanes for  $Q = 0.0142 \text{ m}^3/\text{s}$



(a) Section at  $x = 0.0$  m (Entry)



(b) Section at  $x = 0.325$  m (Exit)



(c) Section at  $x = 0.650$  m (Down stream)

Fig. 6.34 Simulated Velocity ( $u$ , m/s) Contours without Hump for  $Q = 0.0133 \text{ m}^3/\text{s}$

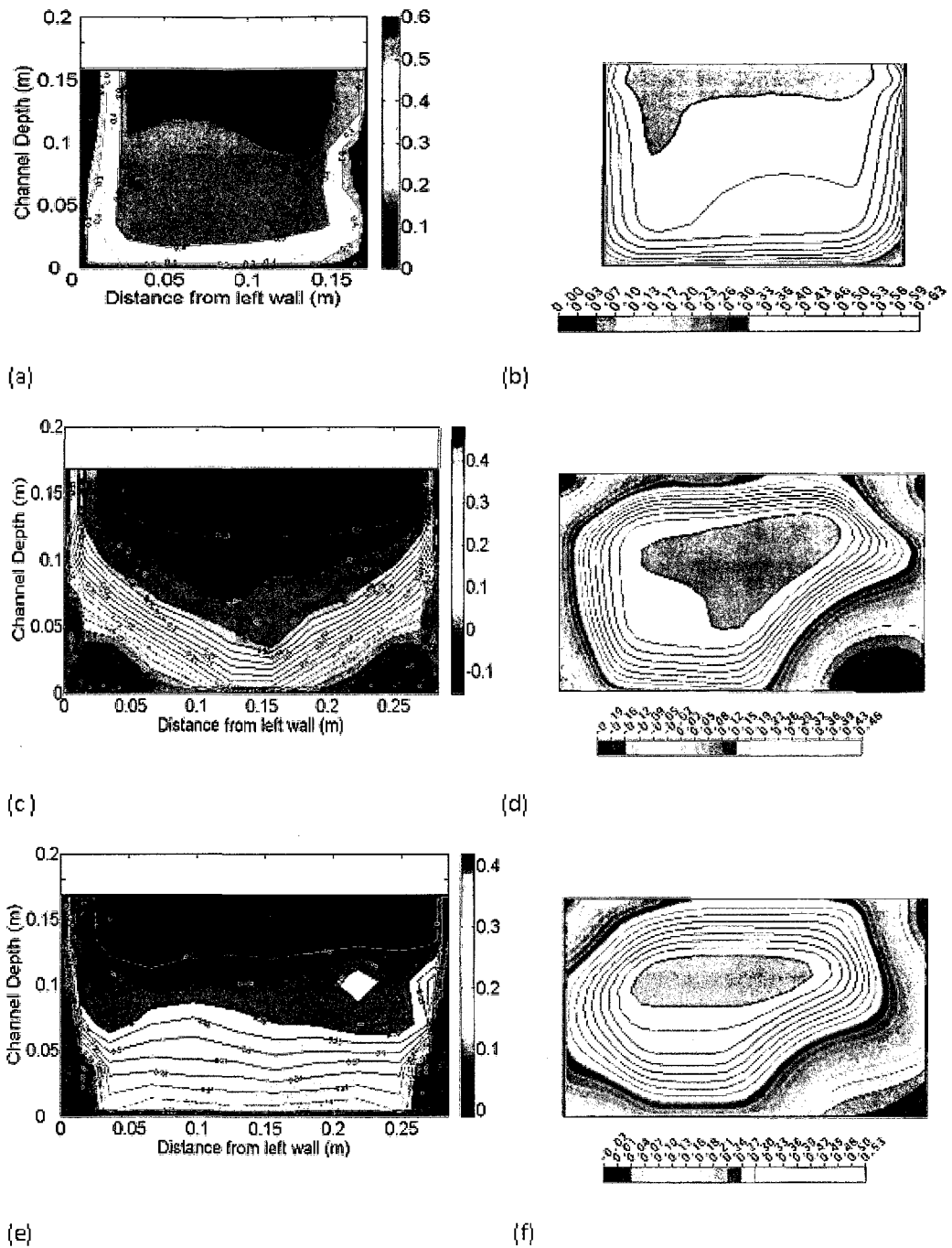


Fig.6.35 Axial velocity Contours for Section 1-1: (a) Experimental (b) Numerical, Section 4-4: (c) Experimental (d) Numerical, Section 5-5: (e) Experimental (f) Numerical

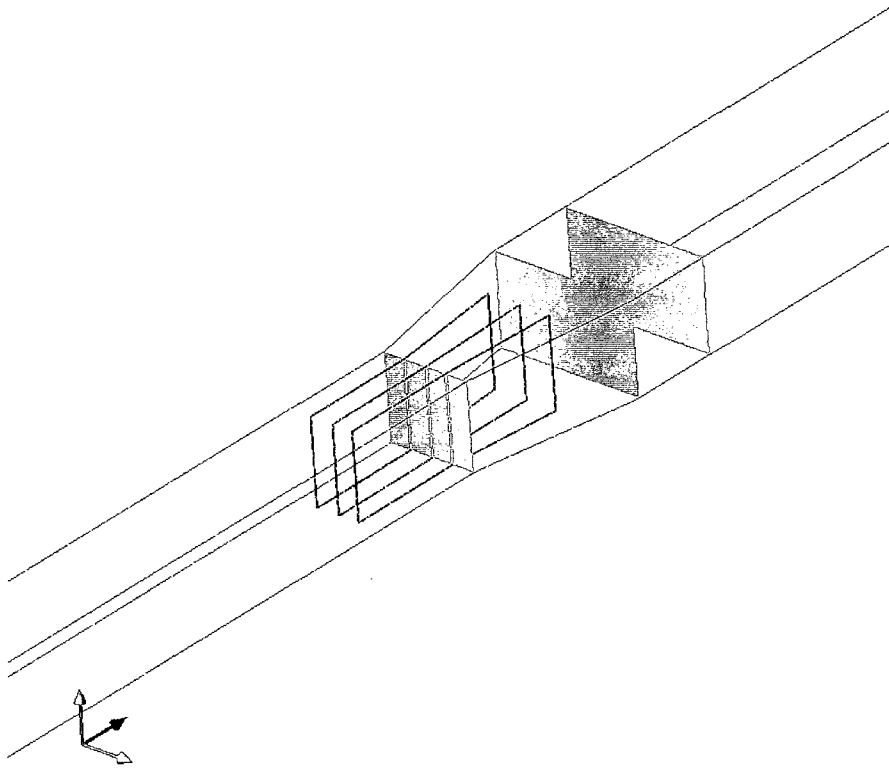


Figure 6.36 Flow Simulations with Vanes

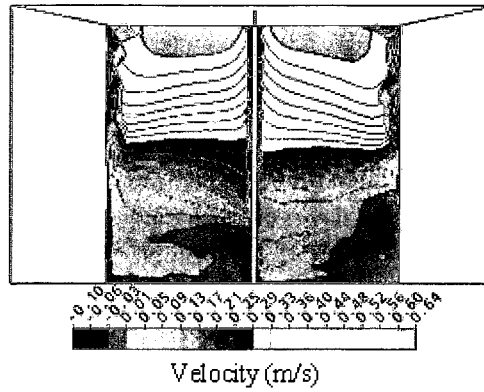
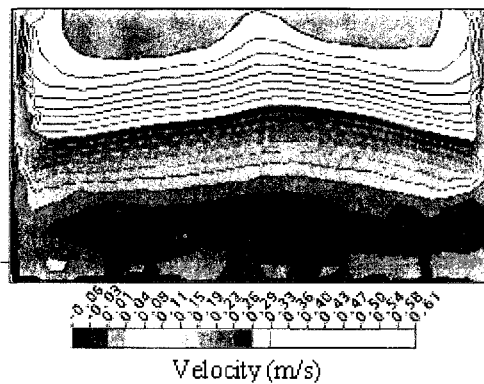
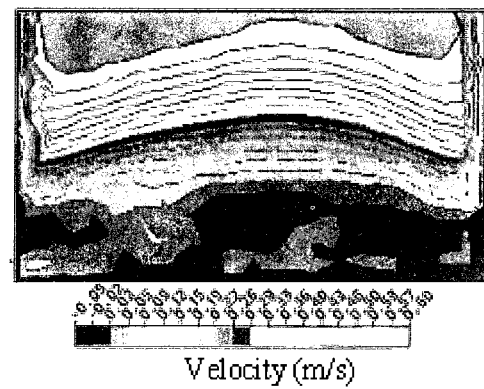
(a) Section at  $x = 0.0$  m (Entry)(b) Section at  $x = 0.325$  m (Exit)(c) Section at  $x = 0.650$  m (Down stream)

Fig. 6.37 Simulated Axial Velocity Contours ( $U$  m/s) with 1 Vane ( $Q = 0.0142$   $\text{m}^3/\text{s}$ )

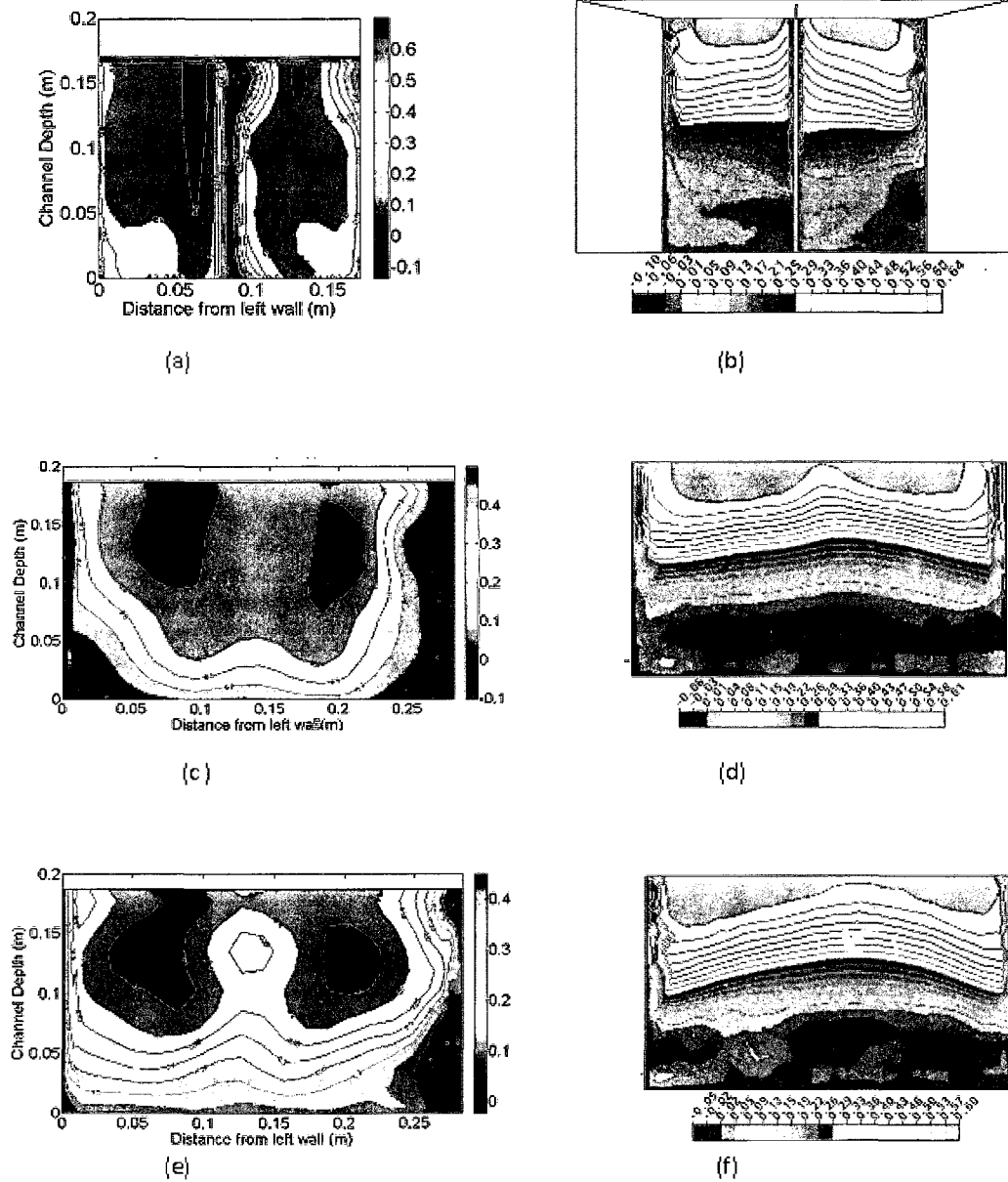
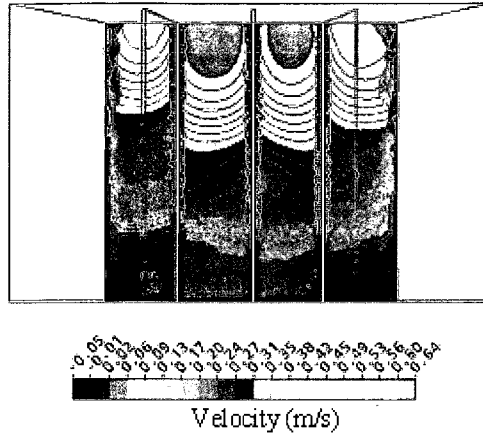
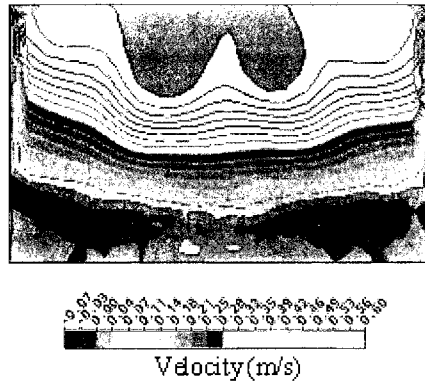


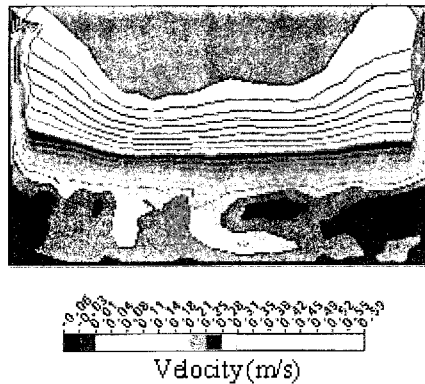
Fig.6.38 Axial Velocity Contours with 1 Vane for Section 1-1: (a) Experimental (b) Numerical, Section 4-4: (c) Experimental (d) Numerical, Section 5-5: (e) Experimental (f) Numerical



(a) Section at  $x = 0.0$  m (Entry)



(b) Section at  $x = 0.325$  m (Exit)



(c) Section at  $x = 0.650$  m (Down stream)

Fig. 6.39 Simulated Axial Velocity  $U$  (m/s) Contours with 3 Vanes ( $Q = 0.0142 \text{ m}^3/\text{s}$ )



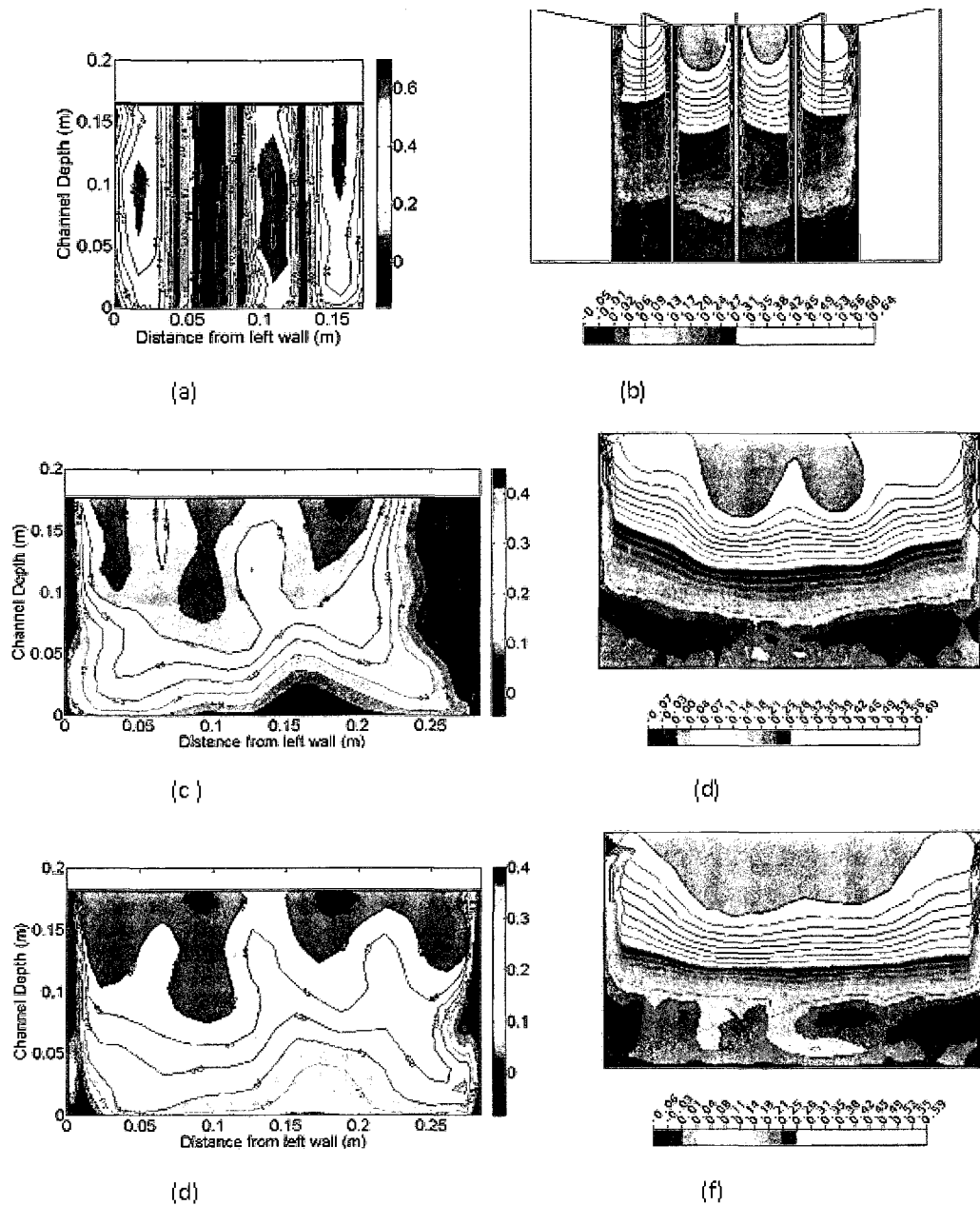


Fig.6.40 Axial Velocity Contours with 3Vaness for Section 1-1: (a) Experimental (b) Numerical, Section 4-4: (c) Experimental (d) Numerical, Section 5-5: (e) Experimental (f) Numerical

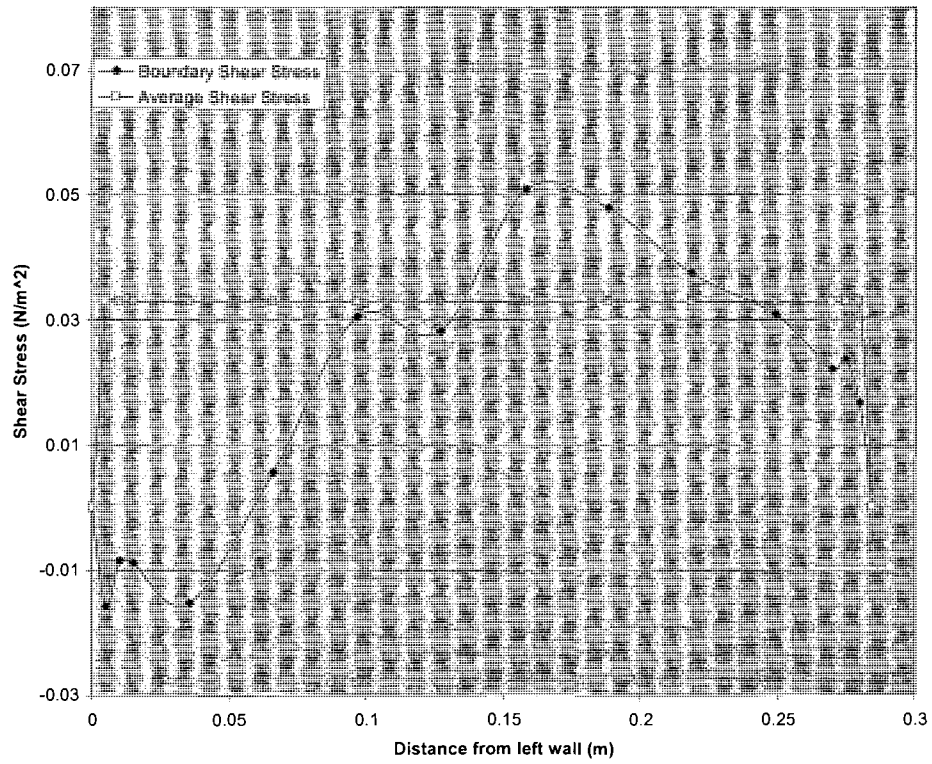


Fig.6.41 Boundary Shear Stress in Channel Transitions

## REFERENCES

- Abramowitz, M. (1949). "On backflow of a viscous fluid in a diverging channel." Journal of math. Physics. No 28.1-21.
- Archer, W. H. (1913). "Experimental determination of loss of head due to sudden enlargement in circular pipes." Trans. ASCE, Vol. LXXVI, 999.
- Bhandari, N. N., and Uppal, H. L. (1938). "Protection against Scour of River and canal Works." Paper No. 214, Punjab Eng. Congress.
- Brundrett, E., and Baines, W. (1964). The production and diffusion of vorticity in duct flow." J. Fluid Mech.,19(3), 375-394.
- Carlson, J. J. , Johnston, J. P., and Sagi, C. J.(1967). "Effects of Wall shape on flow regimes and performance in straight, two dimensional diffusers.", Journal of Basic Engineering, No. 3, 151-160.
- Chaturvedi, R. S. (1963). "Expansive Subcritical Flow in Open Channel Transitions." Journal of the Institution of Engineers, Civil Eng. Div., India, vol. 43, May, 447-487.
- Chow, V. T. (1959), Open Channel Hydraulics, McGraw-Hill, New York. 461-468.
- Cochran, D. L., and Kline, S. J.(1958). "The use of short of flat vanes for producing efficient wide-angle two dimensional sub-sonic diffusers." NACATN 4309.
- Daugherty, R. L., and Ingersoll, A., C. (1964), "Fluid Mechanics." McGraw-Hill Book Co., Inc., New York. 759-764.
- Davis, C. V. (1942). "Handbook of Applied Hydarulics." McGraw-Hill Book Co., New York, 14.

- Ead et al. (2000). "Turbulent open channel flow in circular corrugated culverts." *J. Hydraulic Eng.*, 126(10), 750-757.
- El-Shewey, M. I. A., and Joshi, S. G. (1996). "A study of turbulence characteristics in open channel transitions as a function of Froude and Reynolds numbers using laser technique." *Adv. Fluid mech.*, 9, 363-372.
- Feil, O.G. (1962). "Vane system for very wide-angle sub-sonic diffusers." Report PD-7, Department of Mechanical Eng. Stanford University.
- Ferziger, J. H. and Peric M. (2002). "Computational Method for CFD." 3<sup>rd</sup> Edition, Springer.
- Formica, G. (1955). "Esperienze preliminary sulle predate di carico nei caneli, dovute a combiamenti di sezione." (Preliminary test on head losses in channel due to cross sectional changes, *L'Energia Electrica*, Milan, Italy, Vol. 32, No. 7, 554-568.
- Fox, R. W. and Kline, S. J. (1962). "Flow regimes in curved subsonic diffuser." *Journal of Basic Engineering.*, Trans. of ASME, Series D, Vol. 84, 303-316.
- Hamel, G. (1916). *Spiralformige Bewegung Zaher Flussigkeiten Jahresber d. Dt. Mathamatikes-Verini-gung*, 34.
- Henderson, F. M. (1966). "Open Channel Flow." 1<sup>st</sup> Edition, The Macmillan Company, new York. 19-45.
- Hinds, J. (1928). "The hydraulic design of flume and siphone transitions." *Transactions, ASCE*, Vol. 92, 1423-1459.
- Hinze, J. O. (1975). "Turbulence". 2<sup>nd</sup> Edition, McGraw-Hill Book Co., New York. 638-650.

- Hwang, N. H. C., and Houghtalen, R. J. (1996). "Fundamentals of Hydraulic Engineering systems." 2<sup>nd</sup> Edition, Prentice Hall, New Jersey. 169-180.
- Ingham, D. B., and Ma, L. (2005). "Fundamental equations for CFD in river flow simulations." Computational Fluid Dynamics: Application in Environmental Hydraulics, John Wiley and Sons, Ltd.
- Kalinske, A. A. (1946). "Conversion of kinetic energy to potential energy in flow expansions." ASCE, Vol. 111, 355-390.
- Liiv, T., and Lagemaa, P. (2008). "The variation of the velocity and turbulent kinetic energy field in the vicinity of the breaking point." Estonian Journal of Engineering, Vol. 14, 1, 42-64.
- Mehta, P. R. (1981). "Separated flow through large sudden expansions." J. Hydraulic Div., Am. Soc. Civ. Eng., 107(4), 451-460.
- Millsaps, K, and Pohlhausen, K. (1953). "Thermal distribution in Jeffery-Hamel flows between non-parallel plane walls." Journal of Aero. Sci. vol. 20. 187-196.
- Montagu, A. M. r. (1934). "Fluming." Publication No. 6, C. B. I., Simla, India.
- Nezu, I., and Nakagawa, H. (1993). "Turbulence in open channel flows." A. A. Balkema, Rotterdam, The Netherlands.
- Papanicolaou, A. N., and Hildale, R. (2002). "Turbulence characteristics in gradual channel transition." Journal of Eng. Mech., Vol. 128, No. 9. 948-960.
- Ramamurthy, A. S., Basak, S. and Rao, P. R. (1970). "Open channel expansions fitted with local hump." Journal of the Hydraulic Division, ASCE, Vol. 96, No. HY5, 1105-1113.

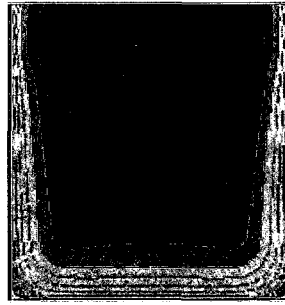
- Ramamurthy, A. S. et al. (2005). "Volume of fluid model for an open channel problem." Canadian Journal of Civil Engineering, Vol. 32, 5. CBCA Reference. 996.
- Rao, P. R. (1967). "Exploratory studies on channel expansions". Unpublished Masters Thesis, Indian Institute of Science.
- Renu, L. R., et al. (1967). "Performance and design of straight two-dimensional diffusers." Journal of basic Engineering, transactions, ASME, Vol. 89, 141-150.
- Schlichting, H., and Gersten, H. (2000). "Boundary-Layer Theory." 8<sup>th</sup> English Edition, Springer, New York, 29-112.
- Seetharamia, K and Ramamurthy, A. S. (1968). "Triangular sills in open channel expansions." Civil Engineering and Public Works Review, Vol. 63, 283.
- Smith, C. D., and James N. G. Yu (1966). "Use of baffles in open channel expansions." Journal of the Hydraulic Division, ASCE, Vol. 92, No. HY2, Proc. Paper 4703, 1-17.
- Soliman, M. M. (1966). "Proc. of ASCE, Journal of Hydraulics Division, Vol. 92, No. HY5, 255-259.
- Versteeg, H. K., and Malalasekera, W. (2007). "An introduction to computational fluid dynamics." 2<sup>nd</sup> Edition, PEARSON, Prentice Hall, New York.
- Waitman, B. A., and Reneau, L. R., and Kline, S. J. (1961). "Effects of Inlet condition on performance of two dimensional diffusers." J. of Basic Eng., Trans. ASME, serried D, vol. 83, 349-360.
- Wilcox, D. C. (1994). "Simulation of transition with a two-equation turbulence model." AIAAJ, 32(2), 247-255.

Wilcox, D. C. (2000), "Turbulence Modeling for CFD." 3<sup>rd</sup> Edition, DCW Industries, Inc.

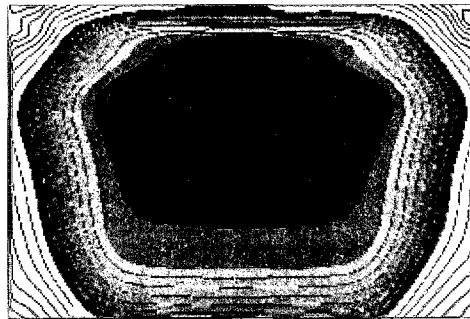
Winternitz, F. A. L., and Ramsey, W. J. (1957). "Effects of inlet boundary layer on pressure recovery, energy conversion, and losses in conical diffusers." *J. of Royal Aer. Society*, Vol. 61. 116.

Wu, X. et al. (1998), "Numerical investigation of the turbulent boundary layer over a bump." *J. Fluid Mech.* Vo. 362, 229-271.

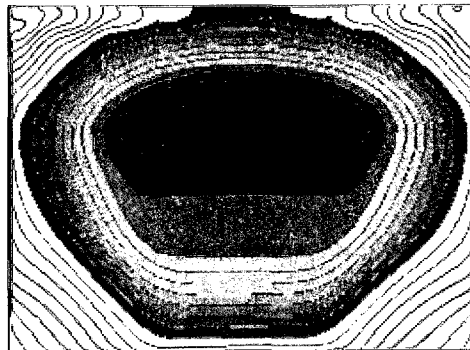
## APPENDIX-A. SECONDARY FLOW CHARACTERISTICS



Velocity (m/s)

(a) Section at  $x = 0.0$  m (Entry)

Velocity (m/s)

(b) Section at  $x = 0.325$  m (Exit)

Velocity (m/s)

(c) Section at  $x = 0.650$  m (Down stream)Fig. A1 Simulated Axial Velocity ( $u$ , m/s) Contours with 25 mm Hump ( $Q = 0.0142 \text{ m}^3/\text{s}$ )



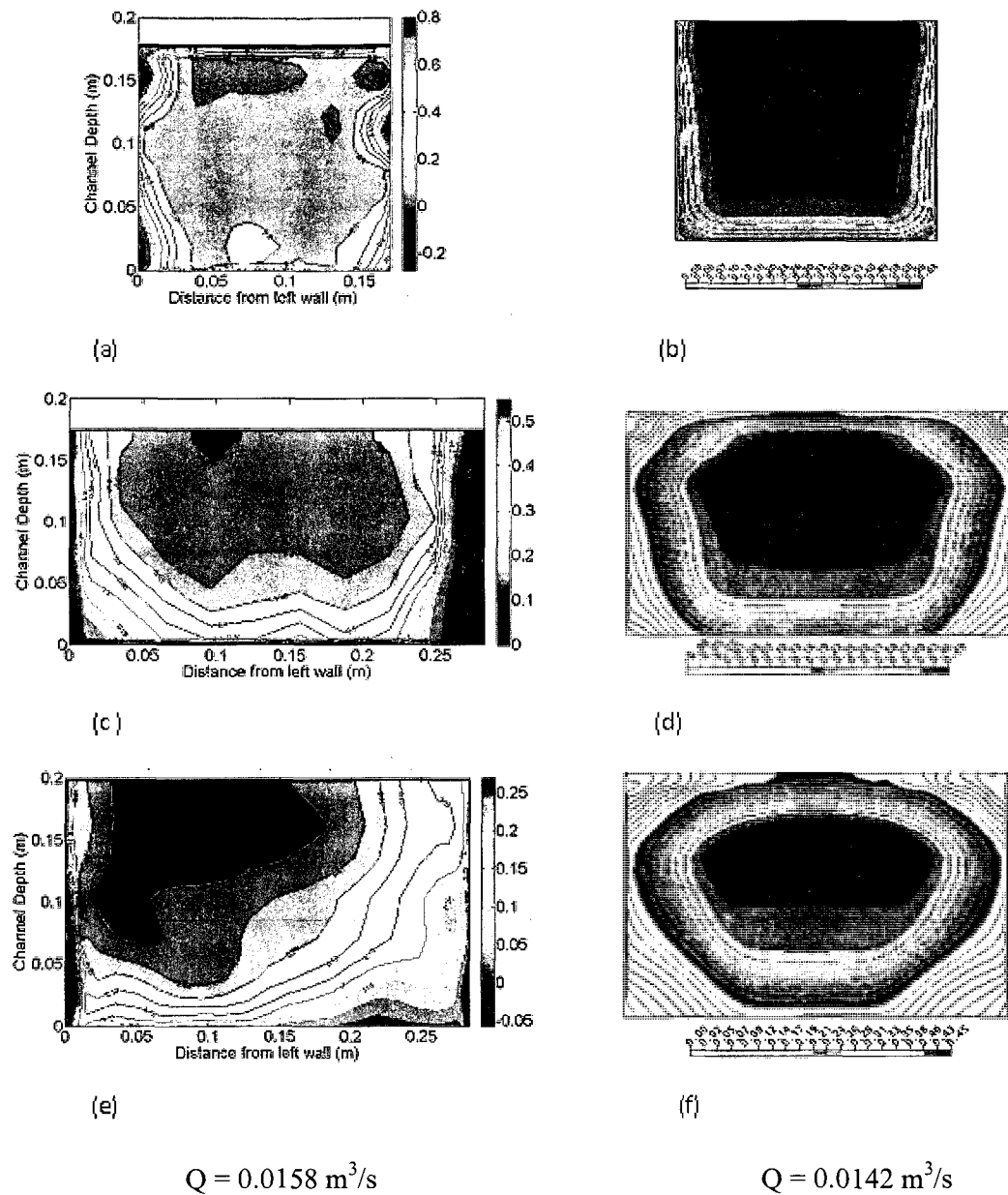
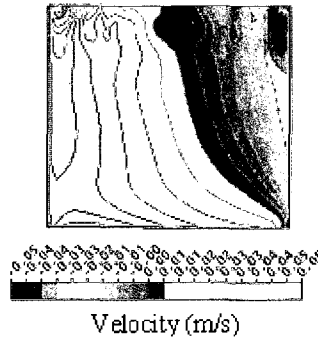
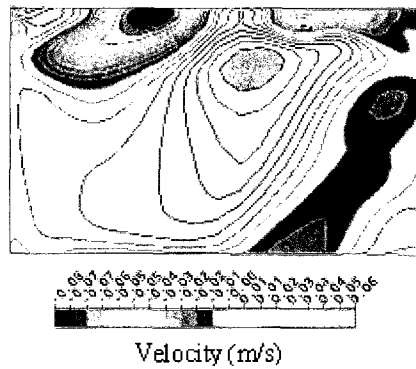


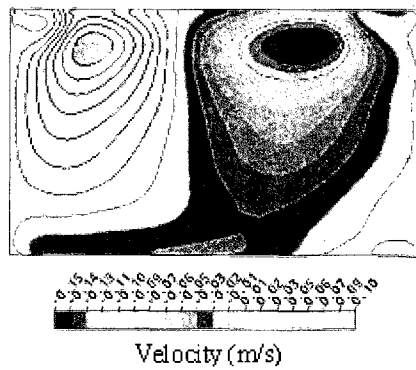
Fig. A2. Axial Velocity Contours with 25 mm hump for Section 1-1: (a) Experimental (b) Numerical, Section 4-4: (c) Experimental (d) Numerical, Section 5-5: (e) Experimental (f) Numerical



(a) Section at  $x = 0.0$  m (Entry)

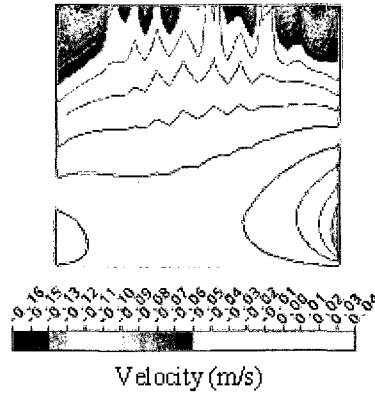


(b) Section at  $x = 0.325$  m (Exit)

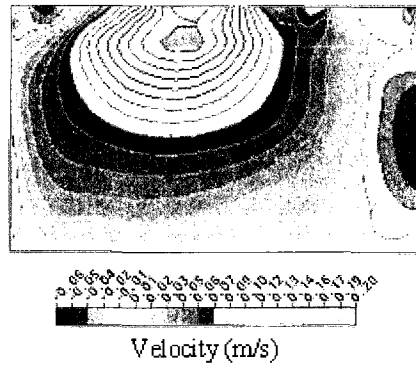


(c) Section at  $x = 0.650$  m (Down Stream)

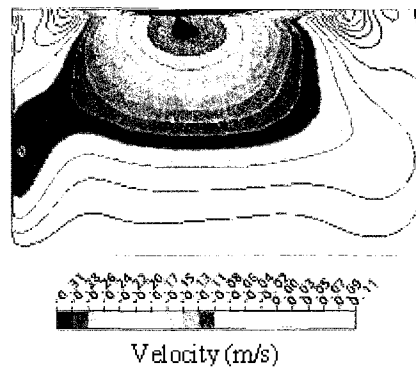
Fig. A3 Simulated Transverse Velocity ( $W$ , m/s) without Hump ( $Q = 0.0133 \text{ m}^3/\text{s}$ )



(a) Section at  $x = 0.0$  m (Entry)



(b) Section at  $x = 0.325$  m (Exit)



(c) Section at  $x = 0.650$  m (Down stream)

Fig. A4 Simulated Vertical Velocity ( $V$ , m/s) without Hump ( $Q = 0.0133$   $\text{m}^3/\text{s}$ )

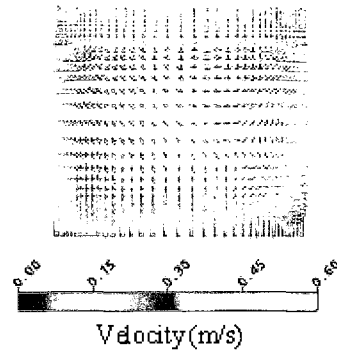
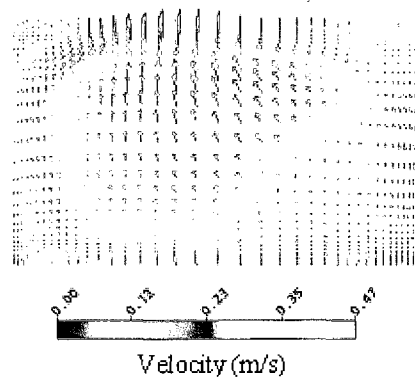
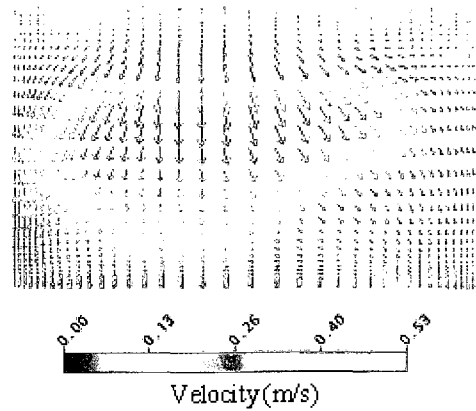
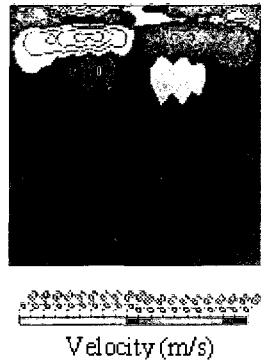
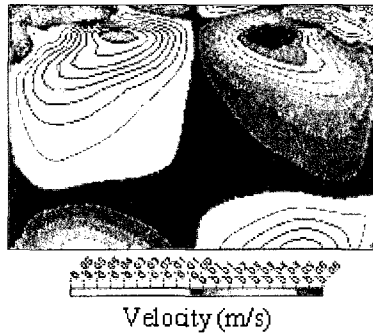
(a) Section at  $x = 0.0$  m (Entry)(b) Section at  $x = 0.325$  m (Exit)(c) Section at  $x = 0.650$  m (Down stream)

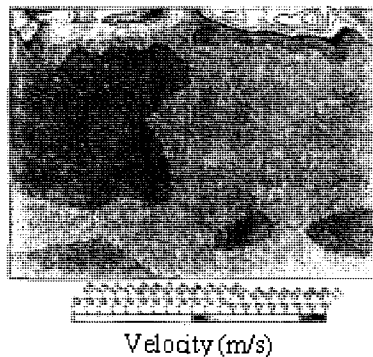
Fig. A5 Simulated Velocity Vectors of V-W Components ( $Q = 0.0133$   $\text{m}^3/\text{s}$ )



(a) Section at  $x = 0.0$  m (Entry)

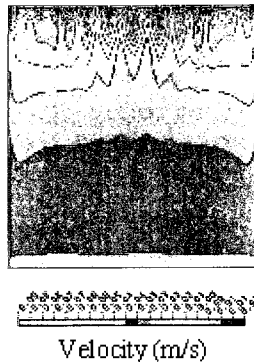


(b) Section at  $x = 0.325$  m (Exit)

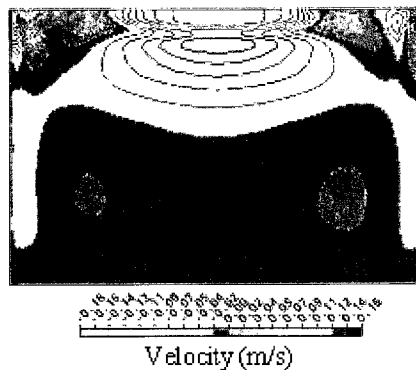


(c) Section at  $x = 0.650$  m (Down stream)

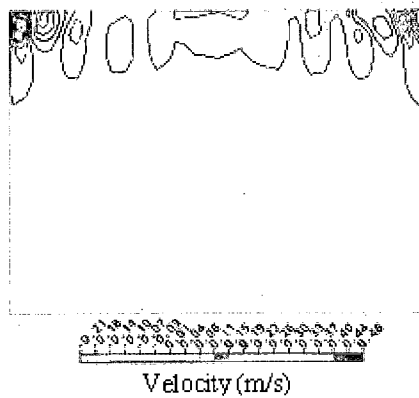
Fig. A6 Simulated Transverse Velocity ( $w$ , m/s) Contours with 25 mm Hump ( $Q = 0.0142$  m<sup>3</sup>/s)



(a) Section at  $x = 0.0$  m (Entry)

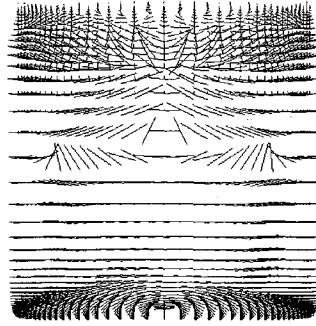


(b) Section at  $x = 0.325$  m (Exit)

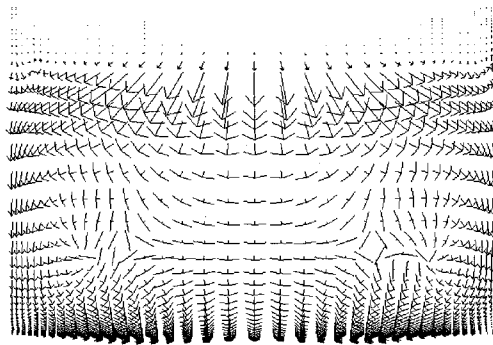


(c) Section at  $x = 0.650$  m (Down stream)

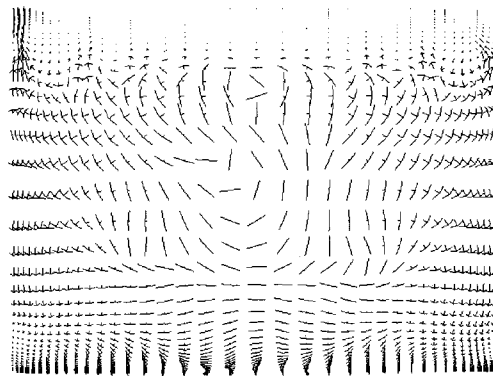
Fig. A7 Simulated Vertical Velocity ( $V$ , m/s) Contours with 25 mm Hump ( $Q = 0.0142 \text{ m}^3/\text{s}$ )



(a) Section at  $x = 0.0$  m (Entry)

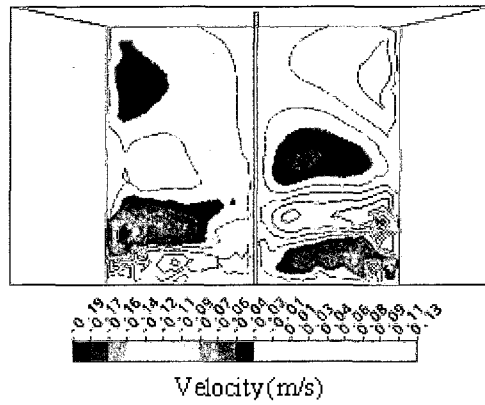


(b) Section at  $x = 0.325$  m (Exit)

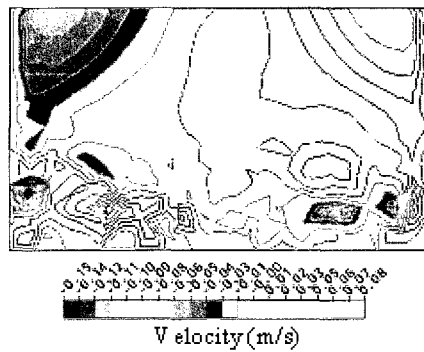


(c) Section at  $x = 0.650$  m (Down stream)

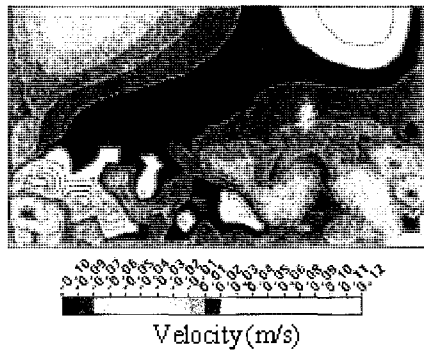
Fig. A8 Simulated Velocity Vectors ( $U$ , m/s) with 25 mm Hump ( $Q = 0.0142 \text{ m}^3/\text{s}$ )



(a) Section at  $x = 0.0$  m (Entry)



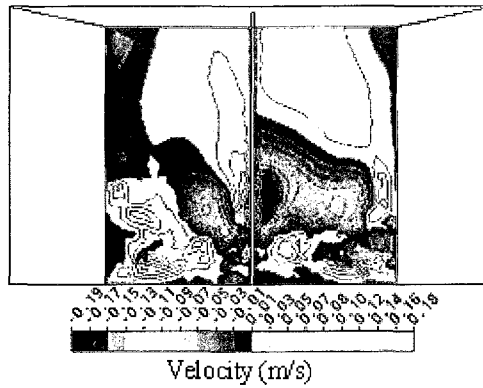
(b) Section at  $x = 0.325$  m (Exit)



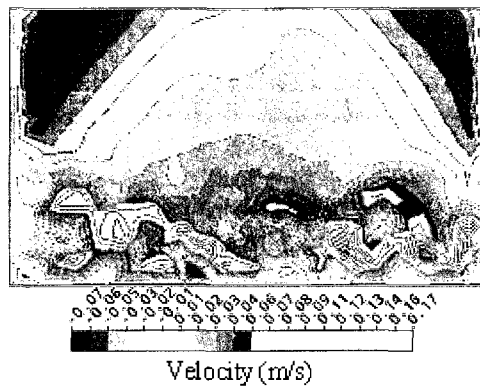
(c) Section at  $x = 0.650$  m (Down stream)

Fig. A9 Simulated Transverse Velocity  $W$  (m/s) Contours with 1 Vane ( $Q = 0.0142 \text{ m}^3/\text{s}$ )

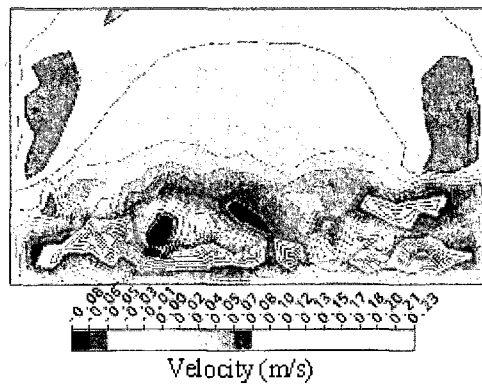




(a) Section at  $x = 0.0$  m (Entry)



(b) Section at  $x = 0.325$  m (Exit)



(c) Section at  $x = 0.650$  m (Down stream)

Fig. A10 Simulated Vertical Velocity  $V$  (m/s) Contours with 1 Vane ( $Q = 0.0142 \text{ m}^3/\text{s}$ )

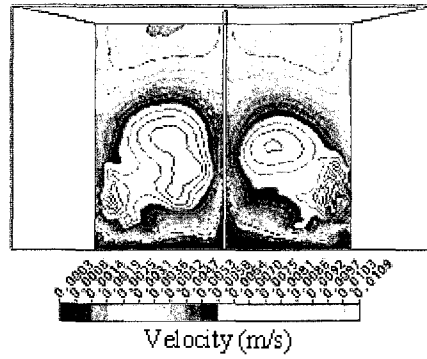
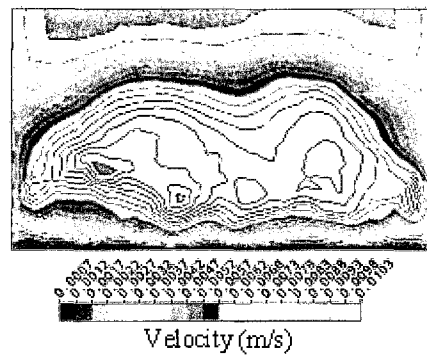
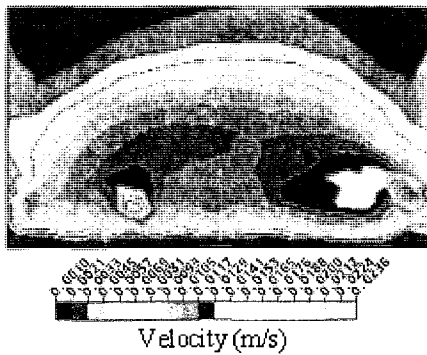
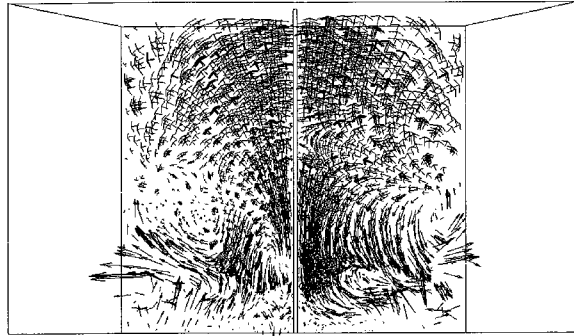
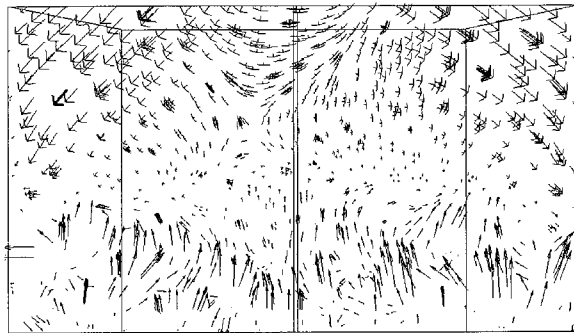
(a) Section at  $x = 0.0$  m (Entry)(b) Section at  $x = 0.325$  m (Exit)(c) Section at  $x = 0.650$  m (Down stream)

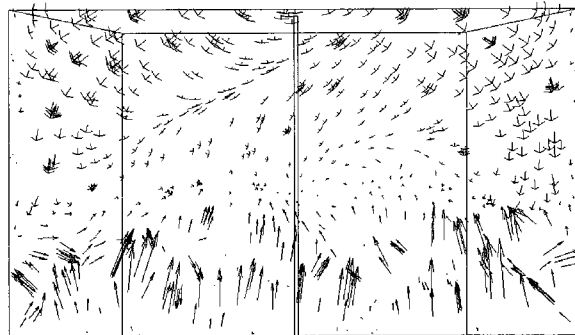
Fig. A11 Simulated Turbulence Kinetic Energy ( $\text{m}^2/\text{s}^2$ ) with 1 Vane ( $Q = 0.0142 \text{ m}^3/\text{s}$ )



(a) Section at  $x = 0.0$  m (Entry)

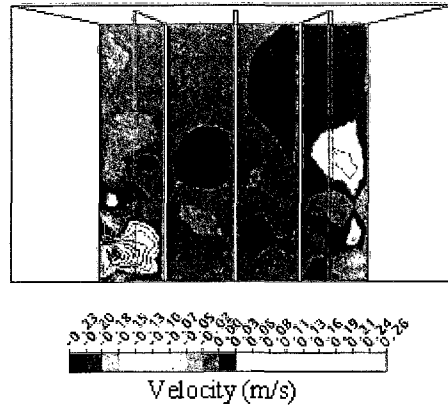


(c) Section at  $x = 0.325$  m (Exit)

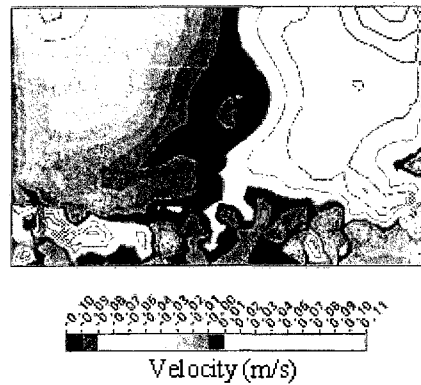


(c) Section at  $x = 0.650$  m (Down stream)

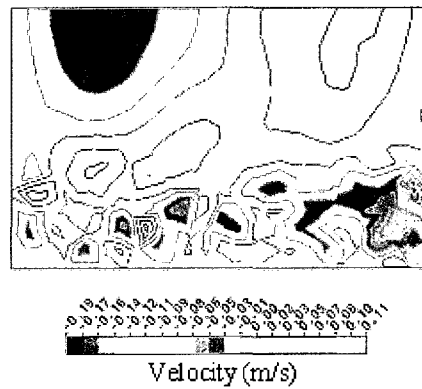
Fig. A12 Simulated Velocity Vectors of V-W Components with 1 Vane ( $Q = 0.0142 \text{ m}^3/\text{s}$ )



(a) Section at  $x = 0.0$  m (Entry)

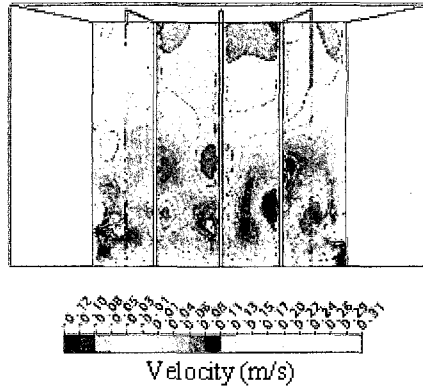


(b) Section at  $x = 0.325$  m (Exit)

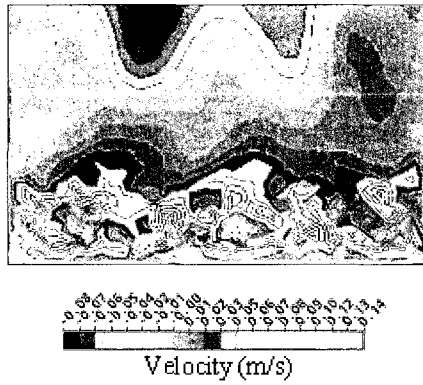


(c) Section at  $x = 0.650$  m (Down stream)

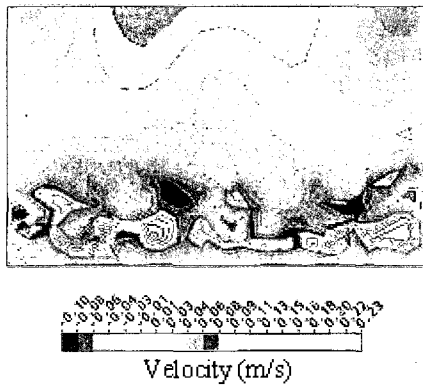
Fig. A13 Simulated Transverse Velocity  $W$  (m/s) Contours with 3 Vanes ( $Q = 0.0142 \text{ m}^3/\text{s}$ )



(a) Section at  $x = 0.0$  m (Entry)



(b) Section at  $x = 0.325$  m (Exit)



(c) Section at  $x = 0.650$  m (Down stream)

Fig. A14 Simulated Vertical Velocity  $V$  (m/s) Contours with 3 Vanes ( $Q = 0.0142 \text{ m}^3/\text{s}$ )

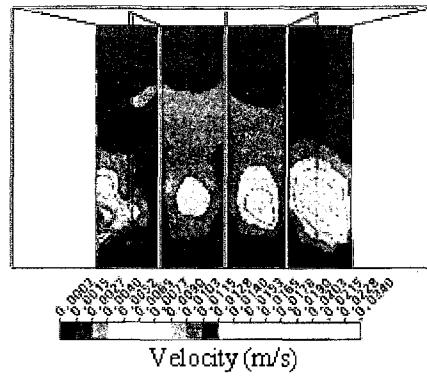
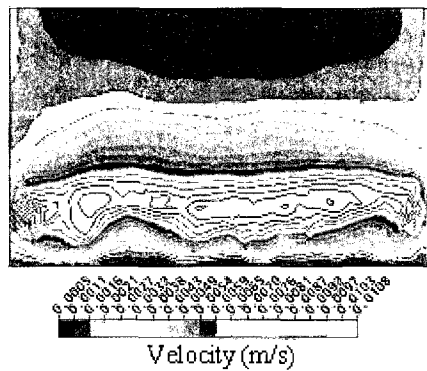
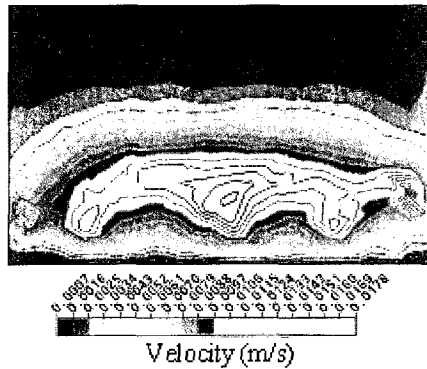
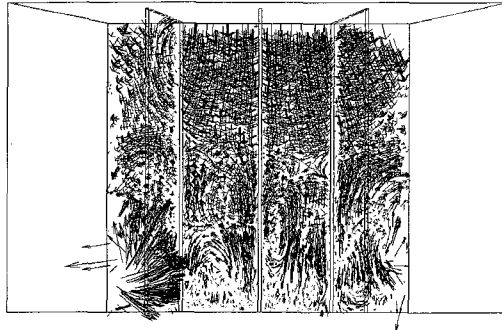
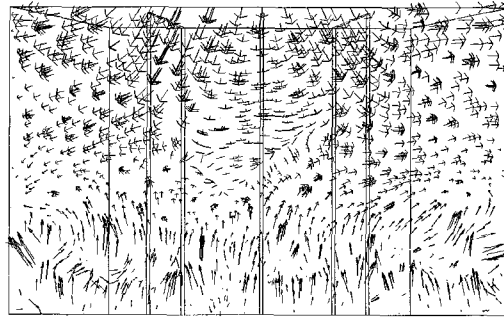
(a) Section at  $x = 0.0$  m (Entry)(b) Section at  $x = 0.325$  m (Exit)(c) Section at  $x = 0.650$  m (Down stream)

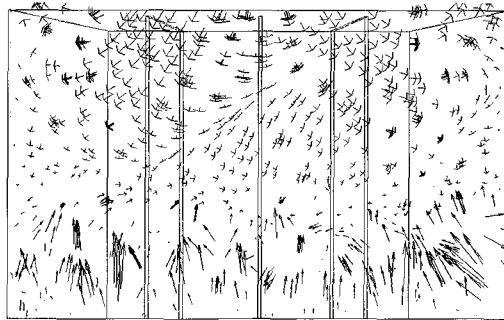
Fig. A15 Simulated Turbulence Kinetic Energy ( $\text{m}^2/\text{s}^2$ ) with 3 Vanes ( $Q = 0.0142 \text{ m}^3/\text{s}$ )



(a) Section at  $x = 0.0$  m (Entry)



(b) Section at  $x = 0.325$  m (Exit)



(c) Section at  $x = 0.650$  m (Down stream)

Fig. A16 Simulated Velocity Vectors of V-W Components with 3 Vanes ( $Q = 0.0142 \text{ m}^3/\text{s}$ )

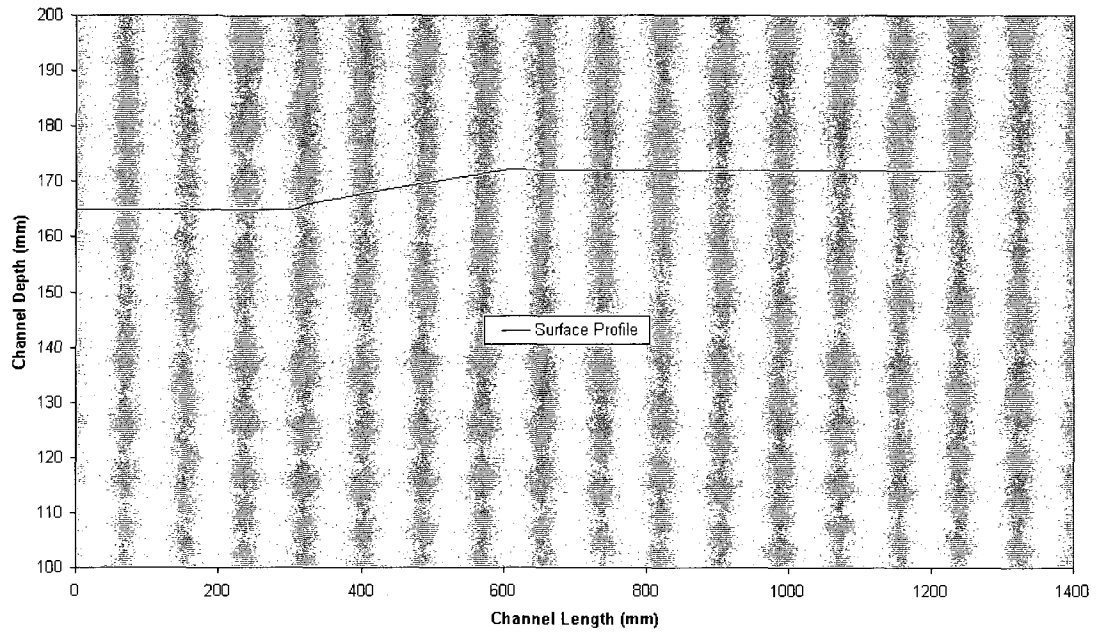


Fig. A.17 Experimental Surface Profile for  $Q_1 = 0.0133 \text{ m}^3/\text{s}$  (No Hump/Vane)

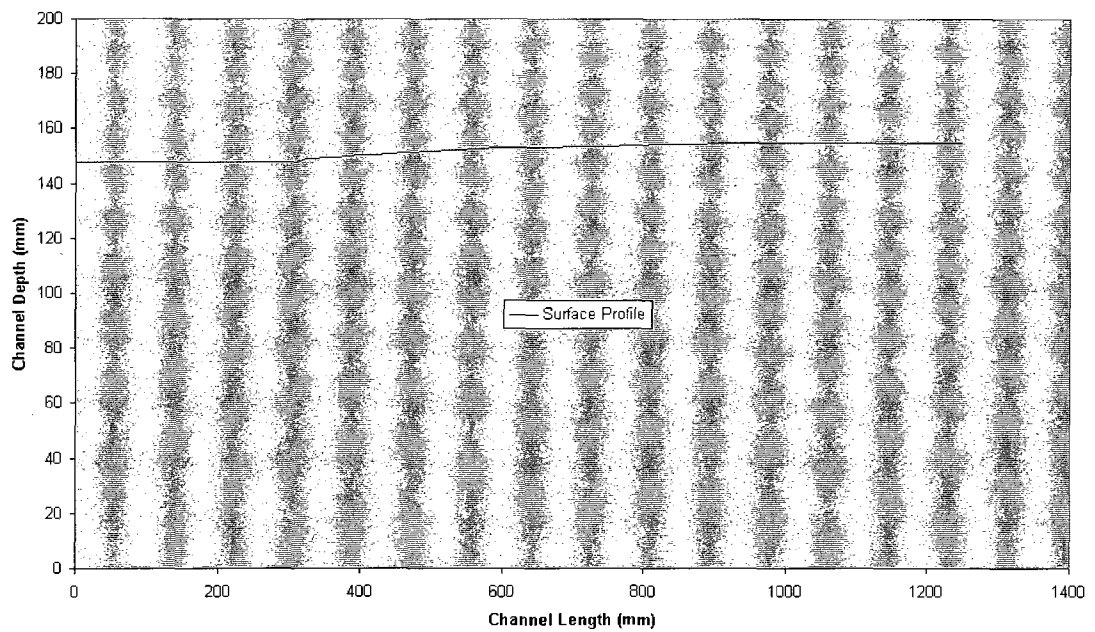


Fig.6.18 Experimental Surface Profile for  $Q_1 = 0.0070 \text{ m}^3/\text{s}$  (No Hump/Vane)  
 $X = 300 \text{ mm}$  (Entry)



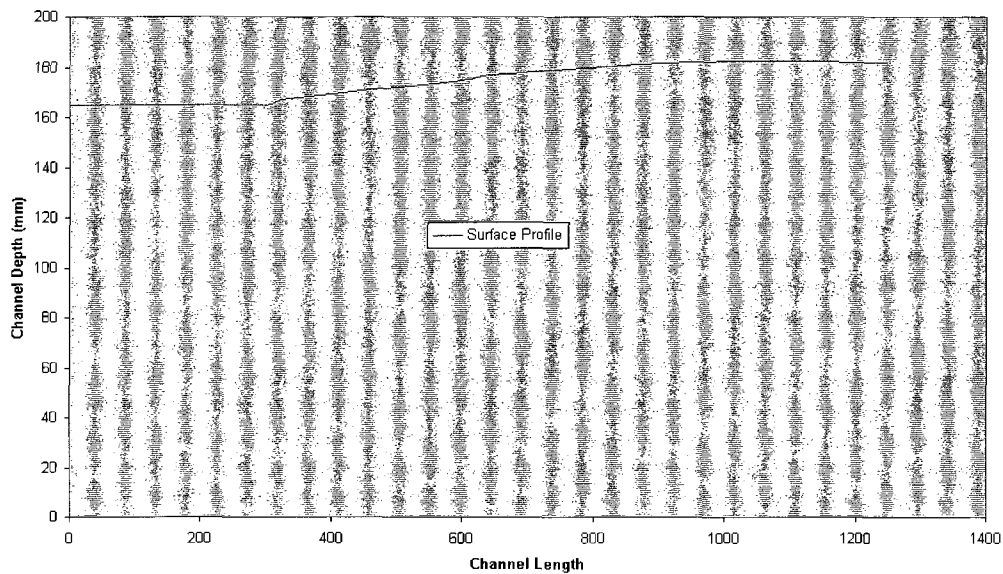


Fig.6.19 Experimental Surface Profile for  $Q_1 = 0.0142 \text{ m}^3/\text{s}$  (No Hump/Vane)

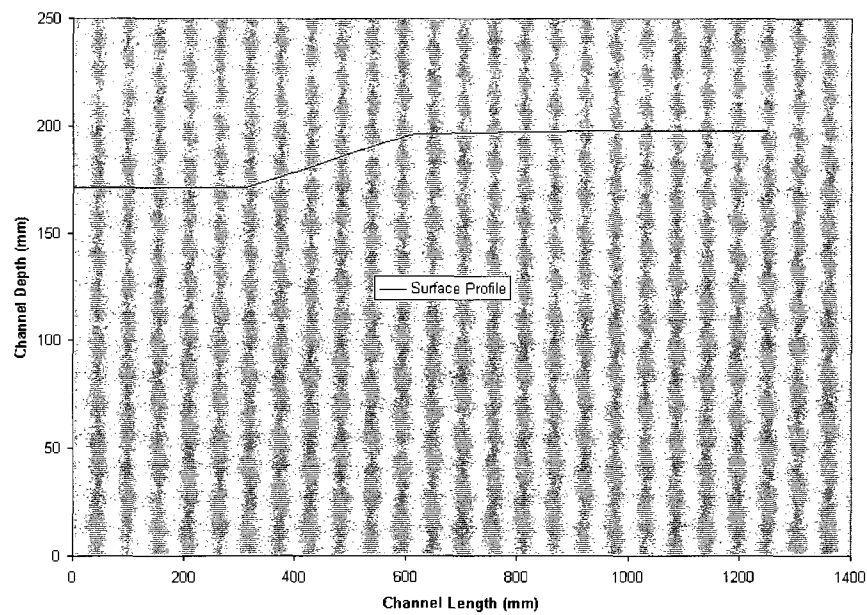


Fig.6.20 Experimental Surface Profile for  $Q_1 = 0.0158 \text{ m}^3/\text{s}$  (25 mm Hump)  
 $X = 300 \text{ mm}$  (Entry)

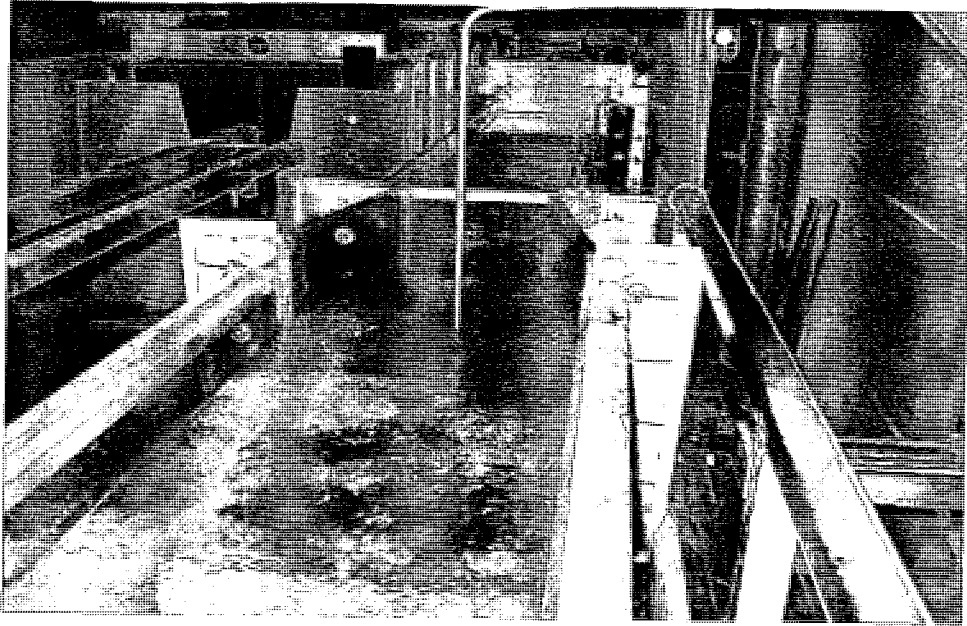


Fig A21 Laboratory Setup showing Flow Separation Visualization with Dyes

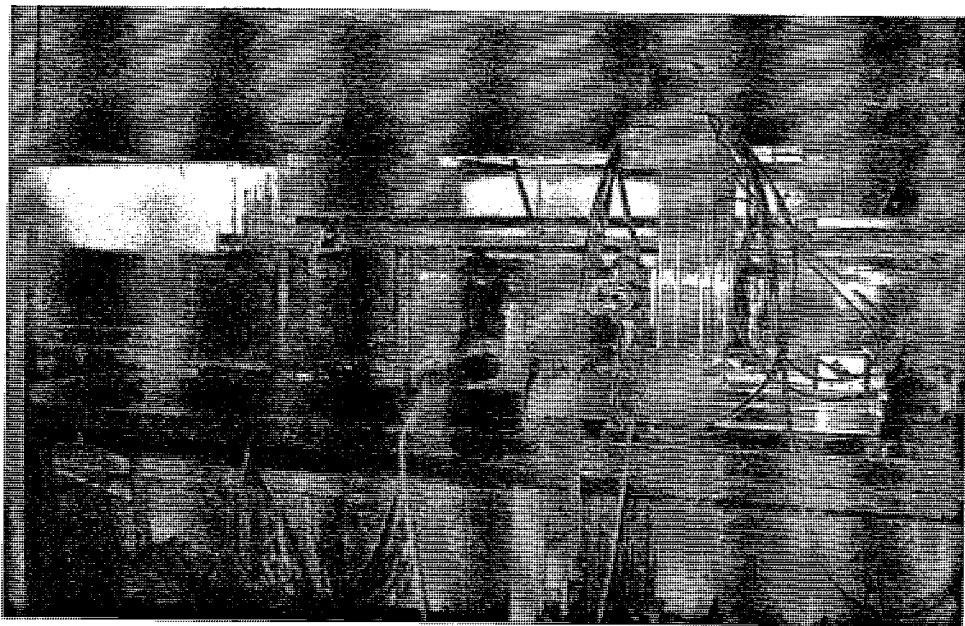


Fig A22 Laboratory Setup showing LDA Probe and Traverse

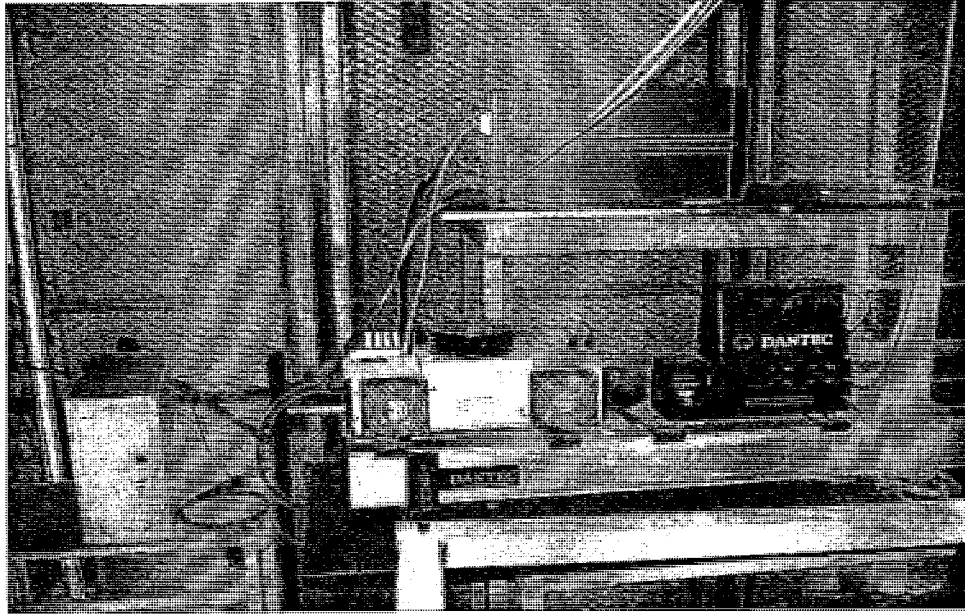


Fig A23 Laboratory Setup showing LDA Processor and CPU

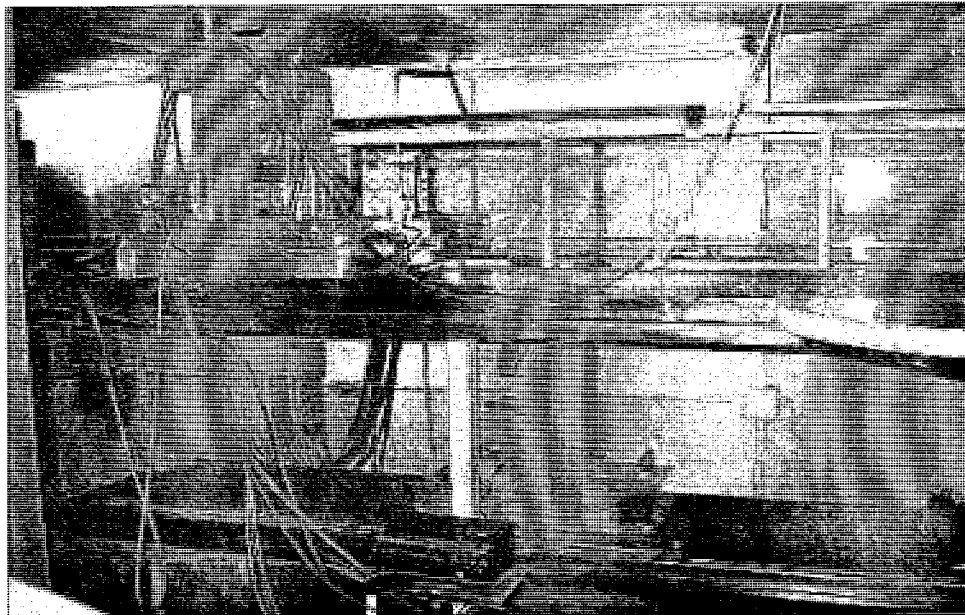


Fig A24 Laboratory Setup showing Top and Bottom Traverses with Controller

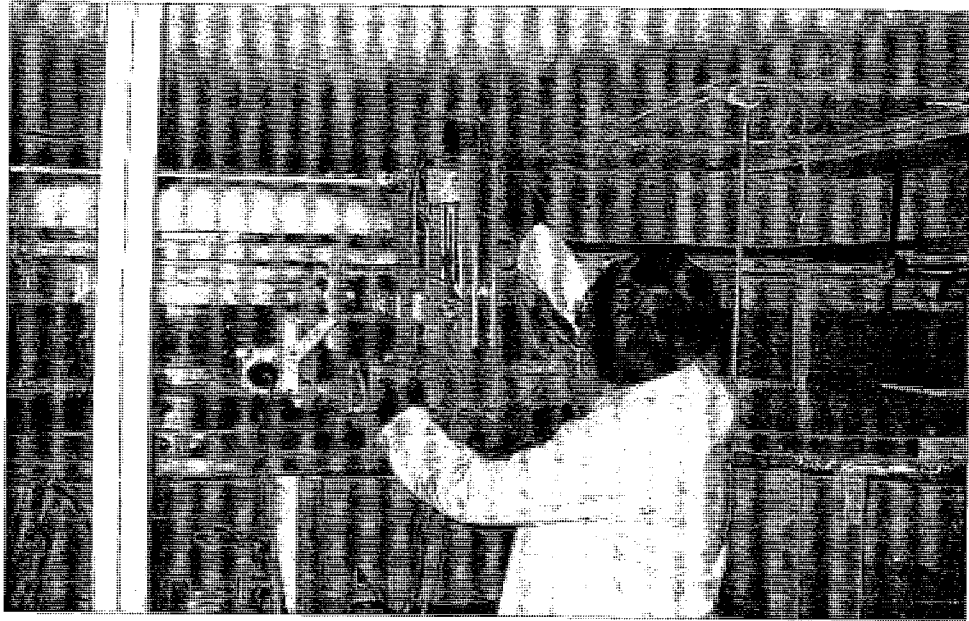


Fig A25 Investigator working in the Lab

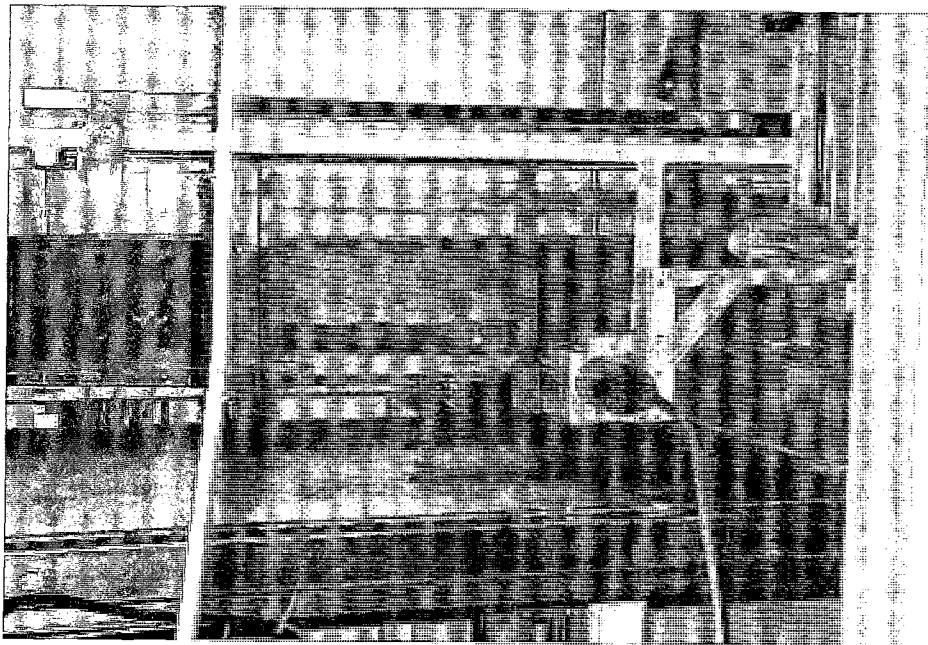


Fig A26 Laboratory Setup showing Laser Beam Penetrating through Plexiglas

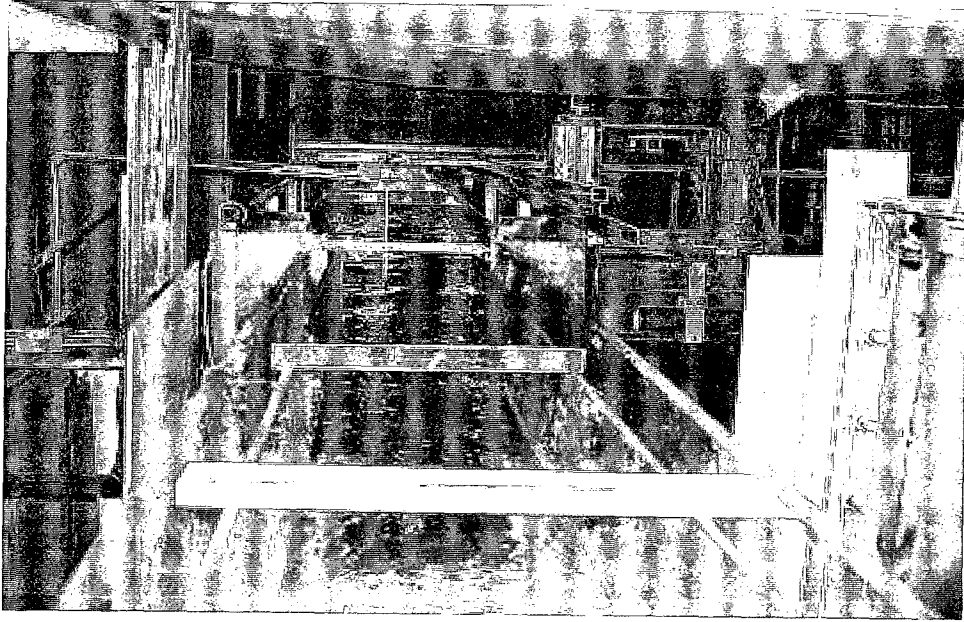


Fig A27 Laboratory Setup showing the Channel Transition from Down Stream Looking Upstream

## APPENDIX-B

Table B.1 Sample calculation of the values of  $\alpha$  and  $\beta$ 

Section	Discharge Q(m <sup>3</sup> /s)	Mean value of the Contours v(m/s)	Area of strips	vdA	v <sup>2</sup> dA	v <sup>3</sup> dA	Vm	A (m <sup>2</sup> )	$\alpha$	$\beta$
(5-5)	0.0158	0.21	0.005	0.001	0.0002	0.00005	0.295	0.0562	1.09	1.03
		0.3	0.005	0.002	0.0005	0.00014				
		0.34	0.005	0.002	0.0006	0.00020				
		0.37	0.005	0.002	0.0007	0.00025				
		0.35	0.005	0.002	0.0006	0.00021		Q <sub>LDA</sub> =	0.02	
Ref: Fig.19		0.33	0.005	0.002	0.0005	0.00018		Q <sub>vnotch</sub> =	0.02	
		0.32	0.005	0.002	0.0005	0.00016				
1" Hump		0.31	0.005	0.002	0.0005	0.00015		% Error=	4.43	
		0.29	0.005	0.001	0.0004	0.00012				
		0.23	0.005	0.001	0.0003	0.00006				
		0.2	0.007	0.001	0.0003	0.00005				
				0.017	0.0050	0.00157				